Thesis for Doctor of Philosophy

Design of Low-Carbon, Low-Temperature Bainite

Yang, Hong-Seok (양 홍 석)

Department of Ferrous Technology

Graduate Institute of Ferrous Technology

Pohang University of Science and Technology

2011

Design of Low-Carbon, Low-Temperature Bainite 2011 Yang, Hong-Seok

Design of Low-Carbon, Low-Temperature Bainite

(저탄소 저온 베이나이트 디자인)

Design of Low-Carbon, Low-Temperature Bainite

By
Yang, Hong-Seok
Department of Ferrous Technology
Graduate Institute of Ferrous Technology
Pohang University of Science and Technology

A thesis submitted to the faculty of Pohang University of Science and Technology in partial fulfillments of the requirements for the degree of Doctor of Philosophy in the Graduate Institute of Ferrous Technology (Computational Metallurgy)

Pohang, Korea
26 September 2011

Approved by

Prof. Bhadeshia, H. K. D. H. (Major Advisor)

Prof. Suh, Dong-Woo (Co-advisor)

Design of Low-Carbon, Low-Temperature Bainite

Yang, Hong-Seok

This dissertation is submitted for the degree of Doctor of Philosophy at the Graduate Institute of Ferrous Technology of Pohang University of Science and Technology. The research reported herein was approved by the committee of Thesis Appraisal

26 September 2011

Thesis Review Committee

Chairman : Bhadeshia, H. K. D. H.

Member: De Cooman, B. C.

Member: Lee, Jae-Gon

Member: Lee, Jae-Sang

Member: Suh, Dong-Woo

Preface

This dissertation is submitted for the degree of Doctor of Philosophy at Pohang University of Science and Technology. The research described herein was conducted under the supervision of Professor H. K. D. H. Bhadeshia, Professor of Computational Metallurgy in the Graduate Institute of Ferrous Technology, Pohang University of Science and Technology and Professor of Physical Metallurgy, University of Cambridge, between March 2008 and September 2011.

This work is to the best of my knowledge original, except where acknowledgements and references are made to previous work. Neither this, nor any substantially similar dissertation has been or is being submitted for any other degree, diploma or other qualification at any other university. This dissertation does not exceed 60,000 words in length.

Part of this work has been submitted to appear in the following publications:

Yang, H.-S., Park, J. H. and Bhadeshia, H. K. D. H.: Possibility of low-carbon, low-temperature bainite. Proceedings of the International Conference on Martensitic Transformations, ICOMAT-08 (2008) pp. 695-702

Yang, H.-S. and Bhadeshia, H. K. D. H.: Austenite grain size and the martensite-start temperature. *Scripta Materialia*, Vol. 60 (2009) pp. 493-495

Yang, H.-S., Jang, J. H., Bhadeshia, H. K. D. H. and Suh, D.-W.: Critical assessment: martensite-start temperature for the $\gamma \rightarrow \epsilon$ transformation, submitted (2011)

Hong-Seok Yang

2011

DFT Hong-Seok Yang
20080961 Design of Low-Carbon, Low-Temperature Bainite
Department of Ferrous Technology (Computational Metallurgy)
2011, 155 p
Advisor: Bhadeshia, H. K. D. H and Suh, Dong-Woo
Text in English

Abstract

The aim of the work presented here was to investigate the possibility of a low-carbon version of superbainite. One of the limiting parameters in the design is the martensite-start temperature. The dependence of it on the austenite grain size has been investigated. The Fisher model for the geometrical partitioning of austenite grains by plates of martensite was used to develop a theory to explain the observations, based on the ability to detect transformation as a function of the austenite grain size. The relationship derived has been tested on a wide range of published data.

The work described in above paragraph leaded to the investigation on effect of grain size on athermal martensite kinetics. The study revealed that the martensite transformation rate starts from zero, rapidly increases until a fraction $\cong$ 0.15, and then decreases smoothly. Small grain-sized samples transform rapidly at the early stages because of larger number of initial nucleation sites. However, the grain size dependence diminishes at the later stages because of autocatalysis and decreasing untransformed austenite.

Compiled knowledge on martensite has been applied to assess the ε martensite-start temperatures. Methods have been created for calculating the temperature at which ε-martensite forms when austenite is cooled. It is demonstrated that the thermodynamic method used in similar calculations for α` can be applied for some alloy systems whereas it cannot be implemented for highly

solute concentrated alloys because of inaccurate thermodynamic data, a conclusion was confirmed using first-principles calculations. A neural network model has been developed which is capable of predicting the transformation temperature for a wide range of compositions and complex phenomena.

Three alloys have been designed, manufactured and investigated to evaluate the validity of low-carbon version of low-temperature bainite. Several problems such as low transformation temperature, merging of B_S into M_S, presence of coalesced bainite and slow kinetics could be solved. However, small fraction of retained austenite coming from low-carbon concentration of initial alloy could not be avoided. That resulted in ordinary mechanical properties.

Contents

Preface……...……...i

Abstract……..…...……..…….……ii

Nomenclature……...……...……...…vii

Chapter 1: Introduction ……...…….…...……1

1.1 Aim of the Work…….....1

1.2 Martensite in Steels…….1

1.2.1 Characteristics of Martensite Transformation……..……..2

1.2.1.1 Diffusionless Transformation……2

1.2.1.2 Habit Plane……3

1.2.1.3 Orientation Relationship……...4

1.2.2 Phenomenological Theory of Martensitic Transformation……5

1.2.3 Martensite Nucleation Theory……..11

1.2.4 Martensite-Start Temperatures…….15

1.2.4.1 Prediction of Martensite-Start Temperature……16

1.2.4.2 Measurements of Martensite-Start Temperature…….23

1.3 Bainite in Steels…….....26

1.3.1 Morphology……..26

1.3.2 Displacive Transformation……...28

1.3.3 Incomplete Reaction…….……31

1.3.4 Low-Temperature Bainite……33

1.3.5 Low-Carbon, Low-Temperature Bainite……..39

1.4 Summary…….....47

Chapter 2: M_S and Austenite Grain Szie…….……49

2.1 Introduction……...49

2.2 Experimental…….50

2.3 Results and Discussion……..52

2.3.1 Fisher's Analysis……..54
2.3.2 M_S and Austenite Grain Size……55
2.3.3 Athermal Martensite Kinetics……..58
2.4 Summary……...60

Chapter 3: Athermal Martensite Kinetics……61
3.1 Introduction……...61
3.2 Experimental……..…61
3.3 Results and Discussion……..64
3.4 Summary……...69

Chapter 4: Martensite-Start Temperature for the the $\gamma \rightarrow \varepsilon$ Transformation...70
4.1 Introduction……...70
4.2 Measurements of ε-Martensite Start Temperatures……...71
4.3 Estimation of ε-Martensite Start Temperatures…….74
4.3.1 Empirical Equation……...74
4.3.2 Thermodynamic Calculations……..90
4.3.3 Neural Network……97
4.4 Summary…….101

Chapter 5: Design of Low-Carbon, Low-Temperature Bainite……....103
5. 1 Introduction……103
5.2 Alloy Design……...104
5.3 Experimental……...106
5.4 Alloy A……107
5.5 Alloys B and C……111
5.6 Parameters Affecting Bainite Transformation Kinetics……..116
5.7 Incomplete Reaction……118
5.8 Mechanical Properties…….120

5.9 Summary……122

Chapter 6: Conclusions……..125

Appendix……128

References……..130

Acknowledgements……154

Curriculum Vitae……..……155

Nomenclature

Ac_1	Temperature at which a sample starts to transform to austenite during heating
Ac_3	Temperature at which a sample becomes fully austenitic during heating
Ae_1	Temperature separating the $\alpha + \gamma$ and α phase fields for a specific alloy
Ae_3	Temperature separating the $\alpha + \gamma$ and γ phase fields for a specific alloy
A'_{e3}	As Ae_3, but para-equilibrium boundary
A''_{e3}	As A'_{e3}, but with accounting strain energy of product phase
a_{Fe}	Lattice parameter of pure iron in ferrite phase
a_α	Lattice parameter of ferrite
a_γ	Lattice parameter of austenite
B_S	Bainite-start temperature
f	Martensite fraction
G_N	Universal nucleation function, which is specifying the free energy change needed in order to obtain a detectable rate of nucleation for Widmanstätten ferrite and bainite.
G_F	Free energy per unit area of fault plane
G_{SB}	Stored energy of bainite
G_{STRAIN}	Strain energy
G_{SW}	Stored energy of Widmanstätten ferrite
ΔG_2	Free energy change per mole of ferrite for equilibrium or para-equilibrium transformation

ΔG_3	Free energy change for the formation of a mole of ferrite nuclei with carbon diffusion
ΔG_{CHEM}	Chemical free energy change for martensitic transformation
ΔG_m	Maximum molar free energy change accompanying nucleation
$\Delta G^{\gamma\to\alpha}$	Free energy change for $\gamma \to \alpha$ transformation without composition change
$\Delta G^{\gamma\to\varepsilon}$	Free energy change for $\gamma \to \varepsilon$ transformation
$\Delta G_{\mathrm{C}}^{\gamma\to\alpha}$	Critical free energy change for stimulating martensitic transformation
$\Delta G_{M_{\mathrm{S}}}^{\gamma\to\varepsilon}$	Free energy change for $\gamma \to \varepsilon$ transformation at M_{S}
$\Delta G^{\gamma\to\gamma'+\alpha}$	Free energy change for equilibrium transformation
$\bar{L}$	Mean lineal intercept
m	Aspect ratio of martensite
M_{S}	Martensite-start temperature
t	Bainitic plate thickness
T	Temperature
T_0	Temperature at which austenite and ferrite of the same composition have the same free energy
T_0'	As T_0, but accounting for the stored energy of ferrite
T_{h}	The temperature below which the nucleation of displacive transformation first becomes possible at a detectable rate
T_{N}^{γ}	Néel temperature of austenite
$\overline{V_{\mathrm{c}}}$	Average size of the compartment
V_γ	Average austenite grain volume
w_{i}^{γ}	Weight fraction of species i in phase γ

W_S	Widmanstätten ferrite start temperature
w_μ	Athermal frictional work for dislocation move
w_{th}	Thermal frictional work for dislocation move
$\bar{x}$	Average mole fraction of carbon in an alloy
x_i^α	Mole fraction of species i in phase α
x_m	Maximum carbon super-saturation permitted in ferrite, on thermodynamic grounds
$x_{T_0'}$	Carbon concentration given by the T_0' curve.
x^γ	Carbon concentration in austenite
$x^{\alpha\gamma}$	Mole fraction of carbon in ferrite which is in equilibrium or para-equilibrium with ferrite
$x^{\gamma\alpha}$	Mole fraction of carbon in austenite which is in equilibrium or para-equilibrium with ferrite
α	Ferrite
α_b	Bainitic ferrite
α_m'	Martensitic ferrite with bct structure
γ	Austenite
γ'	Carbon-enriched austenite
δ	Dilatational component of invariant-plane strain
ε	Martensitic ferrite with hcp structure
ε_0	Offset strain
μ	Shear modulus of austenite
σ	Surface energy
$\Delta\sigma$	Contribution to strength

bcc	Body-centered cubic
bct	Body-centered tetragonal
fcc	Face-centered cubic
TEM	Transmission electron microscope
TRIP	Transformation-Induced Plasticity
TTT	Time Temperature Transformation
XRD	X-ray diffraction

Chapter 1: Introduction

1.1 Aim of the Work

Martensite and bainite are generated by the displacive transformation of austenite. As a consequence, the structures have a fine scale through a simple process of heat treatment. It has been discovered that mixtures of bainitic platelets embedded in austenite can be produced as structures finer than carbon nanotubes, by suppressing the transformation temperature. This suppression is achieved particularly by enhancing the carbon concentration to about 1 wt%, which has the disadvantage that the materials cannot be welded.

The goal of the present work was to examine both theoretically and experimentally, whether the bainite-start (B_S) and martensite-start temperatures (M_S) can simultaneously be depressed using solutes other than carbon. It is necessary to suppress both temperatures in order to maintain a gap which permits bainite to predominate over martensite. In the course of doing this work, it was discovered that there exist no objective methods for determining transformation temperatures, to the required level of accuracy, using experimental data. Techniques therefore had to be developed which leave no room for misinterpretation and permit a clear assessment of uncertainties. This led to fundamental quantitative investigations of the factors influencing transformation start temperatures and the subsequent evolution of structure. The theory thus developed has been tested widely, both on an assembly of published data and using new experiments together with calculations. The original aim was therefore supplemented by a coherent experimental approach to the nature of the transformations.

1.2 Martensite in Steels

Bainitic and martensitic transformations have several common characteristics and the former cannot be explained without understanding martensite. The lowest temperature at which a bainitic microstructure can be obtained is limited by M_S, an

important practical limitation in this research. Therefore it is essential to understand the precision with which martensitic transformation can be predicted.

Atoms move in a disciplined manner during the change from the parent to the product structure as martensite grow. The transformation occurs not only in ferrous alloys but also in materials such as ceramics, solidified gases, polymers and even in protein (Czichos, 1989). The parent phase crystal structure, face-centered cubic (fcc), transforms into martensite which body-centered cubic (bcc), body-centered tetragonal (bct) or hexagonal close-packed (hcp) when the transformation conditions are appropriate. Martensite is technologically important in the steel industry because it can sometimes confer a good combination of strength and toughness so many commercial products utilise martensitic microstructure.

1.2.1 Characteristics of Martensite Transformation

1.2.1.1 Diffusionless Transformation

There is no doubt that martensitic transformation is diffusionless even for the interstitial atoms (Bhadeshia and Honeycombe, 2006). Martensite in steels inherits the carbon content of austenite resulting in supersaturated martensite. Martensite in carbon-containing steel is strong, and with the major contribution to hardness coming from carbon. Carbon in austenite occupies the octahedral interstitial sites. During martensitic transformation the carbon atoms are transferred into the cube-edge octahedral sites in martensite, which introduces tetragonality into the otherwise body-centered cubic lattice. In the martensite, the carbon in octahedral sites causes anisotropic distortion which is effective in inhibiting dislocation glide.

There is also indirect evidence that martensitic transformation is diffusionless (Bhadeshia and Honeycombe, 2006). The martensite interface can move as fast as 1100 m s^{-1}. Such a high speed cannot be sustained by diffusion. And the transformation temperature can be very low where diffusion is impossible within the time scale of the experiment.

1.2.1.2 Habit Plane

A habit plane is the interface plane between the austenite and martensite (plane abcd in Fig 1.1). A characteristic of the habit plane is that it is macroscopically invariant during transformation. An invariant plane means that any line on it is not changed in magnitude or direction during the transformation. Scratch experiments can prove that. If some scratches are made on the surface before the transformation, the formation of martensite causes a tilt on the surface with an accompanying displacement of the scratches. This tilt on the surface is the common phenomenon for displacive transformation. There would be no discontinuity in the intersection (e in Fig. 1.1). It means that the intersection line (line ab) between the habit plane and surface is invariant. Considering that the surface is an arbitrary plane to the martensite plate, the line ab is an arbitrary line of the habit plane. Therefore, any line in the habit plane is invariant and therefore, the habit plane is an invariant plane.

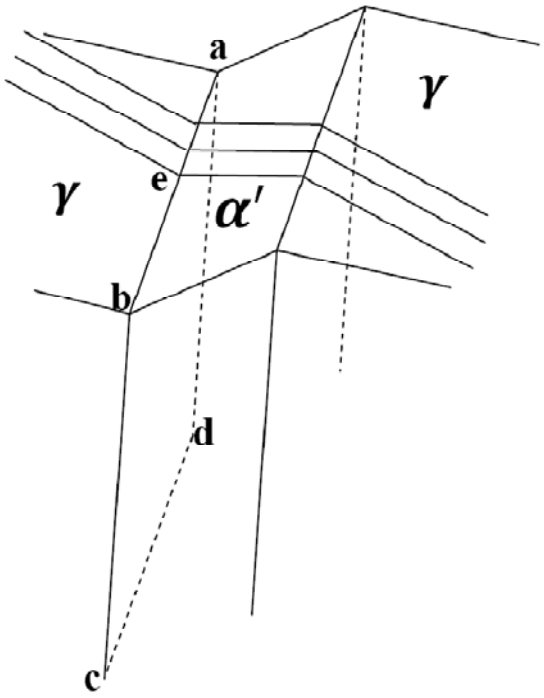

Fig. 1.1: Shape deformation of a martensite plate.

Habit planes of some alloys are shown in Table 1.1. It is known that habit plane changes approximately in sequence of $\{111\}_\gamma \rightarrow \{225\}_\gamma \rightarrow \{259\}_\gamma$ as carbon increases in steels. Another character of the martensite habit plane is the irrational indices. The habit plane is different according to the alloy system but their crystallographic indices are irrational except for hcp martensite (ε).

Table 1.1: Approximate habit planes of martensite (Nishiyama, 1978).

Alloy / wt %	Martensite Structure	Habit Plane
Fe - (0~0.4)C	bct	$\{111\}_\gamma$
Fe - (0.5~1.4)C	bct	$\{225\}_\gamma$
Fe - (1.5~1.8)C	bct	$\{259\}_\gamma$
Fe - 18Cr - 8Ni	hcp	$\{111\}_\gamma$

Another character of martensite is the large shear component of the shape deformation. Strain analysis can be done using surface relief, the shear component of the shape deformation is very large, 0.24 (Dunne and Wayman, 1971).

1.2.1.3 Orientation Relationship

Atoms move in disciplined manner during martensitic transformation so it follows that the parent and product phase should have an orientation relationship. Usually the close-packed planes are parallel or nearly parallel and the corresponding close-packed directions in those planes are parallel. Nishiyama and Wassermann relationship (NW, 1933; 1934) can be generated from Kurdjumov and Sachs relationship (KS, 1930) by a rotation of 5.26° about $[0\ 1\ 1]_\alpha$. GT represents Greninger and Troiano relationship (1949). The actual orientation relation is irrational.

KS $(1\ 1\ 1)_\gamma \parallel (1\ 1\ 0)_\alpha$ and $[\bar{1}\ 1\ 0]_\gamma \parallel [\bar{1}\ 1\ 1]_\alpha$ (1.1)

NW $(1\ 1\ 1)_\gamma \parallel (1\ 1\ 0)_\alpha$ and $[\bar{1}\ 0\ 1]_\gamma \parallel [0\ 0\ 1]_\alpha$ (1.2)

GT $(1\ 1\ 1)_\gamma \parallel (1\ 1\ 0)_\alpha$ (at 1°) and $[\overline{12}\ 17\ \bar{5}]_\gamma \parallel [\overline{17}\ 17\ 7]_\alpha$ (1.3)

1.2.2 Phenomenological Theory of Martensitic Transformation

The smallest strain to deform fcc to bcc is the Bain strain. Fig. 1.2 illustrates the Bain strain. The conventional fcc unit cell is shown in Fig. 1.2a. Alternatively one can construct a bct unit cell with a different set of basis vectors as shown in Fig. 1.2b. Contraction along $\mathbf{b_3}$ axis and uniform expansion along $\mathbf{b_1}$ and $\mathbf{b_2}$ axes would lead to a bcc unit cell. Bain strain naturally makes following orientation relationship:

$$[0\ 0\ 1]_\gamma \parallel [0\ 0\ 1]_\alpha \text{ and } [1\ \bar{1}\ 0]_\gamma \parallel [1\ 0\ 0]_\alpha \text{ and } [1\ 1\ 0]_\gamma \parallel [0\ 1\ 0]_\alpha \quad (1.4)$$

This Bain relationship is not correct considering observed orientation relationships as noted above.

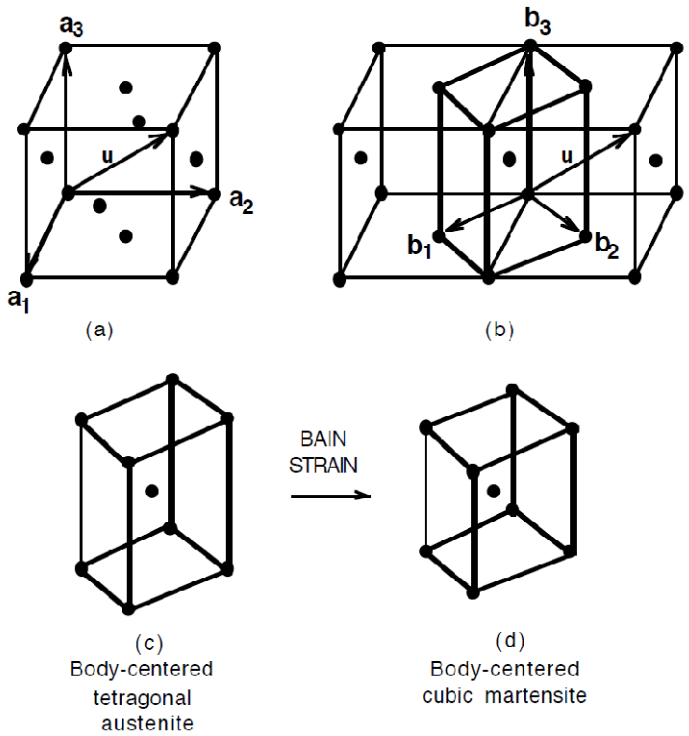

Fig. 1.2: (a) Conventional fcc unit cell. (b) Relation between fcc and bct cells of austenite. (c) bct cell of austenite. (d) Bain strain deforming the bct austenite lattice into a bcc martensite lattice. (Bhadeshia, 2001b)

Furthermore, the Bain strain is not an invariant-plane strain (IPS). As shown in section 1.2.1.2, the habit plane should be invariant. Bain strain converts the fcc lattice represented as a sphere into an ellipsoid (Fig. 1.3). Bain strain expands sphere along $\mathbf{a_1}$ and $\mathbf{a_2}$ axes so uniform expansion on $\mathbf{a_1}$-$\mathbf{a_2}$ plane (Fig. 1. 3a) and contraction along $\mathbf{a_3}$ axis (Fig. 1.3b). Therefore there is no line which is same in magnitude and direction as a result of Bain deformation. Two lines, a'b' and c'd', preserve magnitude but are changed in direction. If rigid body rotation is allowed to the Bain strain, it is possible to make one line invariant as shown Fig. 1.3c. Line c'd' is invariant in Fig. 1.3c. It has the same magnitude and direction. Therefore, a combination of a rigid body rotation and Bain strain can be an invariant-line strain, and at the same time generates the observed irrational orientation relationship. However, the shape deformation due to martensitic transformation is an invariant-plane strain, which requires further explanation.

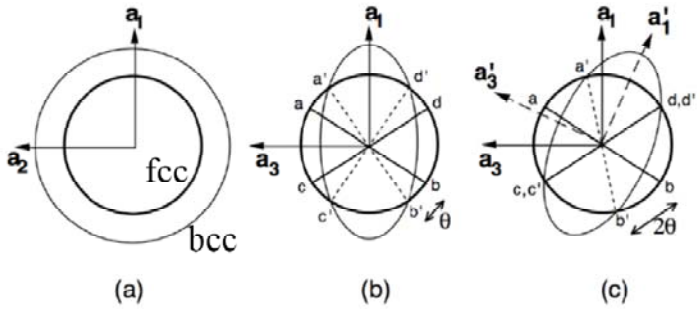

Fig. 1.3: fcc sphere changes to ellipsoid bcc by Bain strain. (a) View from $\mathbf{a_3}$ axis and (b) from $\mathbf{a_2}$ axis. (c) The invariant-line strain obtained by combining the Bain strain with a rigid body rotation is shown (Bhadeshia, 2001b).

The phenomenological theory of martensitic transformation appeared in 1953-54 (Wechsler *et al*., 1953; Bowles and Mackenzie, 1954a, b; Mackenzie and Bowles, 1954) and is well-described elsewhere (Bhadeshia, 2001b; Christian, 2002). The mathematical theory and can explain the irrational habit plane, invariant-plane strain character of the shape deformation and orientation relationship of martensite. The concept of the theory is shown in Fig. 1.4. As mentioned previously, Bain strain (**B**)

combined with rigid body rotation (**J**) can be an invariant-line strain to change fcc to bcc. The lines through x and w which are perpendicular to the paper in Fig. 1.4c are invariant-lines. **JB** deformation also can be accomplished by combining two shear strain (**P** and **Q**) because invariant-line strain always is equivalent to a combination of two invariant-plane strains. Lattice-invariant deformation such as slip or twin can be applied to macroscopically make it invariant-plane strain. As a result, whole deformation remains an invariant plane in macroscopically. The plane containing line wx which is perpendicular to the paper is the invariant-plane. This explains why the habit plane of α' is irrational because the amount of lattice-invariant deformation needed to recover the correct shape is not usually rational. Internal $\{2\ 1\ 1\}_{\alpha}$ twins in the martensite were experimentally observed as had been predicted by the theory (Kelly and Nutting, 1960; Shimizu and Nishiyama, 1972). Generally, low-carbon steel (high M_S) tends to become slipped martensite and high-carbon or high-nickel steels (low M_S) are easy to be internal twinned martensite. There are some explanations considering temperatures or strength or austenite, but the reason is not clearly understood.

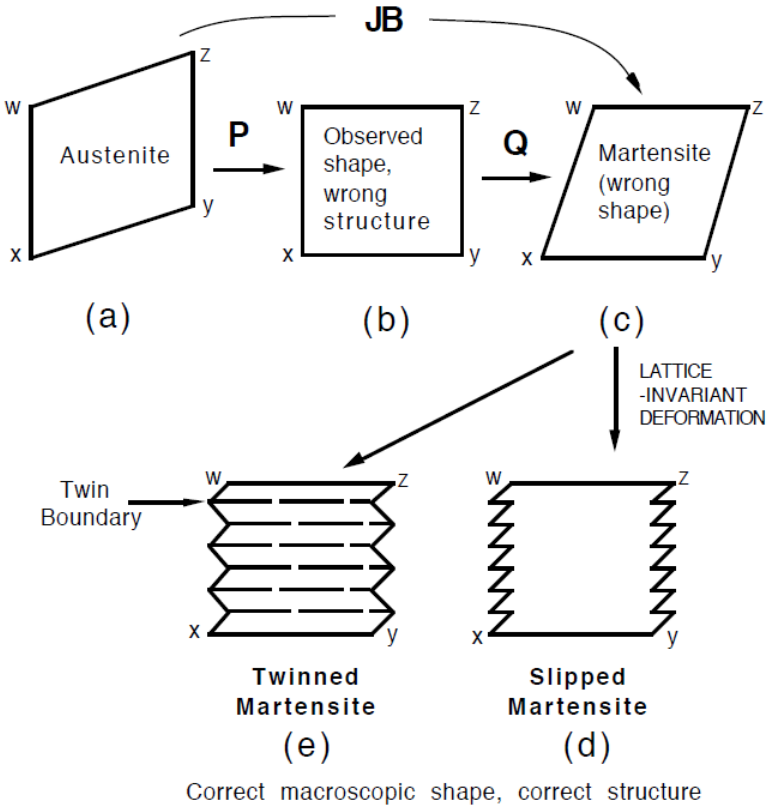

Fig. 1.4: Schematic illustration of the phenomenological theory of martensite. (a) represents the austenite crystal and (c), (d) & (e) all have a bcc structure. (b) has a structure between fcc and bcc. The dashed lines in (e) are coherent twin boundaries. (Bhadeshia, 2001b)

An example of the mathematical development of the theory is as follow (Bhadeshia, 2001b)

1) Lattice-invariant mode should be assumed, for example, $(1\ 0\ 1)[1\ 0\ \bar{1}]_{\gamma}$ shear which corresponds to $(1\ 1\ 2)[\bar{1}\ \bar{1}\ 1]_{\alpha}$ twinning.
2) Invariant line in Fig. 1.4(c) calculated, one of two possible lines is $[\gamma;\mathbf{u}]$ = [-0.671120 -0.314952 0.671120]. The lines lie on $(1\ 1\ 2)_{\alpha}$ and have same magnitude after Bain strain.

3) Invariant normal calculated, one the two possible normal is (**h**;γ)=(0.539127 0.647058 0.539127). The normal contain $[\bar{1}\ \bar{1}\ 1]_\alpha$ and have same magnitude after Bain strain.

4) Calculated rotation matrix and **S**=**PQ**=**JB**

$$(\gamma\ \mathbf{J}\ \gamma)=\begin{pmatrix} 0.990534 & -0.035103 & 0.132700 \\ 0.021102 & 0.994197 & 0.105482 \\ -0.135633 & -0.101683 & 0.985527 \end{pmatrix} \quad (1.5)$$

$$(\gamma\ \mathbf{P}\ \gamma)\ (\gamma\ \mathbf{Q}\ \gamma)=\begin{pmatrix} 1.125317 & -0.039880 & 0.106601 \\ 0.023973 & 1.129478 & 0.084736 \\ -0.154089 & -0.115519 & 0.791698 \end{pmatrix} \quad (1.6)$$

5) Co-ordinate transformation matrix which represents the orientation relationship

$$(\alpha\ \mathbf{J}\ \gamma)=(\alpha\ \mathbf{C}\ \gamma)(\gamma\ \mathbf{S}\ \gamma)^{-1}=\begin{pmatrix} 1 & \bar{1} & 0 \\ 1 & 1 & 0 \\ 0 & 0 & 1 \end{pmatrix}\begin{pmatrix} 0.87189 & 0.01857 & -0.119388 \\ -0.03089 & 0.87512 & -0.089504 \\ 0.16518 & 0.13130 & 1.226811 \end{pmatrix} \quad (1.7)$$

$$= \begin{pmatrix} 0.902795 & -0.856546 & -0.029884 \\ 0.840997 & 0.893694 & -0.208892 \\ 0.165189 & 0.131307 & 1.226811 \end{pmatrix} \quad (1.8)$$

Eq. 1.8 show that

$$(1\ \ 1\ \ 1)_\gamma = (0.010561\ \ 0.984639\ \ 0.983036)_\alpha \quad (1.9)$$

$$[\bar{1}\ \ 0\ \ 1]_\gamma = [-0.932679\ \ -1.049889\ \ 1.061622]_\alpha \quad (1.10)$$

This orientation relationship is consistent with experimental observations.

6) Invariant plane of **P**, habit plane of the transformation, can be calculated using (γ **S** γ) and invariant plane of **Q**.

$$(\mathbf{p};\ \gamma) = (0.197162 \quad 0.796841 \quad 0.571115) \quad (1.11)$$

7) **P** and **Q**

$$(\gamma\ \mathbf{P}\ \gamma)=\begin{pmatrix} 0.990134 & -0.039875 & -0.028579 \\ 0.032037 & 1.129478 & 0.092800 \\ -0.028583 & -0.115519 & 0.917205 \end{pmatrix} \quad (1.12)$$

$$(\gamma\ \mathbf{Q}\ \gamma)=\begin{pmatrix} 1.132700 & 0.000000 & 0.132700 \\ 0.000000 & 1.000000 & 0.000000 \\ -0.132700 & 0.000000 & 0.867299 \end{pmatrix} \quad (1.13)$$

8) Shear and dilatational strain of (γ **P** γ) is 0.220 and 0.037 respectively which are typical values found in experiments.

It is simple for hcp martensite where the volume change is small. The strain along the $\mathbf{y_2}$ axis is zero. Therefore pure strain with rigid body rotation could be invariant plane strain (Fig. 1.5). The combined deformation corresponds to simple shear on $(1\ 1\ 1)[1\ 1\ \bar{2}]_\gamma$ of which strain is half of twinning. Hcp martensite forms via simple shear, the habit plane is rational and fully coherent.

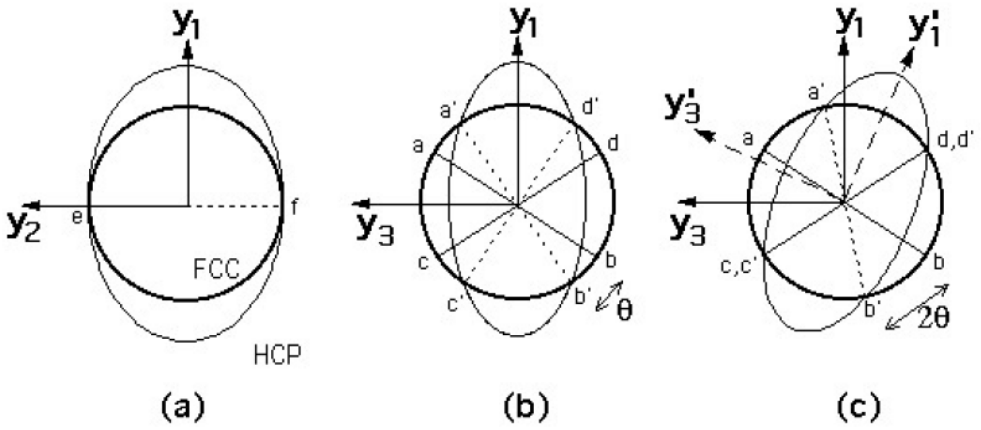

Fig. 1.5: Undeformed crystal represented initially as a sphere of diameter ef. (c) illustrates that a combination of pure strain with a rigid body rotation gives an invariant-plane strain. (Bhadeshia, 2001b)

Austenite stacking sequence for the clos-packed planes is ABCABC. It changes to AB'AB'AB' after homogeneous shear strain of which is half the twinning strain. The scheme is shown in Fig. 1.6. B' represents the center position between B and C.

Therefore additional inhomogeneous strain which moves atoms from B' to B should be introduced for every two layers. These additional movements of atoms are called *shuffles*.

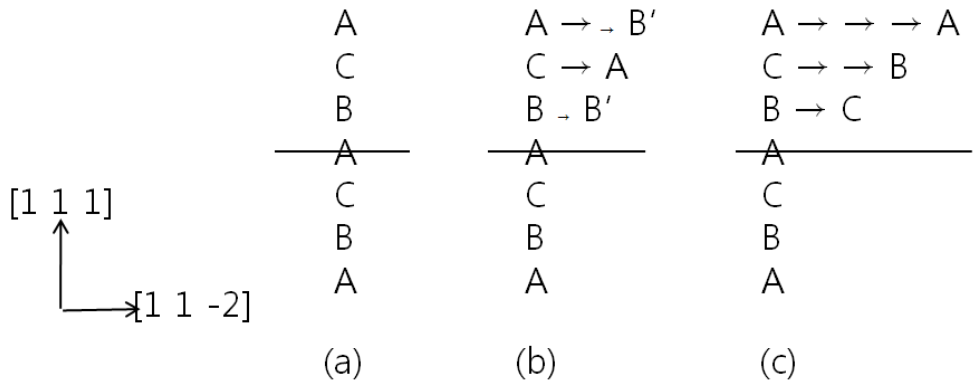

Fig. 1.6: (111) austenite stacking. (a) Undeformed austenite (b) austenite after shear strain of which strain is half of twinning and (c) twinned austenite

1.2.3 Martensite Nucleation Theory

The phenomenological theory explains well the crystallography of martensite, such as the orientation relationship, invariant habit plane and irrationality. It also successfully predicted internal twins in martensite. The name of the theory is phenomenological because it considers only the initial and final state of the transformation. Therefore it has some limitations. There are some known characters of martensite which are not easy to explain by the phenomenological theory. One of them is heterogeneous nucleation (Cao *et al*., 1990). Martensite nucleation is deeply related with the crystal defects and it is hard to understand under phenomenological theory scheme because the theory is macroscopic. Martensite transformation is athermal in many cases. Once it nucleates, it grows rapidly and the number of activated nuclei is dependent on undercooling. The athermal character of martensite requires complement any theory which describe atoms' movement during the transformation.

One such theory dates from 1976, Olson and Cohen's mechanism involves the spontaneous dissociation of specific dislocation defects (Olson and Cohen, 1976). The dissociation of a perfect dislocation in $\{111\}_{fcc}$ into two Shockley partial dislocations results in two layers of hcp phase. Therefore such faulting on every two planes leads to fcc→hcp structure change (Fig. 1.7).

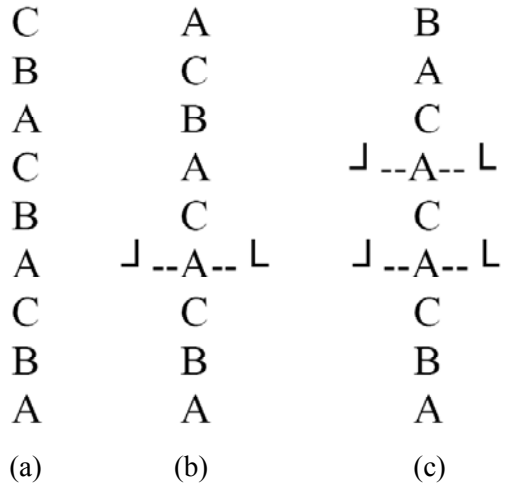

Fig. 1.7: Stacking sequence of close packed planes in fcc stacking fault structures. (a) Normal fcc stacking. (b) Dissociations of a dislocation. (c) Dissociation of another dislocation introduces two more layers of hcp crystal.

The free energy per unit area of fault plane is

$$G_{\mathrm{F}} = n\rho_{\mathrm{A}}(\Delta G_{\mathrm{CHEM}} + G_{\mathrm{STRAIN}}) + 2\sigma \tag{1.14}$$

where n is the number of close packed planes participating in the faulting process, ρ_{A} is the density of atoms in a close packed plane, ΔG_{CHEM} is chemical free energy change from fcc to hcp, G_{STRAIN} is strain energy and σ is surface energy which is a function of n. The energy of the faulted region can be negative when the chemical energy change can accommodate the strain energy and surface energy. Eq. 1.14 is used widely for calculating stacking fault energy with assumed surface energy or vice versa. Such calculations should be done with caution because measuring faulting or surface energy is difficult and imprecise. For the dissociation

of dislocations of infinite length, the total free energy per unit length (normal to the dissociation direction) of the embryo is the sum of the dislocation energy and fault energy contributions.

$$G(r) = E_{\perp}(r) + G_{\mathrm{F}} \cdot r \tag{1.15}$$

where $E_{\perp}(r)$ is dislocation energy and r is distance between two partial dislocations. $E_{\perp}(r)$ decreases monotonically with increasing r, they push each other. The total energy is represented schematically in Fig. 1.8. Dissociated partial dislocations spontaneously separate when $G_{\mathrm{F}} \leq 0$ because that would decreases total energy. There is an equilibrium separation, r_{eq}, when $G_{\mathrm{F}}>0$. Therefore,

$$G_{\mathrm{F}} \leq 0 \tag{1.16}$$

is the criterion for martensite nucleation and growth. Crystal defects spontaneously start to dissociate as the temperature decreases and so the chemical driving force can supply strain and surface energy.

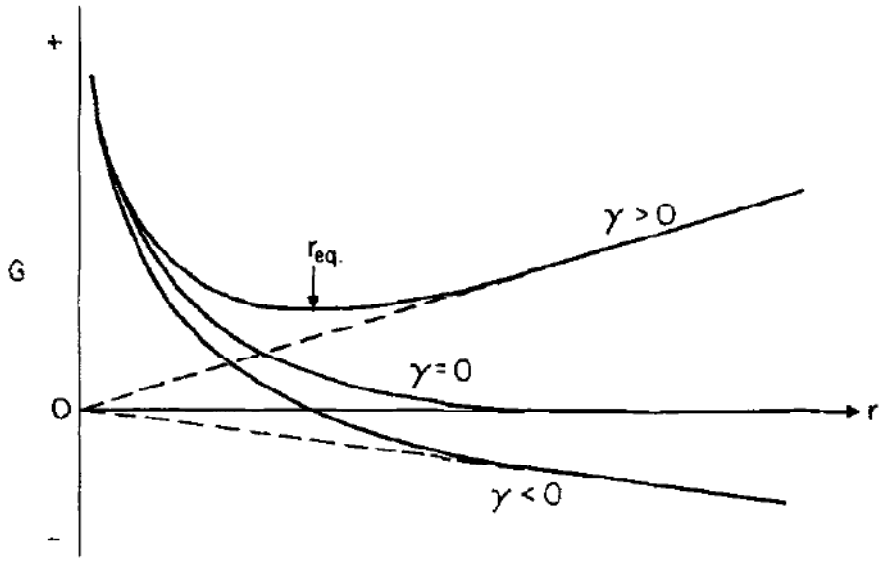

Fig. 1.8: Schematic representation of total free energy as a function of the separation of the partial dislocations bounding a faulted region for the here condition (Olson and Cohen, 1976). Reprinted with kind permission from Springer Science+Business Media.

The temperature where G_F becomes zero corresponds to M_S, and it depends on the number of planes participating faulting. Fig. 1.9 shows a schematic representation of the temperature dependence of the fault energies associated with the dissociation of defects of various thicknesses. When a larger number of dislocations is properly arranged, it is easy for them to be dissociated and they dissociate at higher temperatures. Potential nuclei's temperature where G_F becomes zero are different, they are activated at different temperatures and spontaneously grow. It explains the athermal character of martensite. The first step of Olson and Cohen's model for bcc martensite is also faulting on the close-packed planes. The whole steps of the transformation are shown in Fig. 1.10.

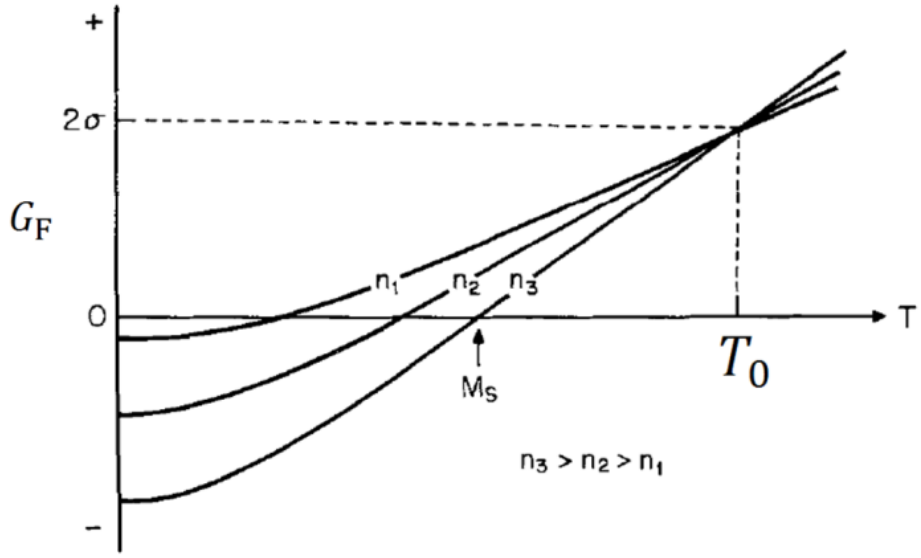

Fig. 1.9: Schematic representation of the temperature dependence of the fault energy for three thicknesses. T_0 represents the temperature where free energy change for transformation is zero (Olson and Cohen, 1976). Reprinted with kind permission from Springer Science+Business Media.

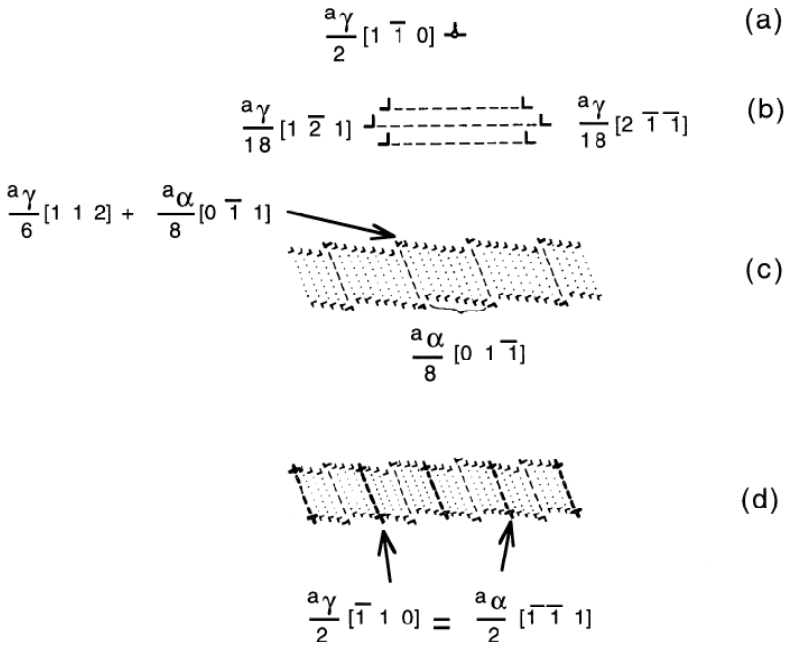

Fig. 1.10: Olson and Cohen model for the nucleation of bcc martensite. (a) Perfect screw dislocation in austenite. (b) Three-dimensional dissociation over a set of three close packed planes. (c) Relaxation of fault to body-centered cubic structure with the introduction of partial dislocations in the interface. (d) Addition of perfect screw dislocations which cancel the long range strain field of the partials introduced in (c). (Bhadeshia, 2001a)

1.2.4 Martensite-Start Temperatures

Martensite starts to from at the temperature where sufficient driving force is available during quenching. The martensite-start temperature is the highest temperature where the transformation is possible, and the lowest temperature where bainite can dominate the microstructure. Therefore it should be depressed for developing low-temperature bainite, and understanding and prediction of M_S are required in developing low-temperature bainite.

1.2.4.1 Prediction of Martensite-Start Temperature

The easiest way to predict M_S is using experimental regression equations. Some of them are shown in Table 1.2. These equations represent the composition dependence of M_S. They are basically linear weighted sums of alloying terms, but can include arbitrary non-linear terms or binary interaction terms. These equations have been developed based on a limited number of experiments, so have difficulties when applied to different alloy systems and cannot get accurate result when applied beyond the range of the equation developed. These kinds of equations hardly help to understand martensite transformation. However they can indicate the effect of elements on M_S so developing and using of them is easy and convenient.

Table 1.2: Different formulae for the estimation of the M_S in steels.

M_S (K), compositions are in wt %	Product	Reference
772 - 316.7C - 33.3Mn - 11.1Si - 27.8Cr - 16.7Ni - 11.1Mo - 11.1W	$\alpha`$	Payson and Savage, 1944
811 - 361C - 38.9Mn - 38.9Cr - 19.4Ni - 27.8Mo	$\alpha`$	Grange and Stewart, 1945
772 - 300C - 33.3Mn - 11.1Si - 22.2Cr - 16.7Ni - 11.1Mo	$\alpha`$	Nehrenberg, 1945
834.2 - 473.9C - 33Mn - 16.7Cr - 16.7Ni - 21.2Mo	$\alpha`$	Steven and Haynes, 1956
785 - 453C - 16.9Ni - 15Cr - 9.5Mo + 217$(C)^2$ - 71.5(C)(Mn) - 67.6(C)(Cr)	$\alpha`$	Andrews, 1965
667 - 710.5(C+1.4N) - 18.5Ni - 12.4Mn - 8.4Cr + 13.4Si - 1.6Mo – 22.7Al + 11.6(C+1.4N)(Mo+Cr+Mn) - 3.7$\{(Ni+Mn)(Cr+Mo+Al+Si)\}^{1/2}$	ε	Dai *et. al*., 2004

M_S can be estimated using the statistical relation with T_0. M_S is related with driving force and T_0 is the temperature where driving force is zero. Therefore there

must be a relation between M_S and T_0. T_0 can be calculated using thermodynamic calculation, an example is (Wang *et al.*, 2000).

$$M_S(℃) = 1.183T_0 - 434 \quad (1.17)$$

It is possible to calculate M_S using eq. 1.17 and thermodynamics. However there is no fundamental reason for a linear relationship between M_S and T_0.

Recently, a more refined statistical approach has been made which utilises an artificial neural network (Wang *et al*., 2000; Capdevila *et. al*., 2003; Sourmail and Garcia-Mateo, 2005a- b). Neural network is an explicit combination of transfer functions and weights (Bhadeshia, 2009). Experimental equations usually use functions which are already assumed such as linear or second order polynomial function. The relation is determined by input data in neural network analysis rather than a pre-determined function. Therefore it is able to capture non–linear, non–periodic functions of immense complexity without bias on the form of the function. This method also associates an uncertainty with each prediction. Insufficient data are associated with large uncertainties, which the user must then assess to see whether the prediction is useful or not (Bhadeshia, 2009). One can analyse on a range where experimental data are rare with clear indication uncertainty. A neural network can analyse large quantities of complex data, a network model can cover wide composition range. Fig. 1.11 and 1.12 show examples of neural network predictions. It is better than linear regression equations in predictions (Wang *et. al.*, 2000). And it can reveal complex phenomena, for example the Mn-Si interaction effect on M_S (Fig. 1.12). The predictions in Fig. 1.12 don't include uncertainties which are should be presented. Uncertainties are needed to assess the predictions.

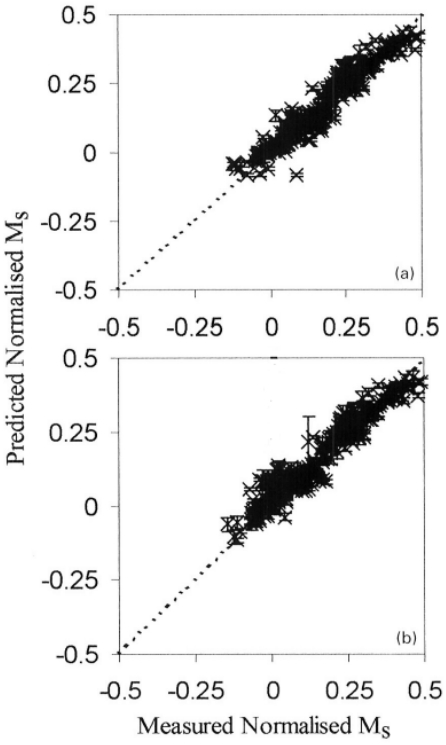

Fig. 1.11: Comparison with measured and predicted M_S for (a) training data and (b) test data. (Capdevila *et al.*, 2003)

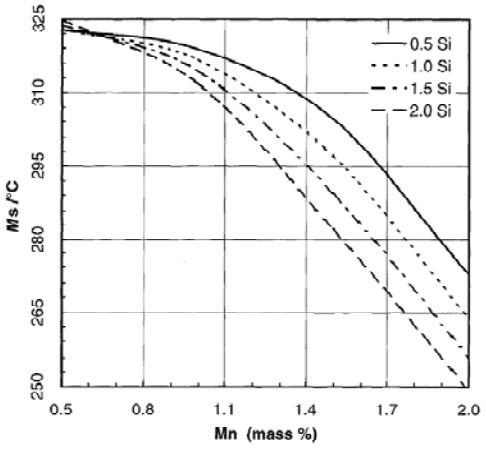

Fig. 1.12: Influence of Si-Mn interaction on M_S, predicted by neural network. Base alloy is Fe-0.4C-xSi-yMn-1.0Cr-0.5Mo wt % (Wang *et. al.*, 2000).

Neural network analysis is useful in predicting M_S and complex effects which are not well revealed in limited number of experiments. However it cannot provide the fundamental physics for the predictions. Transformation start temperatures should be related with thermodynamics. It should be possible to estimate M_S through thermodynamic calculations. The concept is simple. Martensitic transformation is possible when the chemical driving force for the diffusionless transformation, $|\Delta G^{\gamma\rightarrow\alpha}|$, is large enough. The required driving force for stimulating martensitic transformation is the critical driving force for martensite nucleation, $\left|\Delta G_C^{\gamma\rightarrow\alpha}\right|$. A large driving force is required to accommodate the strain energy, interface energy, frictional work and so on. The basic concept is represented in Fig. 1.13.

$$\Delta G^{\gamma\rightarrow\alpha} = \Delta G_C^{\gamma\rightarrow\alpha} \text{ at } M_S \tag{1.18}$$

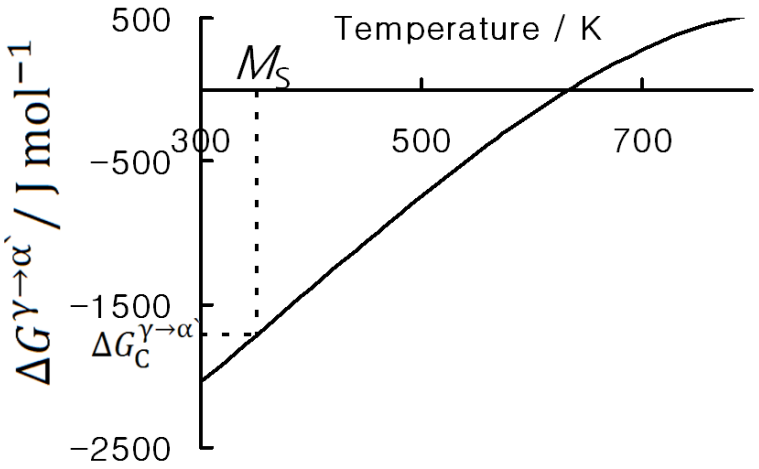

Fig. 1.13: Calculation of martensite start temperature as point where chemical driving force for transformation of austenite without composition change achieves critical value (Cool and Bhadeshia, 1996)

Accepting equation 1.18, the accuracy of the M_S calculation can be improved in two ways. One is improving the accuracy of calculation of diffusionless driving force. The other is an improved estimation of the critical driving force. It is easy to

use the previous efforts for improving accuracy of driving force because of the presence of commercial thermodynamic databases and software such as ThermoCalc or MTDATA. So, the remained problem is improved estimation of critical driving force.

Bhadeshia (1981a) calculated the $\Delta G_{\mathrm{C}}^{\gamma \rightarrow \alpha`}$ as only a function of carbon content, it varies between 1100 and 1400 J mol^{-1}. The application of the calculation to low-alloy steel is shown in Fig. 1.14.

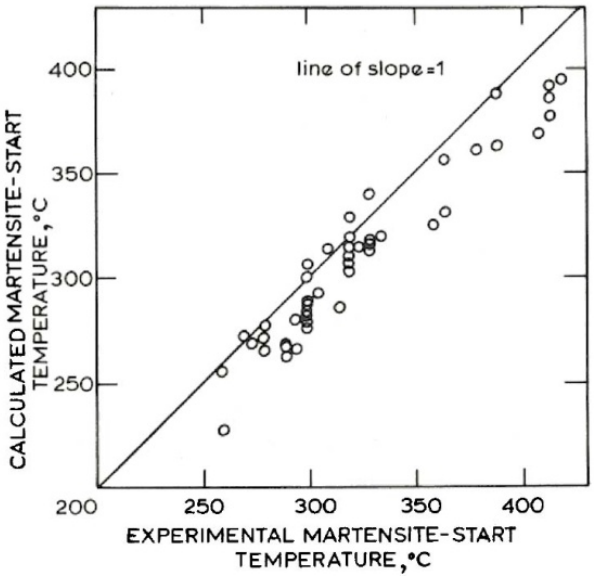

Fig. 1.14: Comparison between computed and experimental M_{S} temperatures of various low-alloy steels. Critical driving force is estimated as only a function of carbon (Bhadeshia, 1981b).

Hsu (1985) focused on the linear relationship between the yield strength of austenite and M_{S}. Martensite transformation accompany large shear strain as shown earlier, he derived the shearing energy, U_{S}.

$$U_{\mathrm{S}} = \frac{1}{2} V \varphi \sigma_{\gamma} = 2.1 \sigma_{\gamma} \ \ [\mathrm{J\ mol^{-1}}] \qquad (1.19)$$

where V is the deformation molar volume in cm^3 mol^{-1}, φ is strain accompanying the martensite transformation equals to 0.28 and σ_{γ} is yield strength of austenite in

MPa. Considering stored energy in martensite and austenite, surface energy and dilatational energy which is insensitive to composition, he estimated critical driving force;

$$\left|\Delta G_{\mathrm{C}}^{\gamma\rightarrow\alpha}\right| = 2.1\sigma_{\gamma} + 900 \ \ [\mathrm{J\ mol^{-1}}] \tag{1.20}$$

The theory is elegant in that it relates the fundamental mechanism of the transformation to M_{S}, but there are some errors in derivation. Considering macroscopic strain of the shape deformation, 0.28 was used for φ, but it is plastic strain. Therefore, 1/2 should not be in eq. 1.19. The shear strain energy also ignores the shape. The errors are compensated later because of roughly estimated constant energy term, 900 J mol^{-1}.

Martensite nucleation starts from faulting on the close-packed planes in the Olson-Cohen model as described in earlier. The fault plane energy becomes negative and leads eventually to barrierless martensite nucleation at sufficient driving force. However, interface dislocations experience a force which interferes with the movement of dislocations. Therefore, the critical condition for semicoherent nucleation is then given by a balance between the negative fault energy and the interfacial frictional work; (Ghosh and Olson, 1994)

$$G_{\mathrm{F}} = n\rho_{\mathrm{A}}(\Delta G_{\mathrm{CHEM}} + G_{\mathrm{STRAIN}}) + 2\sigma = -(w_{\mu} + w_{\mathrm{th}}) \tag{1.21}$$

$$-\Delta G_{\mathrm{CHEM}} = G_{\mathrm{STRAIN}} + \frac{2\sigma}{n\rho_{\mathrm{A}}} + (w_{\mu} + w_{\mathrm{th}}) \tag{1.22}$$

where w_{μ} and w_{th} are athermal and thermal frictional work respectively. Thermal frictional work can be ignored at high temperatures (>300 K) and athermal frictional work was modeled as a function of composition. Assuming strain and interface energy is insensitive to temperature and composition,

$$-\Delta G_{\mathrm{C}}^{\gamma\rightarrow\alpha} = K_1 + \mathrm{w}_{\mu}(X_{\mathrm{i}}) \tag{1.23}$$

K_1 includes strain and interface energy. Based on theoretical and experimental results, frictional work modeled as a function proportional to $(X_i)^{0.5}$. They derived proportion coefficients for several elements. Elements then were cartegorised into four groups according to strengthening coefficient. The terms were added by

Pythagorean-type laws among element in same groups, with linear summation between groups.

$$-\Delta G_{\mathrm{C}}^{\gamma\rightarrow\alpha`} = K_1 + \sqrt{\sum_i \left(K_\mu^i X_i^{0.5}\right)^2} + \sqrt{\sum_j \left(K_\mu^j X_j^{0.5}\right)^2} + \sqrt{\sum_k \left(K_\mu^k X_k^{0.5}\right)^2} + K_\mu^{\mathrm{Co}} X_{\mathrm{Co}}^{0.5} \quad (1.24)$$

where *i*=C, N; *j*=Cr, Mn, Mo, Nb, Si, Ti, V and *k*=Al, Cu, Ni, W. K_1 is 1100 J mol^{-1}. Cool and Bhadeshia (1996) used eq. 1.24 for predicting M_S for power plant steels. They used linear sum for every element rather than Pythagorean-type and realised that modifying K_1 to 683 J mol^{-1} gives better predictions. Eq. 1.24 doesn't consider the dependence of strain, interface energy and frictional work on temperature and shear modulus. Shear modulus of austenite has also been modeled as function of chemical composition and temperature (Ghosh and Olson, 2002).

$$\mu = \left(9.2648 + \sum x_j \left(\frac{\mathrm{d}\mu}{\mathrm{d}x_j}\right)\right)(1 - 7.39921 \times 10^{-7} T^2 + 3.317 \times 10^{-10} T^3) \times 10^{10}\ \mathrm{N\ m^{-2}} \quad (1.25)$$

where T is temperature in K. Eq. 1.24 was further improved by using eq. 1.25 (Ghosh and Olson, 2000). It was assumed that temperature dependence of strain, interface energy and frictional work is similar with that of shear modulus.

$$K_1 = K_1{}^{\mathrm{STRAIN}}\mu \quad (1.26a)$$

$$\sigma = K^\sigma \mu \quad (1.26b)$$

$$w_\mu = K^\mu X_j^{0.5}\, \mu \quad (1.26c)$$

New parameters were got based on eq. 1.23, eq. 1.26, experimental M_S measurements and new database. Four element groups in original research was changed to three groups, final form of critical driving force for martensite nucleation is;

$$-\Delta G_{\mathrm{C}}^{\gamma\rightarrow\alpha`} = K_1{}^{\mathrm{STRAIN}}\mu + \sqrt{\sum_i \left(k_\mu^i X_i^{0.5}\right)^2} + \sqrt{\sum_j \left(k_\mu^j X_j^{0.5}\right)^2} + k_\mu^{\mathrm{Co}} X_{\mathrm{Co}}^{0.5} \quad (1.27)$$

where k_μ's are $K_\mu\mu$ and *i*=Al, C, N, Cr, Mn, Mo, Nb, Si, Ti, V, W and *j*=Cu, Ni. Examples of M_S prediction by Ghosh-Olson model are shown in Fig. 1.15.

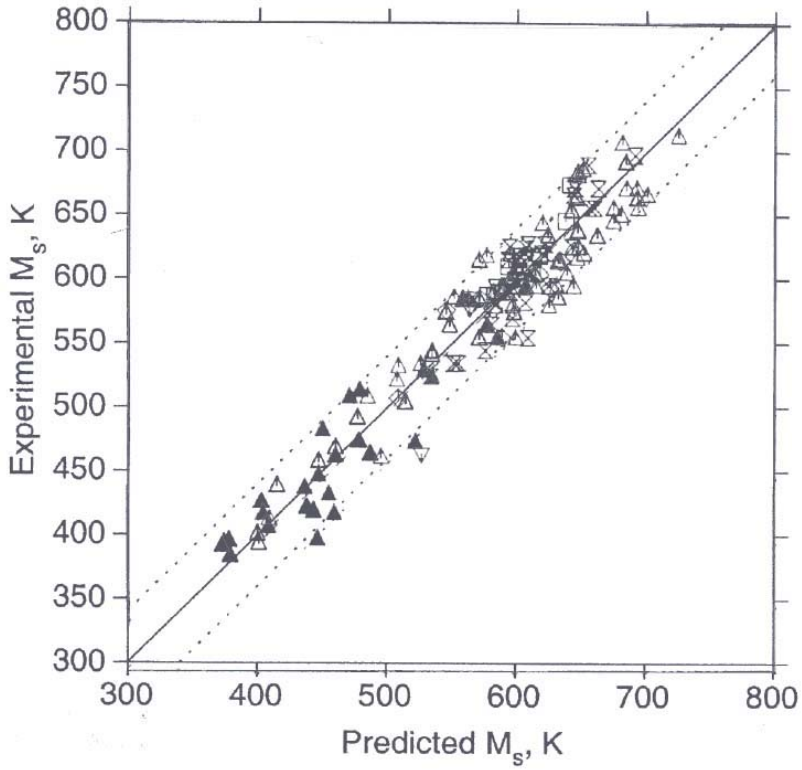

Fig. 1.15: Comparison between the experimental and predicted M_S by Ghosh-Olson model. Two dashed lines represents the limit of ± 40 K (Ghosh and Olson, 2001). Reprinted with kind permission from Springer Science+Business Media.

1.2.4.2 Measurements of Martensite-Start Temperature

M_S can be measured by investigating heat flow, ultrasonic wave velocity, resistivity, internal friction, length change and so on according to temperature. Dilatometry is the method most widely used. Ambiguity in detecting M_S in dilatometry was recognized and a new objective method was developed (Yang and Bhadeshia, 2007). Previous rough estimation methods can lead to different detection of transformation temperatures even with the same data.

The offset method is used routinely in defining the proof strength of materials when the stress–strain curve is smooth, making it difficult to define the deviation

from elastic deformation. In the case of a tensile test, it is conventional to offset the test line by a strain of 0.2 % in order to define the proof strength. A similar procedure could be followed for martensite as illustrated in Fig. 1.16.

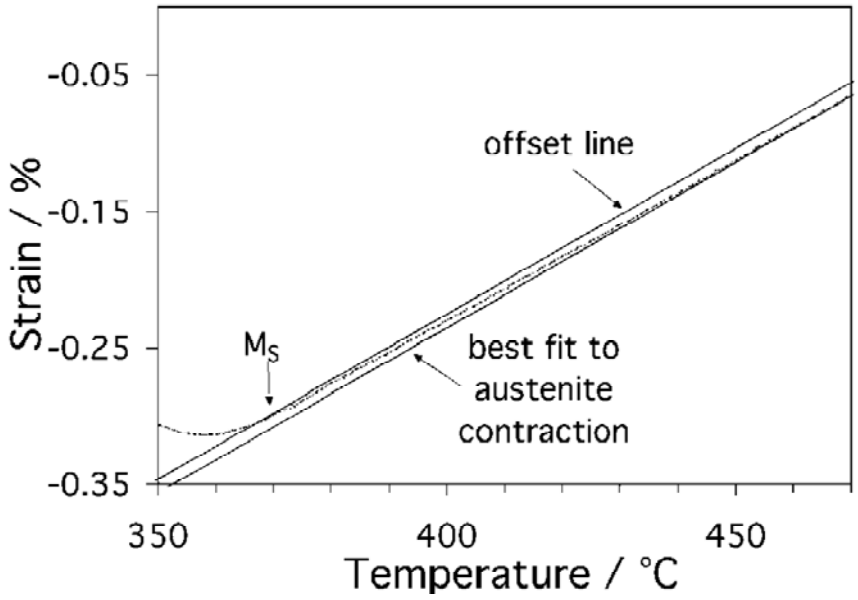

Fig. 1.16: Offset method illustrated (Yang and Bhadeshia, 2007).

The question then arises as to the magnitude of the transformation strain that should be used as the offset from the thermal contraction curve of austenite in order to determine the M_S. A transformation strain due to 1 vol. % martensite can be set as the value of the offset at which M_S is measured. They used a strain of 1.21×10^{-3}, which is some two orders of magnitude greater than the noise in the instrument and should be sufficient for the offset line to intersect the experimental curve in a region of sufficient curvature, thus ensuring a reliable measure of M_S. The transformation strain depends of course on the alloy studied. The strain cannot be measured directly from the dilatometer curve since the martensite reaction may not reach completion at the point where the experiment is terminated. The critical strain corresponding to 1 vol. % martensite can be calculated if the lattice parameters a_γ

and a_α of austenite and martensite respectively are known. The following equations are available from compiled data to estimate a_α in nm (Bhadeshia *et al*., 1991).

$$a_\alpha = 0.28664 + [(a_{\mathrm{Fe}} - 0.0279\, x_{\mathrm{C}}^{\alpha})^2 (a_{Fe} - 0.2496\, x_{\mathrm{C}}^{\alpha}) - a_{\mathrm{Fe}}^3]/(3\, a_{\mathrm{Fe}}^2) - 0.003\, x_{\mathrm{Si}}^{\alpha} + 0.006\, x_{\mathrm{Mn}}^{\alpha} + 0.007\, x_{\mathrm{Ni}}^{\alpha} + 0.031\, x_{\mathrm{Mo}}^{\alpha} + 0.005\, x_{\mathrm{Cr}}^{\alpha} + 0.0096 x_{\mathrm{V}}^{\alpha} \quad (1.28)$$

where x_i^{α} represents the mole fraction of species i in phase α. The lattice parameter of pure iron a_{Fe}=0.28664 nm. The equation applies at room temperature (25 ℃). The parameter for austenite in nm at room temperature is given by (Dyson and Holmes, 1970)

$$a_\gamma = 0.3573 + \sum c_{\mathrm{i}} w_{\mathrm{i}}^{\gamma} \quad (1.29a)$$

where w_{i} represents weight fraction and

$$\sum c_{\mathrm{i}} w_{\mathrm{i}}^{\gamma} = 3.3 \times 10^{-1} w_{\mathrm{C}}^{\gamma} + 9.5 \times 10^{-3} w_{\mathrm{Mn}}^{\gamma} + 2 \times 10^{-3} w_{\mathrm{Ni}}^{\gamma} + 6 \times 10^{-3} w_{\mathrm{Cr}}^{\gamma} + 3.1 \times 10^{-2} w_{\mathrm{Mo}}^{\gamma} + 1.8 \times 10^{-2} w_{\mathrm{V}}^{\gamma} \quad (1.29b)$$

Given that the austenite unit cell contains 4 iron atoms and that of martensite 2 per cell, the offset strain ε_0 corresponding to a specified value of martensite fraction V is given by

$$(1 + \varepsilon_0)^3 = a_\gamma^{-3} [2V a_\alpha^3 + (1 - V)\, a_\gamma^3] \quad (1.30)$$

Dilatometric data are interpreted by defining the first onset of transformation to be that at which a critical strain is achieved relative to the thermal contraction of the parent phase. The critical strain is calculated for 1 vol. % martensitic transformation assuming that the latter occurs at room temperature, by using equations for the lattice parameters of austenite and martensite. This ensures that the method is reproducible.

1.3 Bainite in Steels

1.3.1 Morphology

Bainite is a non-equilbrium transformation product of austenite which forms by cooling at rates such that reconstructive transformations such as pearlite are not possible and yet, the cooling is sufficiently slow to avoid diffusionless transformation into athermal martensite. Bainitic microstructures are generally described as non-lamellar aggregates of carbides and plate-shaped ferrite. Bainite can be classified according to its morphology as upper or lower bainite as shown in Fig. 1.17. Upper bainite consists of clusters of platelets of ferrite which share identical crystallographic orientation which are intimately connected to the parent austenite phase in which they grow. Elongated cementite particles decorate the boundaries of these plates; the amount and continuity of the cementite layer depends on the steel carbon concentration.

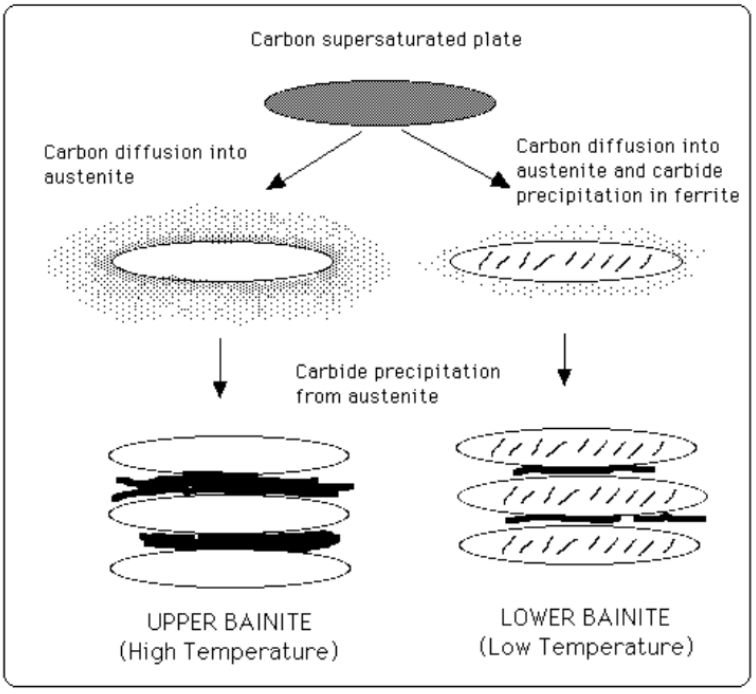

Fig. 1.17: Illustration of upper and lower bainite showing the main differences in carbon partitioning and precipitation behaviours (Takahashi and Bhadeshia, 1990).

Fully carbon-saturated bainitic ferrite is formed, followed by carbon partitioning. The time for carbon to escape is enough when the temperature is high, which makes upper bainite. As the transformation temperature is reduced, some of the carbon precipitates within the ferrite plates as cementite, leading to lower bainite. Fig. 1.18 shows effects of temperature and substitutional element on decrburising time.

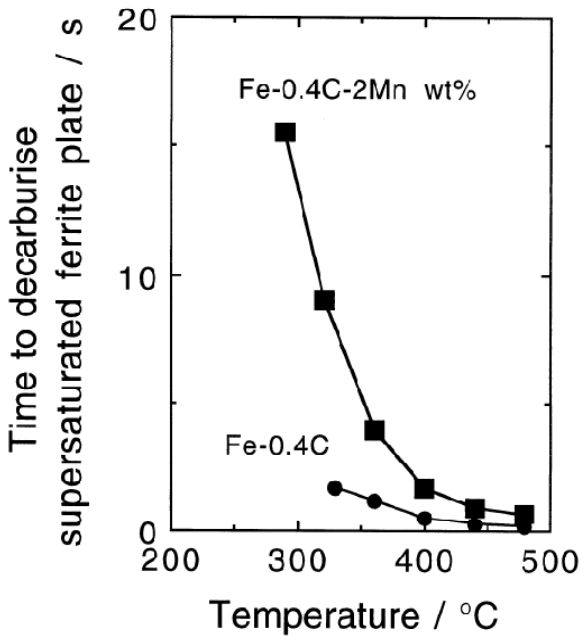

Fig. 1.18: The time to decarburise a plate of thickness 0.2 μm. Low temperature makes it slow and leads to lower bainite. Substitutional elements also retard the carbon partitioning process. Reprinted from Mujahid and Bhadeshia (1992), with kind permission from Elsevier.

Very thin bainitic plates are called subunits because they grow in clusters known as sheaves. Within each sheaf, the subunits are parallel and of identical crystallographic orientation and habit plane. The microstructure can be seen using transmission electron microscopy (TEM) because the dimensions of bainite are too small to see using optical microscopy. The overall morphology of a sheaf is illustrated in Fig. 1.19.

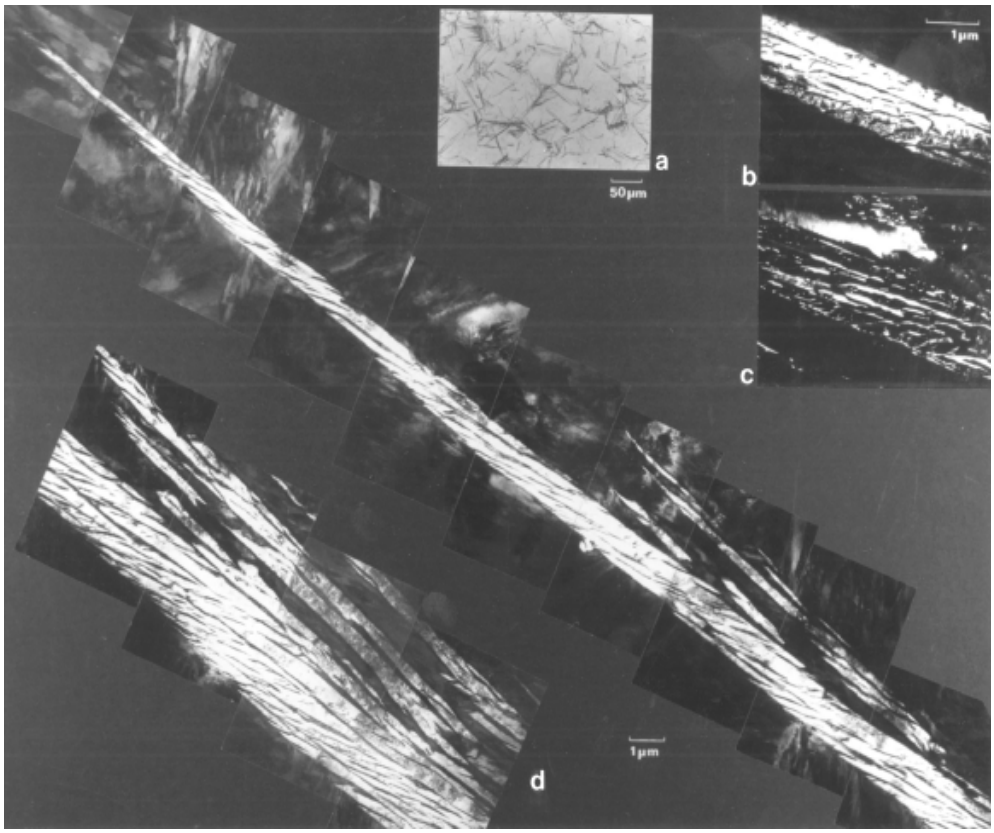

Fig. 1.19: Transmission electron micrograph of a sheaf of upper bainite in a partially transformed Fe-0.43C-2Si-3Mn wt % alloy: (a) light micrograph; (b, c) bright field and corresponding dark field image of retained austenite between the subunits; (d) montage showing the structure of the sheaf (Bhadeshia, 2001a).

1.3.2 Displacive Transformation

Martensite and bainite transformations both are displacive transformations. There is no diffusion of iron atoms and substitutional elements, atoms move in disciplined manner in order to change the structure from fcc to bcc. Many features of the bainite transformation are consistent with the phenomenological theory of martensite transformations. The difference between bainite and martensite is the nucleation behaviour and the carbon portioning process which occurs after the bainite transformation.

Bainite and austenite orientation relationship is irrational and always close to KS-NW relationship. There is an appreciable spread of orientation within a single plate because of high dislocation density. And there are small misorientations between plates within in same sheaf, but they are still close to KS-NW which are well explained by phenomenological theory of martensite.

One of the characters of the displacive transformations is invariant plane shape deformation with large shear component. Phenomenological theory predicts that the shear component of the IPS is 0.22-0.28. Shape deformation cause surface relief when it is transformed at flat surface. Fig. 1.20 shows the atomic force microscopy result. These kinds of experiments also make it possible to measure shear component of IPS. It was 0.26 in surface relief experiments (Swallow and Bhadeshia, 1996) and was 0.22 in TEM experiments (Sandvik, 1982) which are consistent with phenomenological theory. Fig. 1.20 also shows plastic deformation in adjacent austenite. Such plastic deformation causes large dislocation density in both the austenite and bainite phases. The interface of the martensite or bainite is fully coherent or semi-coherent at least, because it's the one of the requirements for the interface moving without diffusion. Interface lose coherency and cannot move any more when they meet plastically deformed region in Fig. 1.20. That's why bainite plates grow to limited size which is far less than austenite grain size. The sheaf as a whole grows by the repeated nucleation of new sub-units, mostly near the tips of those already existing.

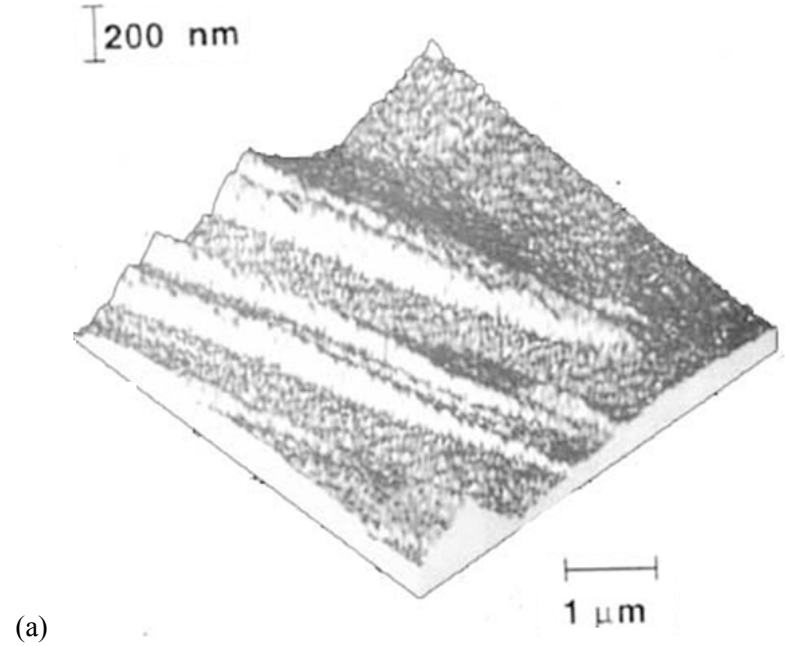

(a)

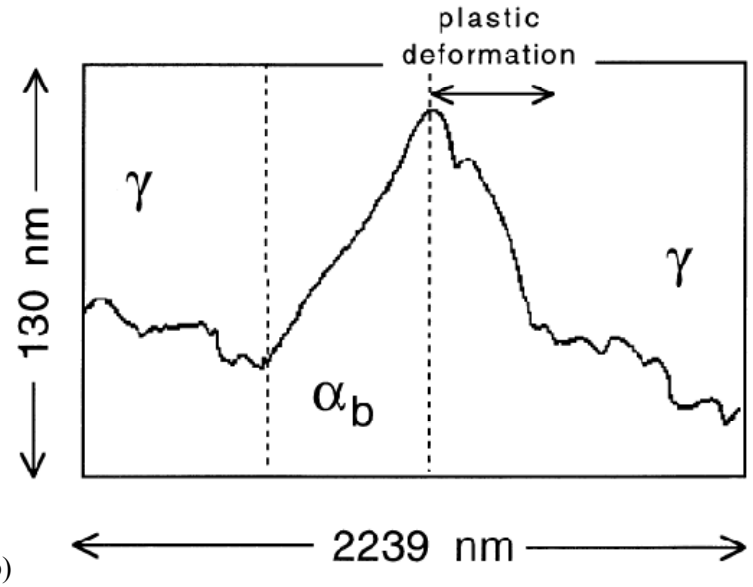

(b)

Fig. 1.20: (a) High resolution atomic force microscope plot of the displacements caused by the formation of a single sub-unit of bainite. Surface was flat before transformation. (b) Scan across the surface relief due to bainite sub-unit (Swallow and Bhadeshia, 1996).

1.3.3 Incomplete Reaction

The character of bainite which is different with martensite is the carbon partitioning process which occurs after bainite transformation. Bainite grows without carbon diffusion; it can grow far faster than expected from the theory of diffusion-controlled growth (Bhadeshia, 2001a). Another character of bainite caused by diffusionless transformation is the *incomplete reaction phenomenon*.

Fully bainitic steels are free from allotriomorphic ferrite and almost free from athermal martensite. The structure is thus composed of retained austenite, bainitic ferrite and carbides. Carbide precipitation from austenite can be suppressed by alloying with elements such as silicon and aluminium (Kozeschnik and Bhadeshia, 2008). In order to understand the mechanism of bainite transformation, it is useful to consider microstructure which does not contain carbides. As shown in Fig. 1.21, bainite growth by a diffusionless mechanism has to occur at a temperature just below T_0, when the free energy of bainitic ferrite falls below that of austenite of same composition. Ae_1 refers to the equilibrium (γ+α)/α phase boundary and Ae_3 refers to the equilbrium (γ+α)/γ phase boundary.

The stored energy in bainitic ferrite is accounted for by raising its free energy curve by an amount equal to the strain energy due to transformation, giving the T_0' curve. During isothermal transformation the excess carbon in the bainite partitions into the residual austenite, forcing the next plate to grow from carbon enriched austenite (Bhadeshia, 2001). The process finally ceases as the austenite carbon content reaches T_0' value, leading to the incomplete reaction phenomenon (Bhadeshia and Waugh, 1982). The scheme is shown in Fig. 1.22. This doesn't happen when carbides precipitate because they consume carbon and hence keep the concentration in the austenite below T_0 as transformation progresses.

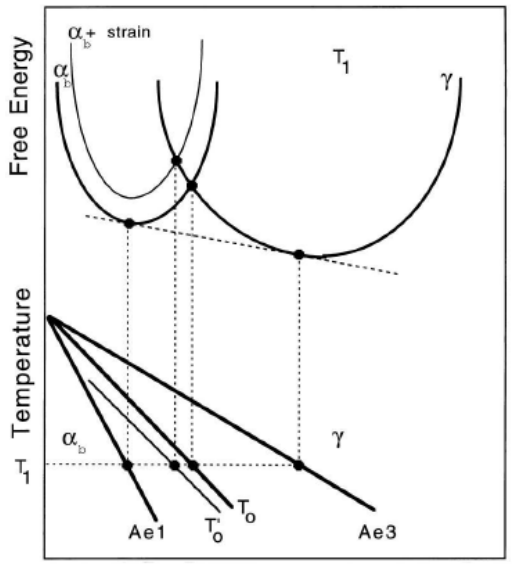

Fig. 1.21: Schematic illustration of the T_0 and $T_0^{'}$ curves. $T_0^{'}$ is same as T_0, but accounting for the stored energy of ferrite. T_1 is the temperature corresponding to the free energy curves (Bhadeshia, 2001a).

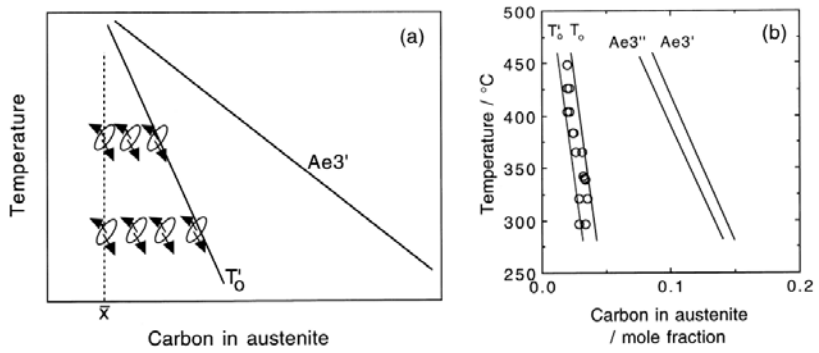

Fig. 1.22: The incomplete reaction phenomenon (Bhadeshia, 2001a). (a) A plate of bainite grows without diffusion, then partitions its excess carbon into the residual austenite. The next plate thus grows from carbon-enriched austenite. This process can only continue until $x_\gamma = x_{T_0'}$. (b) Experimental data on the incomplete reaction phenomenon. A'_{e3} refers to the equilbrium (γ+α)/γ phase boundary and A''_{e3} refers to same as A'_{e3} with accounting strain energy of α (Bhadeshia, Edmonds, 1979).

The phenomenon and fast growth rate makes it clear that carbon does not diffuse during bainitic growth. Carbon partitioning and carbide precipitation are just the next step of the transformation after the formation of supersaturated bainitic ferrite. If carbon atoms diffuse during transformation, the reaction must go on until the austenite composition reaches x_{Ae3} , as in the case for Widmanstätten transformation which can be understood through the concept of para-equilibrium.

Atom probe tomography (APT) has been used to directly confirm the phenomenon (Bhadeshia and Waugh, 1982; Peet *et al*., 2004; Caballero *et al*., 2007, 2009; Pereloma *et al*. 2007). The atom probe technique makes it possible to see atoms and their positions with atomic scale spatial and chemical resolution. One of the researches (Caballero *et al*., 2009) clearly showed the difference between Widmanstätten and bainitic ferrite using APT. It showed that Widmanstätten ferrite reaction stops when austenite reaches A'_{e3} boundary whereas bainitic reaction stops at T'_0.

There are other theories which consider the possibility of interstitial atoms' diffusion during bainite growth. Bainite and Widmanstätten transformations are treated as same diffusional transformations in a theory (Hillert, 2002; Hillert *et al*., 2004; Borgenstam *et al*., 2009). There is another model involving a partial supersaturation of carbon (Olson *et al*., 1989, 1990; Mujahid and Bhadeshia, 2001). The model implies the possibility of gradual transition from bainite to martensite. Constrained paraequilibirum condition also has a potential for describing carbon behaviour during bainite transformation (Speer *et al.*, 2003).

1.3.4 Low-Temperature Bainite

Bainitic sub-units grow up to a limited size, and are thin as mentioned earlier. The reason is that adjacent austenite phase cannot accommodate the shape deformation elastically. There is considerable plastic relaxation in the austenite adjacent to the bainite plates (Fig. 1.20). The dislocation debris generated in this process resists the advance of the bainite/austenite interface, the resistance being

greatest for strong austenite. Neural network analysis revealed that the strength of austenite is the most important factor which determines the thickness of bainite (Singh and Bhadeshia, 1998). Because of that, the plates become thicker at high transformation temperatures since the yield strength of the austenite will then be lower. There are also other factors such as driving force and the transformation temperature itself (Singh and Bhadeshia, 1998). A large driving force increases the nucleation rates. As a result, a larger driving force also leads to a finer microstructure. Though austenite strength is the most important factor that determines the thickness of the bainite, austenite strength and free energy change during transformation are both influenced by temperature. A lower transformation temperature makes austenite strong and the driving force large. This leads to thinner plates of bainite. It is necessary to transform at low temperatures in order to get extremely fine bainite.

There are two equations which account relationship between strength and grain size. One is the Hall-Petch equation and the other is due to Langford and Cohen. When the slip distance is less than about 1 μm, the Langford and Cohen relationship is more reasonable (Langford and Cohen, 1970). For a given thickness *t*, the mean lineal intercept, $\bar{L}$ is roughly two times the thickness and the strength contribution $\Delta\sigma$ due to the size of the plate is given by

$$\Delta\sigma = 115(\bar{L})^{-1} \text{ MPa} \qquad (1.31)$$

where $\bar{L}$ is in micrometers according to Langford and Cohen relationship. The inverse dependence on $\bar{L}$ is because the transmission of slip across boundaries is determined by the energy required to expand dislocation loops rather than by the pile-up of the dislocations obstructed by boundaries. It follows that $\Delta\sigma$ =311 MPa for plates of thickness 185 nm, whereas $\Delta\sigma$=1642 MPa for plates of thickness 35 nm, which means it's possible to get additional strength of more than 1 GPa without compromising toughness.

Extremely fine bainitic structures which consist of ferrite plates and carbon-enriched austenite without carbide precipitation have been developed (Caballero *et*

al., 2002, 2005; Garcia *et al*., 2003a, 2003b, 2003c). This was achieved through transformation at temperatures as low as 200-125 ℃. The scale of the structure achieved is fine indeed, amounting to tens of nanometers as shown in Fig. 1.23.

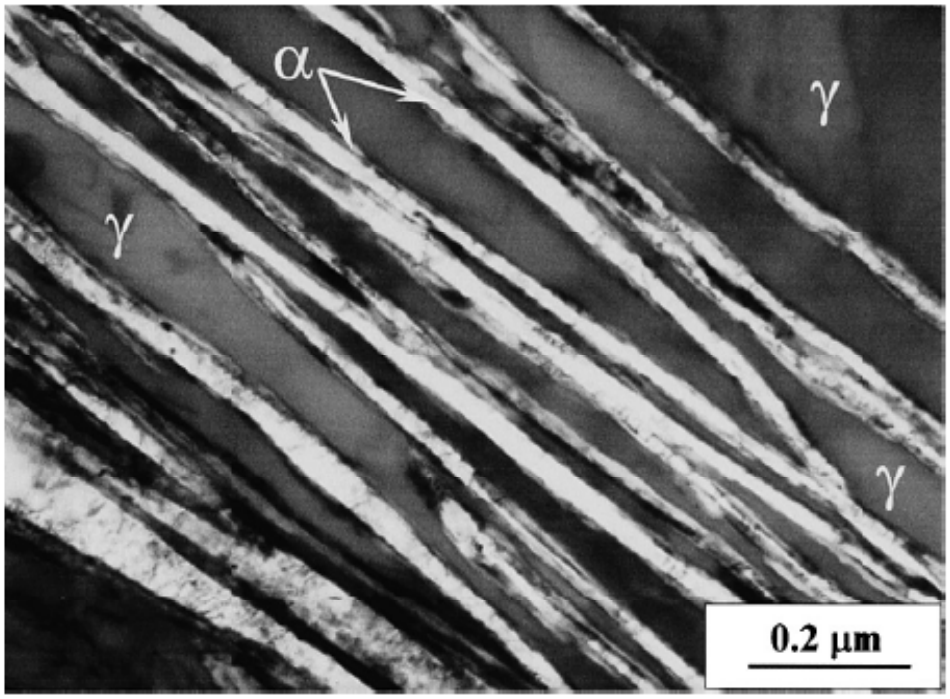

Fig. 1.23: Fe-0.98C-1.46Si-1.89Mn-0.26Mo-1.26Cr-0.09V wt %, Very fine structure: mixture of bainitic ferrite and retained austenite achieved through transformation at 200 ℃ for 5 days. Originally published in *ISIJ International* (Garcia *et al*., 2003c).

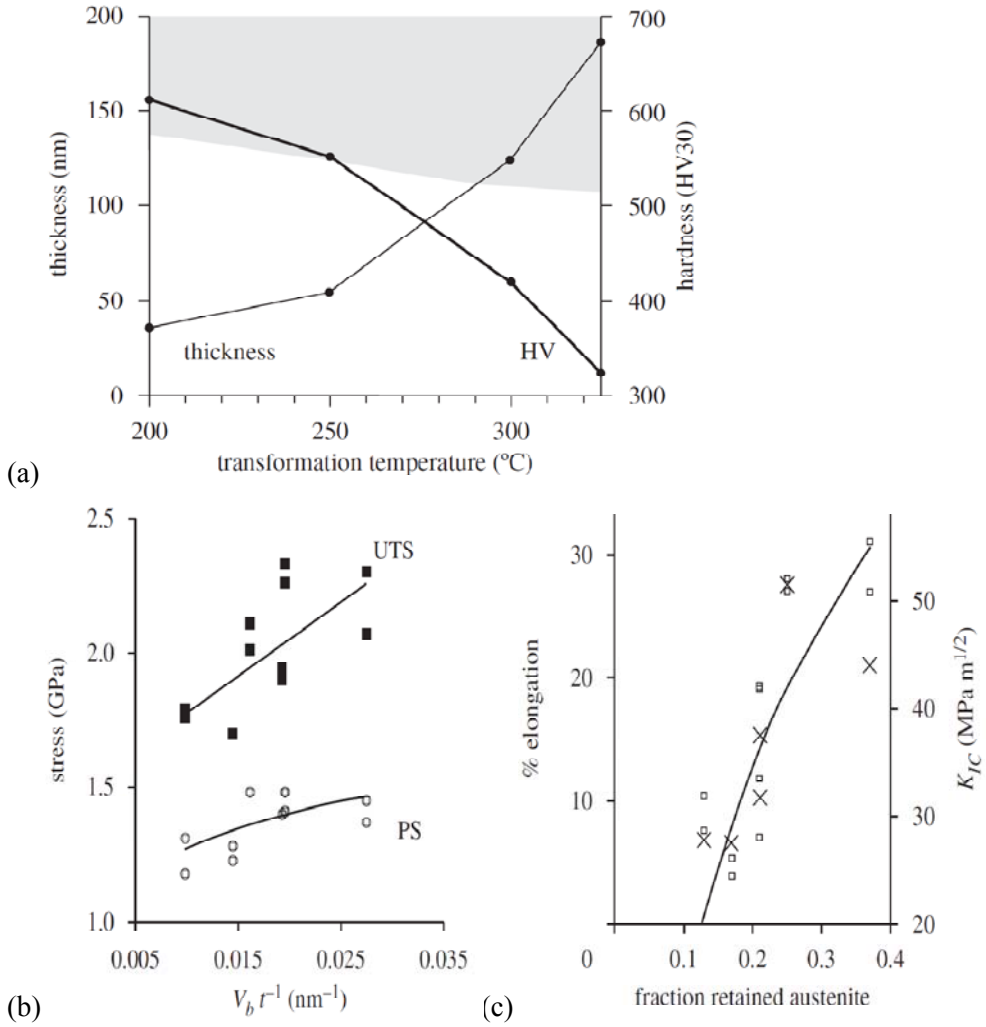

Fig. 1.24: Some mechanical properties of low-temperature bainitic steels. (a) The axis on the left is the stereologically corrected thickness of the bainitic ferrite plates. The shaded region represents the fraction of austenite as a function of temperature, given by the fraction of the height of the diagram, the rest of the microstructure being bainitic ferrite (b) The ultimate tensile strength (UTS) and 0.2 % proof strength (PS) as a function of the volume fraction of bainitic ferrite divided by the ferrite platelet thickness. (c) Ductility (points and curve) and toughness K_{IC} represented as crosses (Caballero *et al.*, 2002; Garcia-Mateo and Caballero, 2005).

The structure exhibits an excellent combination of strength and ductility. Some strength, ductility, toughness and hardness data are illustrated in Fig. 1.24. It is shown the inverse dependence of hardness on plate thickness in Fig. 1.24(a,b). The strength comes mainly from the fine scale of the structure rather than carbon even though the steels contain about 1 wt % of carbon. One interesting observation on mechanical properties is the role of retained austenite on ductility. Ductility is related to the amount of retained austenite as shown in Fig. 1.24(c). It has been suggested that failure occurs when the austenite, which is the toughest of all the phases present, becomes geometrically isolated, i. e. it loses percolation (Bhadeshia, 2008a). Garboczi *et al.* (1995) have modelled the percolation threshold for ellipsoidal objects placed in a matrix. Assuming that the austenite is subdivided into the form of plates by the bainite, it can be represented by oblate ellipsoids with an aspect ratio r of between 1/10 and 1/100. The percolation threshold is then found to be $p_c \approx 1.27r$, i.e. $0.127 \geq p_c \geq 0.0127$. This is consistent with the observation that tensile failure occurs when $V_\gamma \approx 0.1$. Fig. 1.25 indicates that substantial quantities of brittle martensite which forms during deformation can exist in the microstructure before failure occurs. This is because the tendency of the martensite to crack under stress depends on its absolute size, with coarse regions being most susceptible (Chatterjee and Bhadeshia 2006). It is the fine scale of the retained austenite that permits the martensite that forms during deformation to be tolerated without compromising the ductility until the percolation threshold is reached.

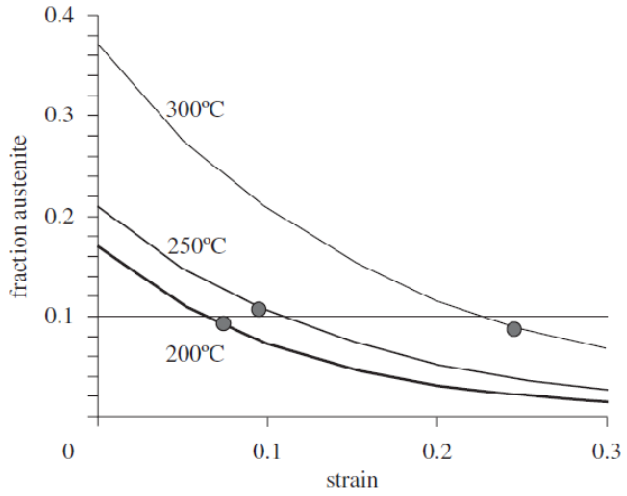

Fig. 1.25: Calculated variation in the fraction of austenite as a function of plastic strain in three nanostructured bainitic samples containing different initial quantities of retained austenite. The isothermal transformation temperatures used to generate the initial structures are annotated (Bhadeshia, 2009).

The applications, advantages, mechanical properties, characteristics and design strategies of these extremely fine carbide free bainitic structures have been described elsewhere (Bhadeshia, 1998; 2004; 2005a; 2005b; 2006; 2007; 2009). Ultimate tensile strengths of 2500 MPa in tension have been obtained routinely, ductilities in the range 5-30 % and toughness in excess of 30-40 MPa $m^{1/2}$. The bainite is also the hardest ever achieved, 700 HV. These mechanical properties come mainly from the fine microstructure and tough austenite films. The potential advantages of the mixed microstructure of fine bainitic ferrite and austenite films can be listed as follows (Bhadeshia 1998):

(a) Cementite is responsible for initiating fracture in high–strength steels. Its absence is expected to make the microstructure more resistant to cleavage failure and void formation.

(b) The bainitic ferrite is almost free of carbon, which is known to embrittle ferritic microstructures.

(c) The microstructure derives its strength from the ultrafine grain size of the ferrite plates, which are less than 1 μm in thickness. It is the thickness of these plates which determines the mean free slip distance, so that the effective grain size is less than a micrometre. This cannot be achieved by any other commercially viable process. Grain refinement is the only method available for simultaneously improving the strength and toughness of steels.

(d) The ductile films of austenite which are intimately dispersed between the plates of ferrite have a crack blunting effect. They further add to toughness by increasing the work of fracture as the austenite is induced to transform to martensite under the influence of the stress field of a propagating crack. This is the TRIP, or transformation–induced plasticity effect.

(e) The diffusion of hydrogen in austenite is slower than in ferrite. The presence of austenite can therefore improve the stress corrosion resistance of the microstructure.

(f) Steels with the bainitic ferrite and austenite microstructure can be obtained without the use of any expensive alloying additions. All that is required is that the silicon concentration should be large enough to suppress cementite.

The most useful advantage of the steel is that the simple process route avoids rapid cooling so that residual stresses are avoided, even in large pieces. There are many adjectives that have been given to the bainitic microstructure described above: cold bainite, hard bainite, strong bainite, super bainite and low-temperature bainite (Bhadeshia, 2004).

1.3.5 Low-Carbon, Low-Temperature Bainite

Super-bainite is based on high-carbon steel, about 1 wt %. Such steels should be difficult to weld because of the possibility of untempered, brittle martensite in the coarse-grained heat affected zones of the joints. Such martensite fractures easily, leading to a gross deterioration in the structural integrity of the joint. For this reason,

the vast majority of weldable steels have low-carbon concentrations. It would be desirable therefore to make the low-temperature bainite with a much reduced carbon concentration (Bhadeshia, 2006a). One criterion which should be satisfied in order to get low-temperature bainite is that martensite-start temperature should be low and bainite-start temperature (B_S) should be higher than M_S.

A theory which assesses the possibility of low-carbon low-temperature bainite is available. The theory only relies on thermodynamics to predict the M_S and B_S. We can consider several kinds driving force when austenite transforms (Fig. 1.26). $\Delta G^{\gamma\rightarrow\gamma'+\alpha}$ is the free energy change when austenite of composition $\bar{x}$ decomposes into the equilibrium mixture of ferrite and carbon-enriched austenite (γ'), Fig. 1.26a. And the free energy change per mole of ferrite is ΔG_2

$$\Delta G_2 = \Delta G^{\gamma\rightarrow\gamma'+\alpha} \times \frac{x^{\gamma\alpha} - x^{\alpha\gamma}}{x^{\gamma\alpha} - \bar{x}} \tag{1.32}$$

where $x^{\alpha\gamma}$ and $x^{\gamma\alpha}$ are the equilibrium compositions of ferrite and austenite respectively. The calculation of the free energy change associated with nucleation must take into that only a minute quantity of ferrite is formed. Consider the change ΔG_2 as austenite decomposes to a mixture of ferrite and enriched austenite of composition $x^{\gamma} = x^{\gamma\alpha}$. As the fraction of ferrite is reduced, x^{γ} and $\bar{x}$ move towards each other causing the line AB to tilt upwards. In the limit that $x^{\gamma} = \bar{x}$, AB becomes tangential to the curve at $\bar{x}$. The free energy change for the formation of a mole of ferrite nuclei of composition x^{α} is then given by ΔG_3, Fig. 1.26b. The greatest reduction in free energy during nucleation is obtained if the composition of the ferrite nucleus is set to a value x_m , given by a tangent to the ferrite free energy curve which is parallel to the tangent to the austenite free energy curve at $\bar{x}$, as shown in Fig. 1.26b. This maximum possible free energy change for nucleation is designated ΔG_m. There is simplification when the transformation occurs without composition change. The change $\Delta G^{\gamma\rightarrow\alpha}$ is the vertical distance between the austenite and ferrite energy curves at the composition of interest (Fig. 1.26c).

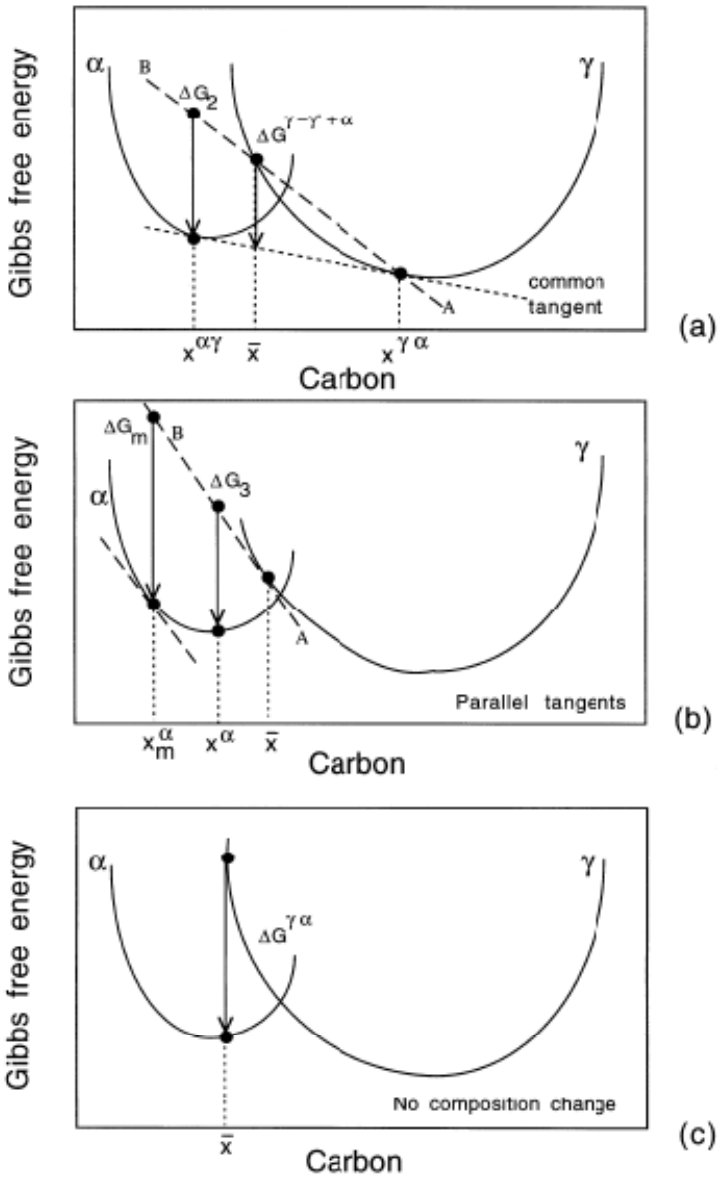

Fig. 1.26: Free energy diagrams illustrating the chemical free energy change during the nucleation and growth of ferrite from austenite of composition $\bar{x}$. The term γ' refers to austenite which is enriched in carbon as a result of the decomposition of austenite of composition $\bar{x}$ into a mixture of ferrite and austenite (Bhadeshia, 2001a).

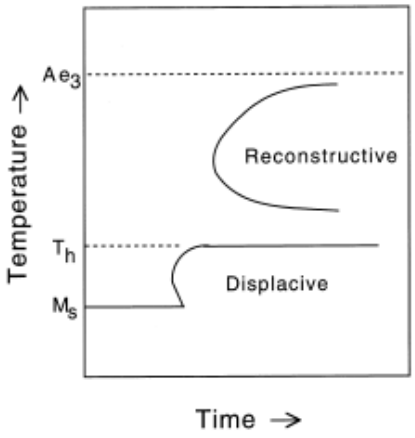

Fig. 1.27: Schematic TTT diagram illustrating the two C-curves and the T_h temperature (Bhadeshia, 2001a).

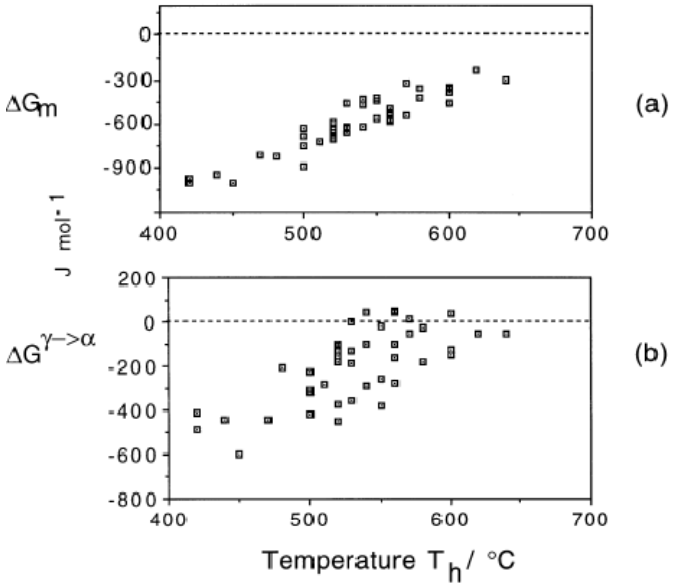

Fig. 1.28: The free energy change necessary in order to obtain a detectable degree of transformation. Each point represents different steel and there is no distribution made between Widmanstätten ferrite or bainite. (a) Calculated assuming the partitioning of carbon during nucleation. (b) Calculated assuming that there is no change in composition during nucleation. Reprinted from Bhadeshia (1981c) with kind permission from Elsevier.

Time temperature transformation (TTT) diagrams consist essentially of two C-curves. The lower C-curve has a characteristic flat top at a temperature T_h, which is the highest temperature at which ferrite can form by displacive transformation (Fig. 1.27). The transformation product at T_h may be Widmanstätten ferrite or bainite.

The analysis of driving forces at T_h gives information about nucleus of Widmanstätten ferrite and bainite. Analysis shown in Fig. 1.28 proves that carbon must partition during the nucleation stage in order always to obtain a reduction in free energy. The situation illustrated in Fig. 1.28b is not viable since diffusionless nucleation would in some cases lead to an increase in the free energy (Bhadeshia, 1981c). The data in Fig. 1.28(a) shows good linearity, the equation fitted to the data is (Ali and Bhadeshia, 1990)

$$G_N = C_1(T - 273.18) - C_2 \text{ J mol}^{-1} \quad (1.33)$$

where C_1 and C_2 are fitting constant. G_N is to be regarded as a *universal nucleation function*, because it defines the minimum driving force necessary to achieve a perceptible nucleation rate for Widmanstätten ferrite or bainite in any steel.

The nuclei of Widmanstätten ferrite and bainite are identical, but the thermodynamic condition determines whether the nucleus evolves into bainite or Widmanstätten ferrite. If diffusionless growth cannot be sustained at T_h then the nucleus develops into Widmanstätten ferrite so that T_h is identified with Widmanstätten ferrite start temperature (W_S). A larger undercooling is necessary before bainite can be stimulated. If, however, the driving force at T_h is sufficient to account for diffusionless growth, then T_h=B_S and Widmanstätten ferrite does not form at all. The thermodynamic conditions for three displacive transformations can be summarised as Table 1.3.

Table 1.3: Summary of displacive transformations.

	Nucleation (Mechanism, driving force)	Growth (Mechanism, driving force)
Widmanstätten α	Para-equilibrium, ΔG_m	Para-equilibrium, $\Delta G^{\gamma\rightarrow\gamma'+\alpha}$
Bainite	Para-equilibrium, ΔG_m	Diffusionless, $\Delta G^{\gamma\rightarrow\alpha}$
Martensite	Diffusionless, $\Delta G^{\gamma\rightarrow\alpha}$	Diffusionless, $\Delta G^{\gamma\rightarrow\alpha}$

As shown in Table 1.3, carbon diffusion in bainite nucleation stage is one of the distinguishing features of bainite when compared with martensite. That's why carbon is effective to maintain the difference between M_S and B_S and high-carbon alloys were used for low-temperature bainite. The above knowledge can be applied to predict transformation temperatures. Widmanstätten ferrite forms below the A_{e3} temperature when:

$$\begin{aligned} \Delta G^{\gamma\rightarrow\gamma'+\alpha} &< -G_{SW} \\ \Delta G_m &< G_N \end{aligned} \tag{1.34}$$

where G_{SW} is the stored energy of Widmanstätten ferrite (about 50 J mol^{-1}). The first of these conditions ensures that the chemical free energy change exceeds the stored energy of the Widmanstätten ferrite, and the second that there is a detectable nucleation rate. Bainite is expected below the T_0' temperature when

$$\begin{aligned} \Delta G^{\gamma\rightarrow\alpha} &< -G_{SB} \\ \Delta G_m &< G_N \end{aligned} \tag{1.35}$$

where G_{SB} is the stored energy of bainite (about 400 J mol^{-1}). Martensite formation condition has been discussed earlier in the paper (eq. 1.18).

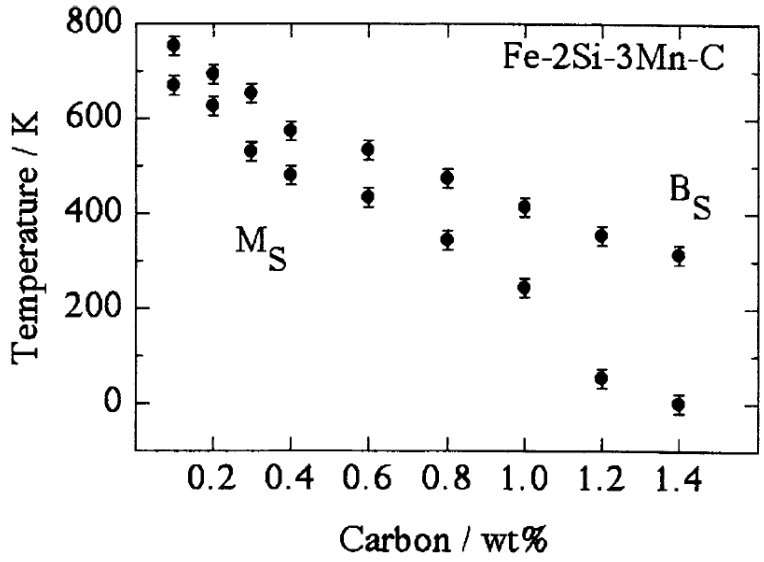

Fig. 1.29: Calculated transformation temperatures as a function of the carbon concentration. Originally published in *ISIJ International* (Garcia *et al*., 2003c).

High-carbon alloys were used to develop low-temperature bainite about 1 wt %. There is no lower limit to the bainite-start temperature, but it should be higher than M_S. The theory calculates the carbon effect on transformation temperatures. Carbon is particularly effective in depressing M_S and increasing the gap between M_S and B_S as shown in Fig. 1.29.

Another strategy for depressing transformation temperatures is substitutional alloying. Fig. 1.30 shows the calculated effect on nickel. The calculation predicted that the fully bainitic microstructure is impossible to obtain because of the merging of the M_S and B_S temperatures at large substitutional solute concentration

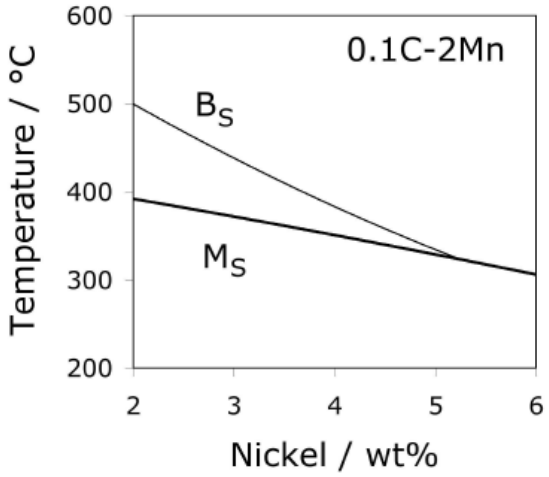

Fig. 1.30: Calculated bainite and martensite-start temperatures (Yang and Bhadeshia, 2008).

Yang and Bhadeshia (2008) applied this strategy and showed that merge of M_S and B_S doesn't happen when transformation time is long enough. Both transformation temperatures were depressed as nickel same as predicted in the theory. However it was possible to get bainitic structure by transforming the highest nickel alloy for 3 months (Fig. 1.31). The research showed that the difficulties due to merging of M_S and B_S might be solved allowing long heat treatment. The study also revealed the presence of coalesced bainite in low carbon low temperature bainite. Coalesced bainite begins as a series of adjacent, identically oriented platelets of ferrite only marginally separated by films of austenite. As the platelets lengthen, they accelerate and coalesce. The carbon is then trapped in the ferrite, either to precipitate later or to partly partition into the residual austenite at the peripheries of the cluster of platelets. Such coalescence can only occur when the driving force available is sufficient to sustain the greater strain energy associated with the coarser plates. These coalesced bainite eliminates the advantage of a fine

microstructure and is detrimental to mechanical properties. Therefore it should be avoided in alloy and process design.

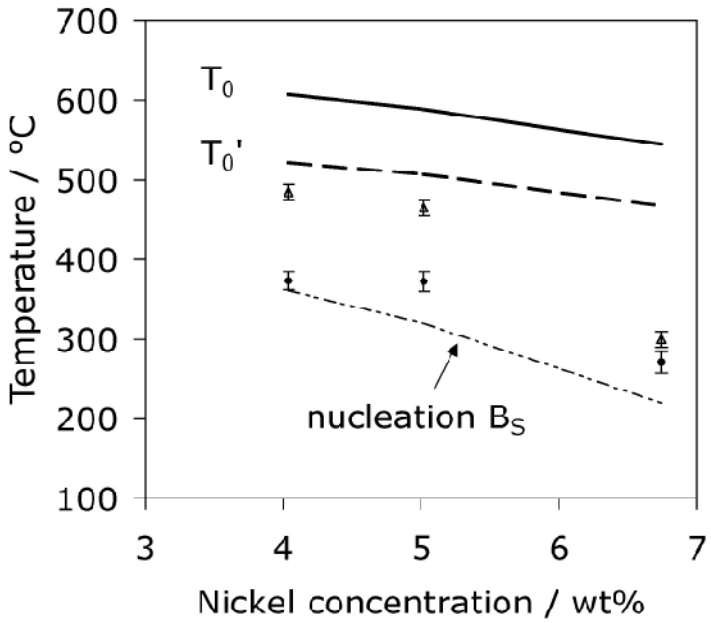

Fig. 1.31: Fe-0.1C-2Mn-Ni wt % alloys. Calculated T_0 and T_0' curves and measured martensite–start (circles) and bainite–start temperatures (triangles). The calculated nucleation–limited B_S is also illustrated (Yang and Bhadeshia, 2008).

1.4 Summary

The characteristics and theory of martensite have been reviewed. Martensitic transformation is a diffusionless displacive transformation, and is understood by a combination of phenomenological crystallography and nucleation theory. It is possible therefore, to explain the many features of martensitic transformation. The start-temperature, M_S, is an important parameter in the design of low-temperature bainitic steels. The available methods for predicting M_S have been reviewed. M_S can be calculated as a temperature where the driving force for diffusionless transformation achieves a critical value consistent with the nucleation mechanism. This critical driving force is in general a function of alloying elements. The accurate

and reasonable measurement of M_S is also as important as the metallurgy for prediction. An offset method developed recently is quantitative analysis which leads to an objective and reproducible estimation of M_S measuring using dilatometer, together with a statement of uncertainty.

Bainite transformation is also a displacive transformation which is associated with an invariant-plane strain and has similar crystallographic features with martensite. There is no diffusion during bainitic growth even for interstitial atoms. For example, fast interface velocity and the incomplete reaction phenomenon provide evidence for this mechanism. Two features of bainite are different when compared with martensite. Bainite nucleation requires carbon diffusion in order to be possible from a thermodynamic point of view. Growth is not accompanied by carbon partitioning, but it is redistributed into the residual austenite immediately after the formation of a bainite crystal.

The structure of very fine bainitic ferrite with carbon enriched austenite films has been developed based on bainite transformation theory. And the presence of austenite films results in a good combination of strength and toughness. Rapid cooling is not necessary for such steels which enable the manufacture of large pieces of steel. However, the steel used containing a high carbon concentration, so it is not suitable for welding. There was trial to develop low-carbon, low-temperature bainite using high substitutional solute concentration and it revealed the some problems. Therefore this study aims deep investigation of the possibility of low-carbon, low-temperature bainite.

Chapter 2: M_S and Austenite Grain Size

2.1 Introduction

The lowest temperature where bainite can be obtained by isothermal transformation is limited by martensite-start temperature. The original work on low-temperature bainite used 1 wt % carbon (Caballero *et al*., 2002, 2005; Garcia *et al*., 2003a, 2003b, 2003c) to depress transformation temperatures and Yang and Bhadeshia (2008) used nickel addition to depress it. However, the chemical composition is not the only variable that affects M_S. Several studies on the dependence of the M_S on the austenite grain size have been reported (Ansell *et al.*, 1979; Brofman and Ansell, 1983; Lee and Lee, 2005; Huang and Xu, 2006). The austenitisation temperature also affects M_S (Ankara *et al*., 1966; Maki *et al*., 1971) but only via the associated variation in austenite grain size (Umemoto and Owen, 1974). In another context, the stability of retained austenite to martensitic transformation increases as the former is refined in a mixed microstructure (Leslie and Miller, 1964; Rao and Rashid, 1983; Caballero *et al.*, 2008).

Many qualitative explanations of such observations have been suggested. One argument is that a refinement of the austenite grain size leads to Hall–Petch strengthening of austenite, thereby making it difficult for martensite to form (Brofman and Ansell, 1983). It is known that solid-solution strengthening affects the nucleation of martensite and bainite by providing a greater resistance to the motion of dislocations involved in the nucleation process as described in the previous chapter. On the other hand, the Hall–Petch theory relies on the transmission of slip across grain boundaries, whereas any resistance to the motion of dislocations at the nucleation stage has to be more localized. Indeed, the equations for the activation volume in the thermally activated motion of the martensite/austenite interface relate only to the volume of material swept by the interface between the parent and nucleus (Olson *et al*., 1989; 1900).

An alternative explanation in the case of highly alloyed steels is based on a burst phenomenon in which a large fraction of the austenite transforms into martensite within a very small temperature interval. The tendency for a burst to occur decreases as the austenite grain size is refined (Guimarães and Gomes, 1978). This is explained qualitatively by the fact that the stress concentration at a martensite plate-tip scales with the size of the plate, which in turn is related to the austenite grain size. Transformation is therefore detected at a higher temperature for large grains (Bokros and Parker, 1963). However, most martensitic steels do not undergo bursts of transformation—especially those that have a low alloy content and form lath-like martensite. There is a gradual increase in the fraction of martensite as a function of undercooling below the M_S temperature, roughly following the classical theory (Koistinen and Marburger, 1959).

It is possible to use the fact that M_S decreases as austenite grain size decreases in developing low-temperature bainite. Austenitisation at low temperature would result in an additional depression of M_S. However, the reason for these observations is not clear. The aim of the work presented in this chapter is to develop a theory which explains why M_S decreases as austenite grain size decreases.

2.2 Experimental

The alloy used was prepared as a solid cylindrical sample of dimensions 3.6×8 cm by centrifugal casting and then homogenised in a vacuum furnace for 2 days at 1200 ℃. The sample was then cut along its length into six pieces of equal thickness; their individual chemical analyses are shown in Table 2.1. Composition variations of the kind depicted can only influence M_S by ±1 ℃ (Yang and Bhadeshia, 2007).

Details of the experimental method for measuring the transformation temperature using a push-rod BAHR DIL805 high-speed dilatometer are as follows. Each sample was austenitised at 770–1100 ℃ for 30 s, but one sample was austenitised at 1100 ℃ for 600 s to obtain the largest austenite grains. The heating rate used was 30 ℃ s^{-1}, giving A_{c1} and A_{c3} temperatures of 660 and 754 ℃, respectively. The

heating and austenitisation treatments were carried out under a vacuum of 5×10^{-4} mbar. Every sample was quenched twice before measuring M_S to avoid any effect of initial microstructure. The reported measurements of M_S are from the second quench.

M_S temperatures were measured by the offset method described in the previous chapter. The method measures the temperature where 1 vol. % martensite forms. It is impossible to detect the first single martensitic lath formation and M_S is normally measured as the temperature where a detectable minimum amount of martensite forms. That is why M_S is dependent on the sensitivity of equipment. The offset method makes it avoid such ambiguity.

Saturated aqueous picric acid with wetting agent (100 ml of saturated picric acid with 4 g of sodium dodecylbenzene sulfate in 100 ml H_2O) was used to reveal the prior austenite grain structure. The grain size was measured using the mean linear intercept method (Dehoff and Rhines, 1968).

Table 2.1: Chemical composition of samples in wt %

Sample	C	Ni	Mn
1	0.124	5.02	2.26
2	0.126	5.03	2.28
3	0.126	5.01	2.26
4	0.126	5.05	2.28
5	0.123	4.97	2.24
6	0.127	5.04	2.28
Average	0.125	5.02	2.27

2.3 Results and Discussion

Prior austenite grain size increased with the austenitisation temperature as shown Fig. 2.1a. Example micrographs are shown in Fig. 2.2. The largest grain is more than 20 times the size of the smallest. A typical dilatometric curve is shown in Fig. 2.1b, it confirms that the transformation to martensite occurs gradually with undercooling; the data presented are for the largest austenite grain size, which is known to be prone to bursts of transformation in highly alloyed steels. The measured M_S temperature according to austenite grain size confirmed that it is depressed due to grain refinement (Fig. 2.3).

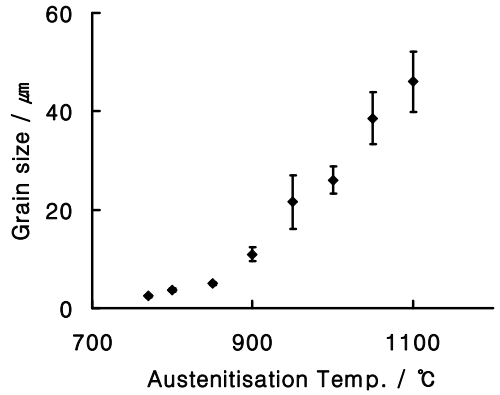

(a)

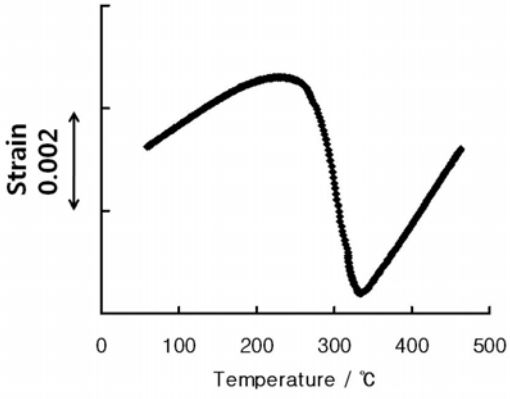

(b)

Fig. 2.1: (a) Prior austenite grain size variation as a function of austenitisation temperature. (b) Typical dilatometric curve which shows that martensitic transformation of the alloy is athermal rather than with a burst character.

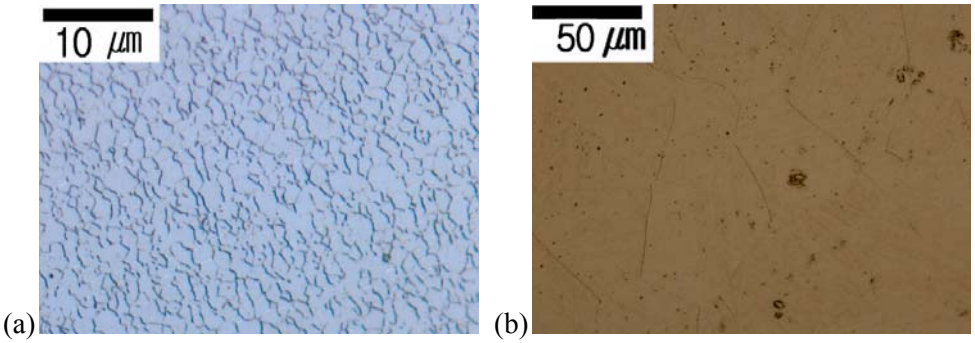

Fig. 2.2: Prior austenite grain boundaries are revealed in quenched samples. (a) Sample austenitised at 770 ℃ for 30 s and (b) 1050 ℃ for 30 s. Note that the magnifications are different.

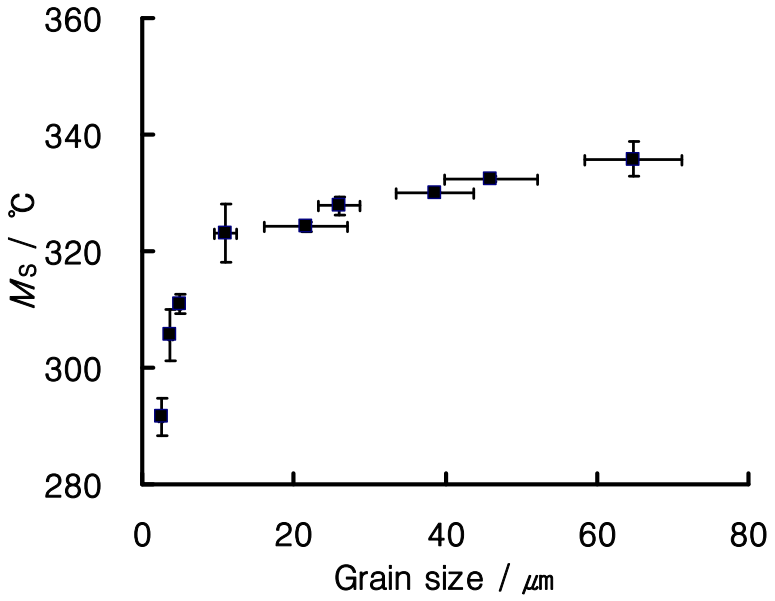

Fig. 2.3: M_S as a function of prior austenite grain size. M_S is depressed due to grain refinement.

2.3.1 Fisher's analysis

The model which explains Fig. 2.3 starts from Fisher's analysis (1949), which describes geometric partitioning as transformation proceeds. A martensite interface cannot move across grain boundary or other martensite plate. Therefore, each plate divides the grain into smaller compartments, so that subsequent plates are reduced in size as transformation proceeds (Fig. 2.4).

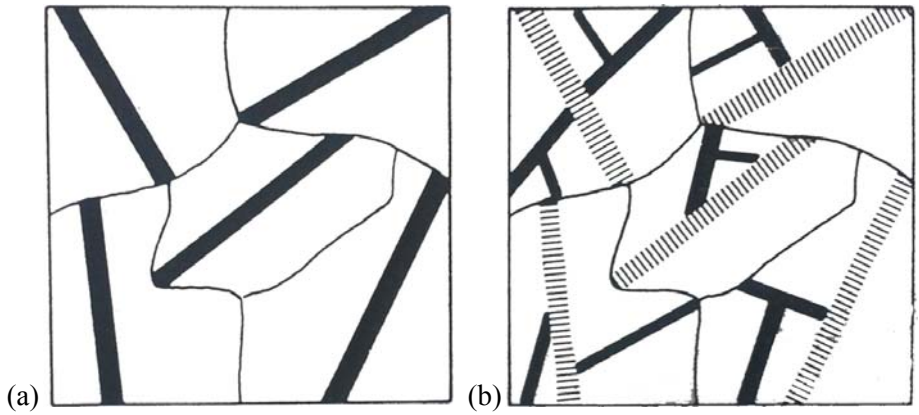

Fig. 2.4: Illustrations which show successive stages of the transformation. (a) Plates formed at early stages (b) plates formed at later stages are smaller shown as solid black (McMurtrie and Magee, 1970).

It is assumed that the fraction increase per plate ($df/\,dN_v$) is a constant fraction of compartment within which it forms:

$$\frac{df}{dN_v} = m(1-f)\overline{V_c} \tag{2.1}$$

where $\overline{V_c}$ is the average size of the compartment resulting from the partitioning of an austenite grain by the presence of martensite plates and *f* is martensite fraction. Aspect ratio (m) was assumed in this research to be 0.05 (Christian, 1979). The compartment size is reciprocal of the number of compartments per unit volume (N_v^c):

$$\frac{df}{dN_v} = m(1-f)\frac{1}{N_v^c} \tag{2.2}$$

Initial number of compartments per unit volume is equal to the reciprocal of the austenite grain volume. And newly formed martensite plates divide a compartment into two, therefore each plate produce one new compartment. It can be expressed as

$$N_v^c = \frac{1}{V_\gamma} + N_v \tag{2.3}$$

where V_γ is the average austenite grain volume. On combining eqs. (2.2) and (2.3) we obtain:

$$N_v = \frac{1}{V_\gamma}\left[\exp\left\{-\frac{\ln(1-f)}{m}\right\} - 1\right] \tag{2.4}$$

2.3.2 M_S and Austenite Grain Size

Dilatometric data such as those in Fig. 2.3a can be converted into martensite fraction data (Fig. 2.5), which in turn yield N_v using eq. 2.4. The numbers of plates per unit volume are presented in Fig. 2.6.

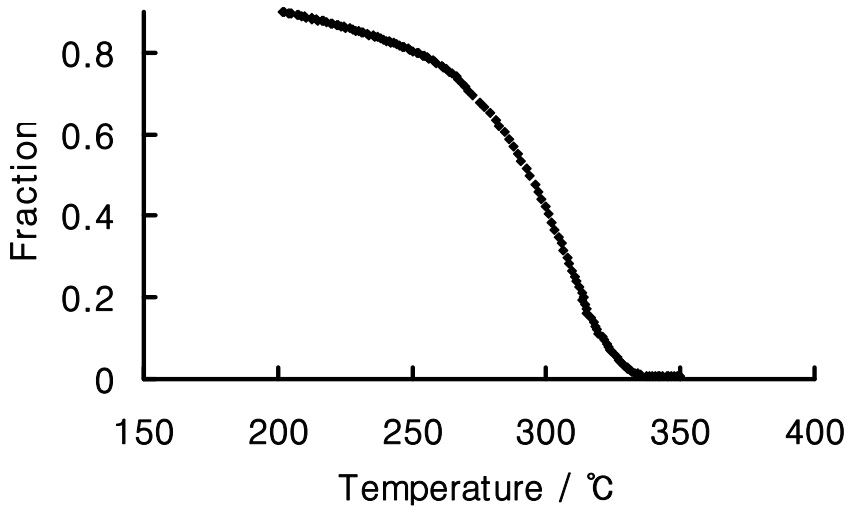

Fig. 2.5: Evolution of martensite according to temperature, sample austenitised at 1100 ℃ for 30 s.

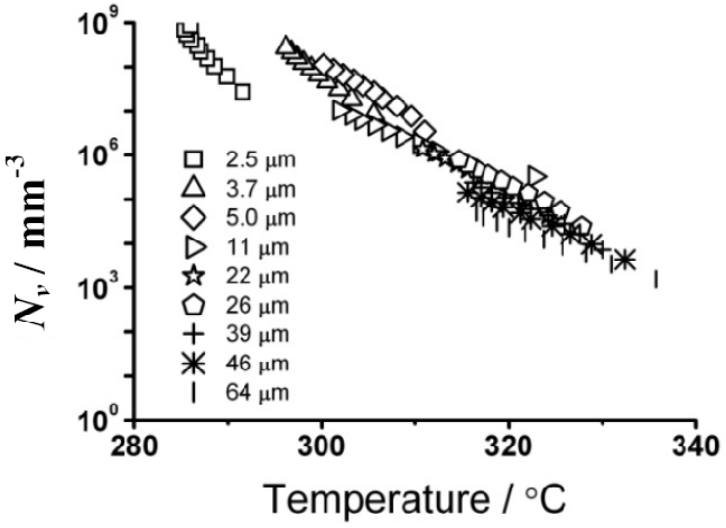

Fig. 2.6: Calculated number of plates per unit volume as a function of the temperature in the early stage of the transformations. The number of activated nuclei is independent of grain size.

The trends illustrated in Fig. 2.6 seem independent of the prior austenite grain size and can be represented reasonably by an equation of the form:

$$N_v = \exp\{b(M_s^0 - T)\} - 1 \tag{2.5}$$

where b is an empirical fitting constant. The term M_s^0 is defined as a fundamental martensite start temperature for a large austenite grain size, large as unit volume. On combining eqs. (2.4) and (2.5) one obtains:

$$M_s^0 - T = \frac{1}{b}\ln\left[\frac{1}{V_\gamma}\left\{\exp\left(-\frac{\ln(1-f)}{m}\right) - 1\right\} + 1\right] \tag{2.6}$$

In this equation, the term $M_s^0 - T$ becomes $M_s^0 - M_S$ when the fraction f is set to the first detectable fraction (e.g. 0.01 in offset method). The equation explains why M_S increases with the grain size, with $M_S \rightarrow M_s^0$ as $V_\gamma \rightarrow \infty$. The temperature M_s^0 where the first martensite plate forms are in this hypothesis the same regardless of grain size. However, a large grain sample can reach a detectable fraction at relatively high temperatures. Eq. 2.6 is compared with experimental results in Fig. 2.7. Lines in Fig. 2.7 are produced with f=0.01 (the offset used in determining

the martensite start temperature); aspect ratio m=0.05; two fitting constants are used: b=0.2689 ℃$^{-1}$ and M_S^0=364 ℃.

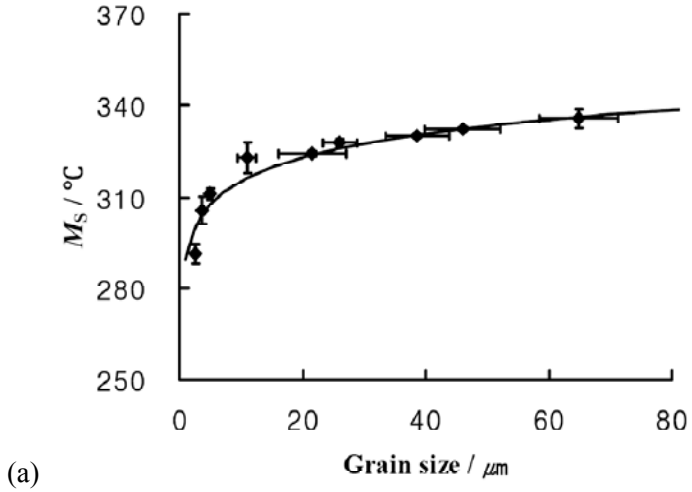

(a)

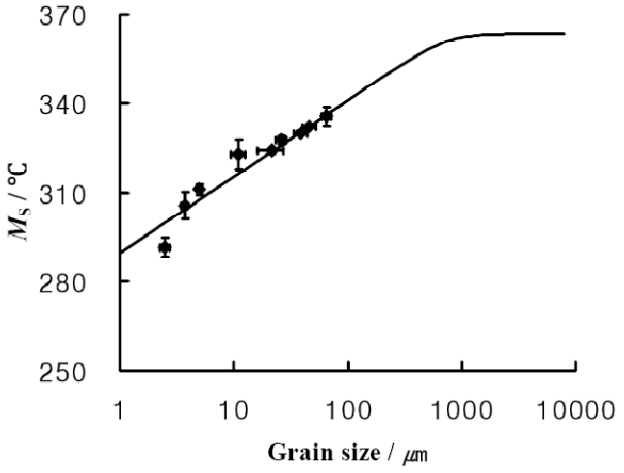

(b)

Fig. 2.7: Experimental data with calculation by eq. 2.6. Figures (a) and (b) are same but scales are different. $M_S \rightarrow M_S^0$ as $V_\gamma \rightarrow \infty$ is shown in (b).

Published M_S data were collected to assess the validity of the model (Brofman and Ansell, 1983; Takaki *et al*., 1993; Jiang *et al*., 1996; Jun and Choi, 1998; Huang and Xu, 2006; García *et al*., 2008;). The data include lath, plate and ε martensite. All data can be interpreted with the model described here (Fig. 2.8).

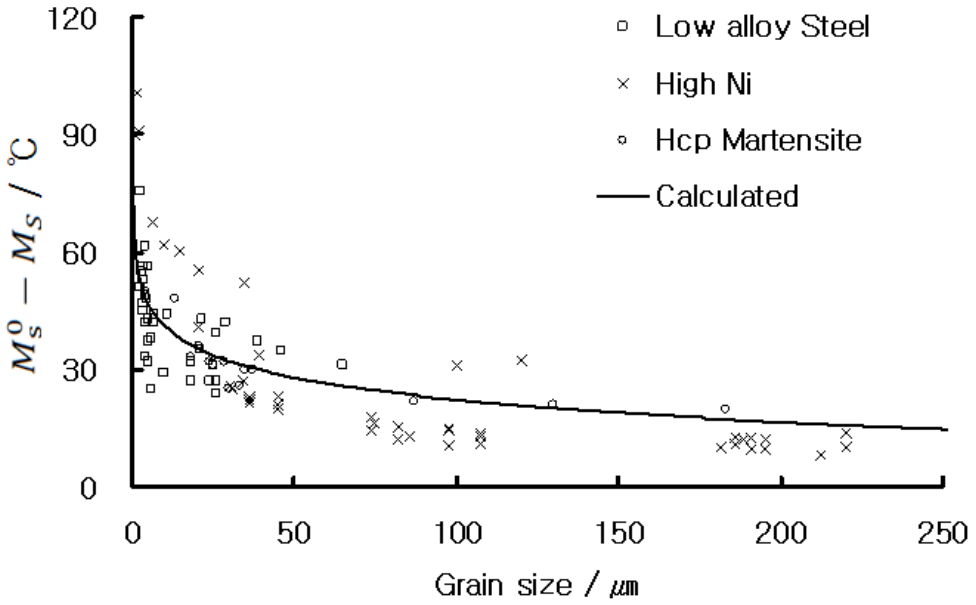

Fig. 2.8: Comparison with data in literature. Data include not only low-alloy lath martensite, but also high-nickel plate and ε martensite.

2.3.3 Athermal Martensite Kinetics

Eq. 2.6 describes the evolution of martensite fraction according to temperature, rather like the Koistinen-Marburger (KM) equation (1959) which was developed by fitting to experimental work and was later justified theoretically (Magee, 1970):

$$\ln(1-f) = -\alpha(M_S - T) \tag{2.7}$$

where α is fitting constant 0.008-0.02 $℃^{-1}$ in plain carbon steels (Bohemen and Sietsma, 2009). The KM equation is eventually identical with eq. 2.6 except at the early stages of transformation. When the fraction is large enough (f >0.1) eq. 2.6 simplified as follow:

$$M_S^0 - T \approx \frac{1}{b}\ln\left[\frac{1}{V_\gamma}\exp\left\{-\frac{\ln(1-f)}{m}\right\}\right] \tag{2.8a}$$

$$\ln(1-f) \approx -m \cdot \ln\left[V_\gamma \exp\{b(M_S^0 - T)\}\right] \tag{2.8b}$$

$$\ln(1-f) = -m \cdot \ln V_\gamma - mb(M_S^0 - T) \tag{2.8c}$$

The $(-m \cdot \ln V_\gamma)$ term comes here because of different definitions of M_S^0 and M_S. If V_γ is large enough, then this term diminishes and M_S^0 tends towards M_S. Therefore, mb corresponds to α in the KM equation. The curve in Fig. 2.7 used a fitting constant of b=0.2689 ℃$^{-1}$ which corresponds to α=0.013 ℃$^{-1}$. Similarities between them are shown in Fig. 2.8 where the two relationships differ only at the early stages of transformation. The fraction of martensite starts to increase abruptly at M_S in the KM equation, but gradually in eq. 2.6 which is more reasonable and closer to experimental observation. Bohemen *et al*. (2008) also mentioned that M_S in KM equation is lower than measured values.

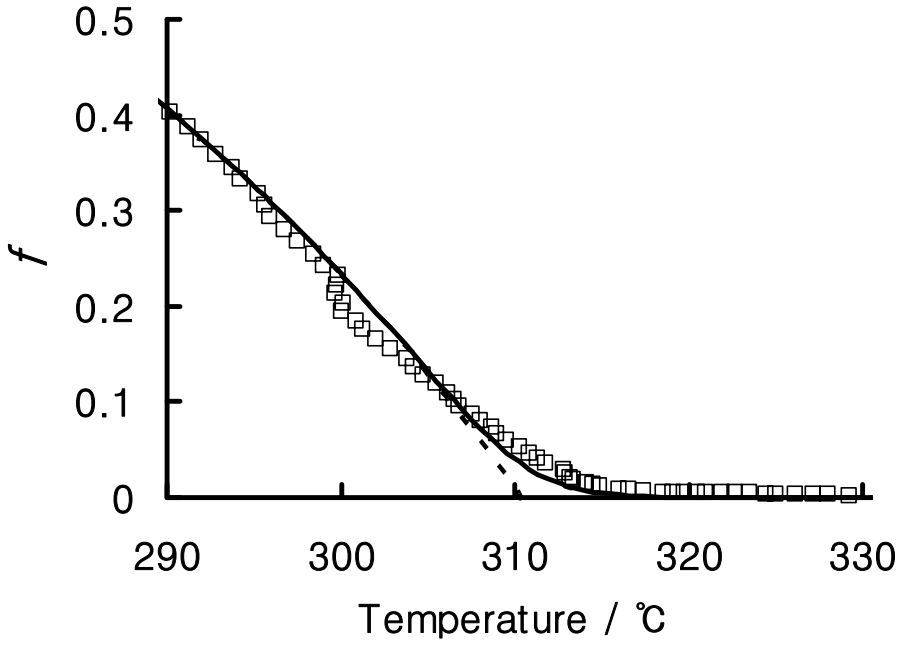

Fig. 2.8: Comparison between the model developed here and the KM equation. Squares represent measured data, sample austenitised at 850 ℃. Solid and dashed lines represent eq. 2.6 and the KM equation respectively. There is no essential difference when *f* is large.

2.4 Summary

New experimental evidence confirmed the dependence of M_S on the prior austenite grain size. The Fisher model for the geometrical partitioning of austenite grains by plates of martensite was used to develop a theory to explain the observations, based on the ability to detect transformation as a function of the austenite grain size. It was assumed that the number of nuclei as a function of temperature is the same regardless of grain size. However, large grained samples reach the detectable amount of martensite faster which results in a high M_S. The relationship derived has been tested on wide range of published data. The relationship not only explains the M_S dependence on grain size but can also be used to describe athermal martensite kinetics. The evolution of martensite fraction is described better by the equation developed here than the KM equation especially at early stages of the transformation.

Chapter 3: Athermal Martensite Kinetics

3.1 Introduction

The effect of the austenite grain size on M_S has been discussed in chapter 2, embodied in eq. 2.6. The next question that arises is the dependence of martensite fraction evolution as a function of grain size and temperature.

The fitting constant in the KM equation (α) represents the kinetics of athermal martensite. The equation was developed empirically and later justified by Magee (1970) to show that the fitting constant is:

$$\alpha = -\bar{V}\varphi \frac{\partial \Delta G^{\gamma \to \alpha}}{\partial T} \tag{3.1}$$

where $\bar{V}$ is average volume of martensitic plates, φ is a constant and $\Delta G^{\gamma \to \alpha}$ is the free energy change. $\bar{V}$ and $\partial \Delta G^{\gamma \to \alpha} / \partial T$ were assumed to be constant, with the former decreasing at small grain sizes. Therefore, Magee's theory predicts that a large grain sample would show a faster reaction rate. Lee and Lee (2005) investigated the grain size effect on martensite kinetics in a low alloy steel. They concluded that a small grained sample transforms rapidly at the early stages of the transformation whereas a large grained sample is fastest at the intermediate stage. Transformation rate are the same regardless of grain size eventually at the last stage. However, they analysed only nine martensite fraction data, and the trend was not clear. Therefore, the work presented in this chapter aims to investigate the effect of austenite grain size on the kinetics of athermal martensite.

3.2 Experimental

The dilatometric data obtained in chapter 2 were used to analyse the martensite kinetics, after conversion into phase fraction using the lever rule (Fig. 3.1):

$$f = \mathrm{B}/(\mathrm{A}+\mathrm{B}) \tag{3.2}$$

Two fitting lines representing the fully austenitic and martensitic strains are required to estimate *f*. The austenite contraction line was obtained based on data roughly

from M_S+50 ℃ to M_S+300 ℃, R^2 value for austenite contraction line usually exceeded 0.9999 where R is the correlation coefficient. Martensitic transformation finishes at room temperature as shown in X-ray diffraction data or using microscopy (Fig. 3.2 and 3.3). However, it was difficult to get a martensite contraction line because the temperature range where the cooling curve becomes linear is narrow. Therefore, the expansion line of martensite was obtained based on heating curve from 50 ℃ to M_S. The heating line was then moved to make contact with the cooling curve at 50 ℃, which was set as martensite contraction line, as shown in Fig. 3.1.

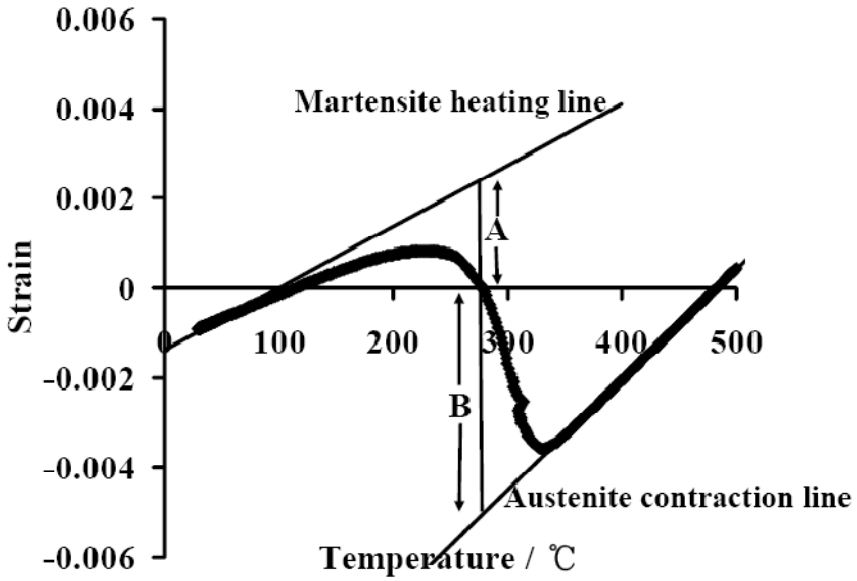

Fig. 3.1: Conversion of dilatometric curve into martensite fraction. Sample austenitised at 1100 ℃ for 600 s.

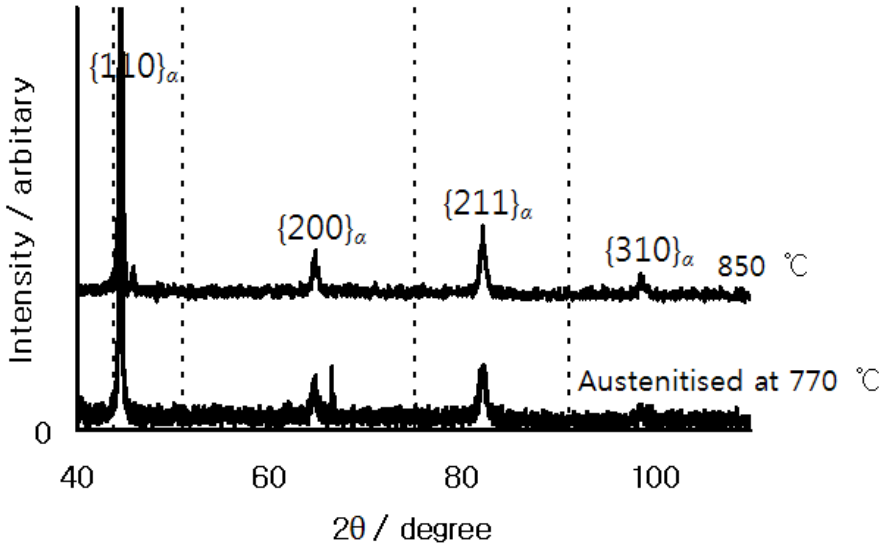

Fig. 3.2: Examples of X-ray diffraction. The dashed lines represent positions where austenite is expected to contribute.

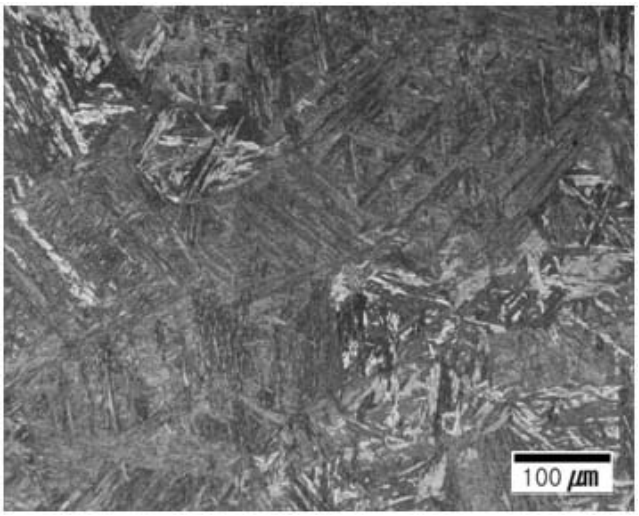

Fig. 3.3: Fully martensitic microstructure, sample austenitised at 1100 ℃ for 600 s.

3.3 Results and Discussion

Martensitic transformation kinetics can be represented by the fitting constants in the KM equation or eq. 2.6, α and b. Fig. 3.4 shows ln(1-f) as a function of temperature. The slope of the graph corresponds to α. The slope is almost constant when f >0.2, but is more gentle at the early stages of decomposition. Therefore α was calculated in the two ranges of f 0.01-0.2 and 0.2-0.8.

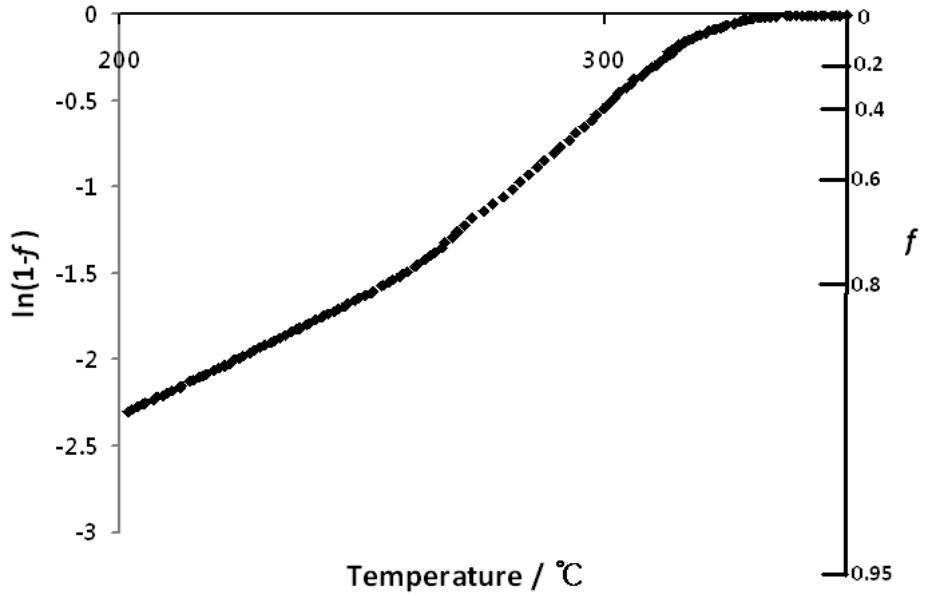

Fig. 3.4: ln(1-f) as a function of temperature, sample austenitised at 1100 ℃ for 600 s.

The calculation are shown in Fig. 3.5. The α values fall into two widely separated ranges consistent with the form of the curve illustrated in Fig. 3.4. The α values are also more sensitive to grain size at the early stages of transformation. The analysis demonstrates clearly that transformation rate of small grain sized sample is faster at the early stages.

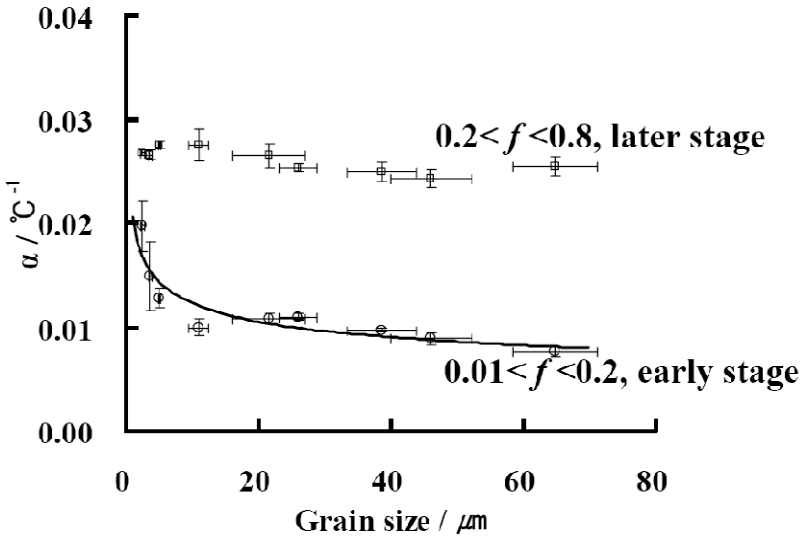

Fig. 3.5: Fitting constant in the KM equation, α as a function of austenite grain size and the stages of transformation.

Fitting constants b in eq. 2.6 were calculated by converting martensite fraction data into N_V. The results are shown in Fig. 3.6, and also show that small grain sized sample is faster in kinetics at the early stages of the martensite transformation.

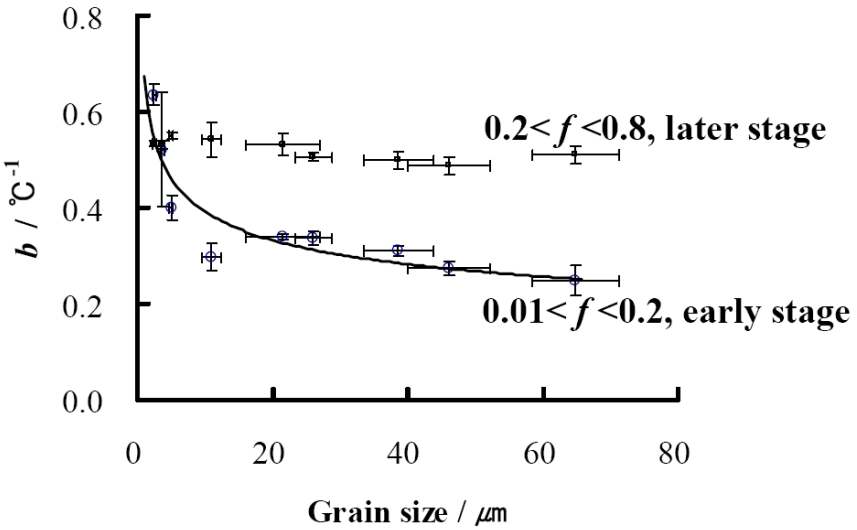

Fig. 3.6: Fitting constant in eq. 2.6, b as a function of austenite grain size and the stages of transformation.

The instantaneous transformation rate ($-\mathrm{d}f/\mathrm{d}T$) has been analysed to investigate the martensite kinetics in detail as shown in Fig. 3.7. As mentioned in chapter 2, the KM equation describes the onset of the transformation as abrupt, which is not consistent with experimental observations. Eq. 2.6 on the other hand, describes a gradual onset. The transformation rate increases steeply from zero, goes through a maximum and then declines smoothly as temperature decreases. The decline is simply a reflection of the decrease in the quantity of parent phase available for transformation.

Fig. 3.8 illustrates the measured transformation rate of different austenite grain sized samples. Previous analysis showed that small grain sizes samples have large b value at the early stages of transformation, clearly shown in Fig. 3.8b, with grain size dependence decreasing as the austenite is exhausted.

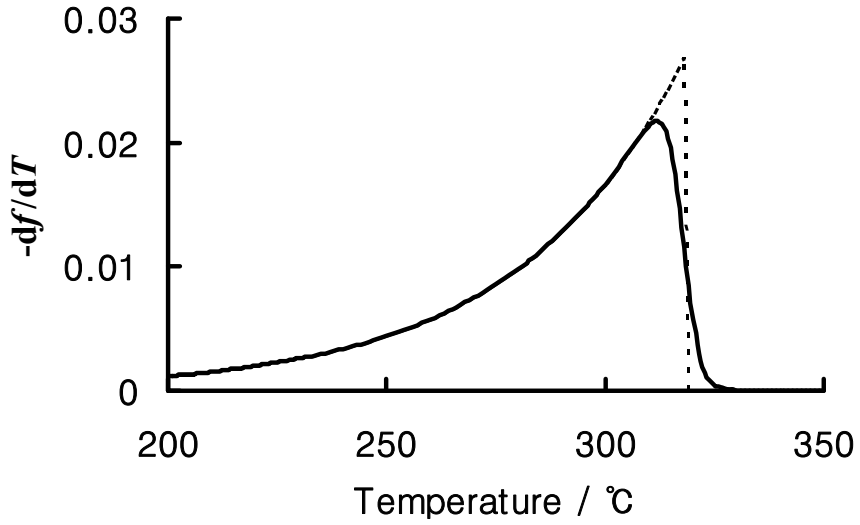

(a)

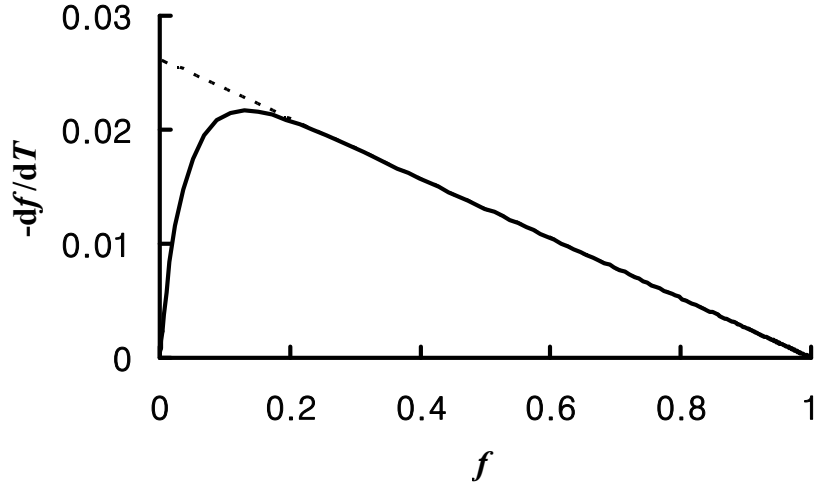

(b)

Fig. 3.7: Transformation rate according to (a) temperature and (b) martensite fraction. Solid lines represent eq. 2.6 and dashed lines represent the KM equation.

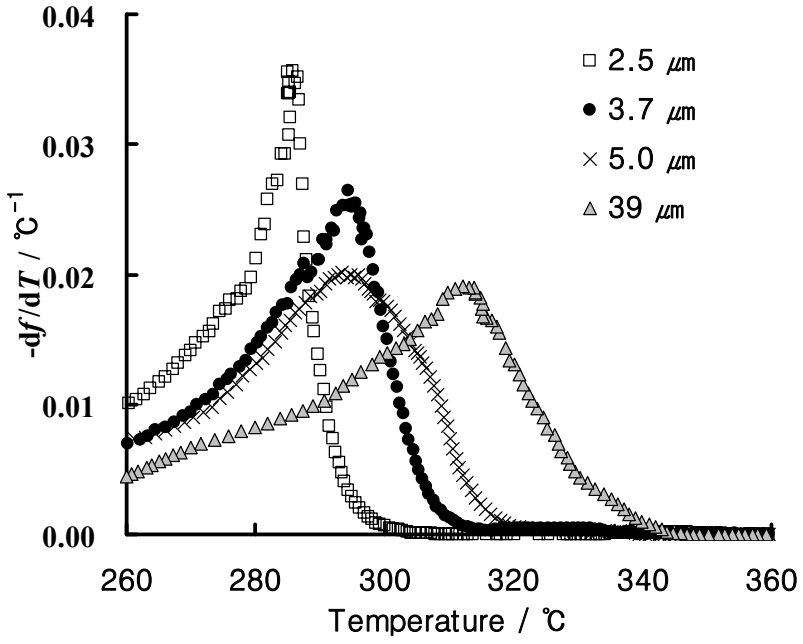

(a)

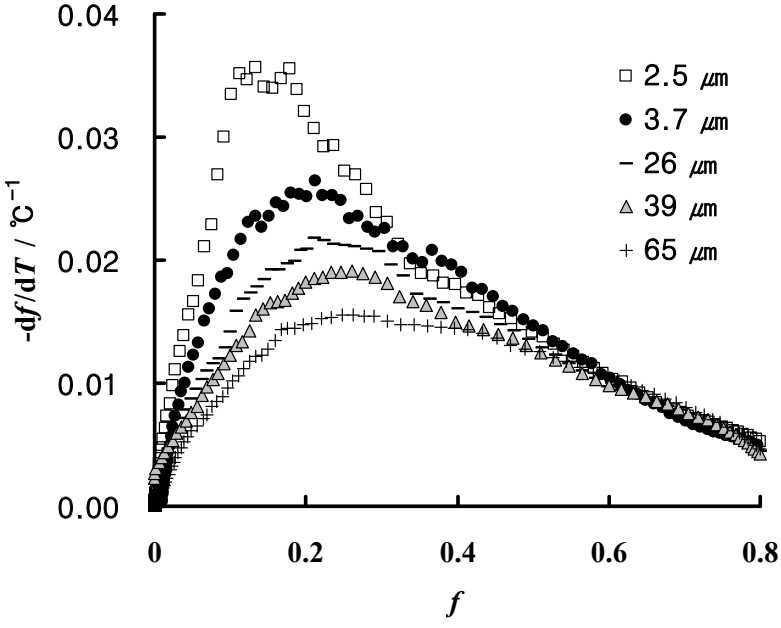

(b)

Fig. 3.8: Measured –d*f*/d*T* according to (a) temperature and (b) fraction. Selected samples among 9 different grain size samples are shown for the clarity.

A qualitative explanation involves the number of initial nucleation sites. Olson *et al*. (1987) measured initial martensite nucleation events before autocatalysis happens, as a function of a function of austenite grain size, using sensitive acoustic emission measurements. They derived the form describing the grain size dependence of preexisting nucleation sites as follow:

$$N_V^0 = k_1 + \frac{k_2}{D^{k_3}} \tag{3.3}$$

where N_V^0 is total number density of preexisting nucleation sites, D is prior austenite grain size and k_1, k_2 and k_3 are constants. A small grain-sized sample can transform faster because of the larger number of initial nucleation sites at the early stages of the transformation. The effect of large number of initial nucleation sites diminishes as the transformation progress because the grain boundary nucleation sites play a minor role compared with autocatalysis. The transformation rate of all samples decreases because untransformed austenite decreases as the reaction progress.

3.4 Summary

The effect of prior austenite grain size on the evolution of martensite transformation below the start temperature has been analysed. The athermal transformation rate starts from zero, rapidly increases until a fraction $\cong$ 0.15, and then decreases smoothly. Small grain-sized samples transform rapidly at the early stages because of larger number of initial nucleation sites. However, the grain size dependence diminishes at the later stages because of autocatalysis and decreasing untransformed austenite.

Chapter 4: Martensite-Start Temperature for the $\gamma \rightarrow \varepsilon$ Transformation

4.1 Introduction

Thermodynamic calculations of martensite-start temperature were reviewed in chapter 1; martensite is triggered when the free energy change for transformation without a composition change reaches a critical value, the magnitude of which is determined by stored energies and kinetic phenomena. The method has been applied with some success to the $\gamma \rightarrow \alpha'$ transformation and forms the basis of computer programs which take as inputs the thermodynamic parameters of the parent and product phases and output the transformation–start temperature[*]. In this way, the incorporation of a previously excluded element on the M_S temperature simply requires an understanding of how this element alters the thermodynamic stabilities of the phases involved.

Iron in which the atoms are arranged on a hexagonal lattice is designated ε. Although this is not a common allotrope in alloyed iron at ambient pressure, it is becoming of increasing importance in low–carbon, often low density, structural steels containing unconventionally large concentrations of manganese (Grässel *et al*., 2000; Frommeyer *et al*., 2003; Embury and Bouaziz, 2010). It is also the basis of many iron–based shape memory alloys (Sato *et al*., 1984; Li and Wayman, 1994; Tomota and Maki, 2000). The ε therefore features in reversible martensitic transformations and in steels where its transformation plasticity is exploited. It is important therefore, in the process of alloy design and optimisation, to be able to calculate its martensite–start temperature, at least as a function of the chemical composition.

[*] For example, University of Cambridge and NPL. Materials Algorithms Project, www.msm.cam.ac.uk/map/mapmain.html

The last attempt at dealing with this issue was by Dogan and Ozer (2005) who derived an empirical equation using linear regression analysis on some 17 iron–based alloys which undergo the $\gamma \rightarrow \varepsilon$ martensitic transformation as follows:

$$M_S / \mathrm{K} = 246 - 5.8w_{Mn} + 38.5w_{Si} - 61.5w_{Cr} - 5.1w_{Ni} + 138w_{Ce} - 146w_{Ti} - 96w_N \quad (4.1)$$

where w represents the weight percent of the element identified in the subscript. The equation was derived for the concentration ranges 13.0–31.5Mn, 4.7–7.0Si, 0–11.6Cr, 0–6.8Ni wt %; Ce, Ti and N were each present in only one alloy with values of 0.3, 0.6 and 0.3 wt % respectively. Standard errors were not quoted but the deviation from a fit to this equation were typically less than ± 20 K. They also considered the use of thermodynamics as described above; however, neither the origin of the thermodynamic data nor the calculations of M_S temperatures were presented in the paper, so it is not clear what was achieved. The purpose of this chapter is to take a fresh look at this problem given the much larger availability of data due to increased modern interest in low density and TRIP (transformation induced plasticity) steels based on the ε phase.

4.2 Measurements of ε-Martensite Start Temperatures

Some of the data in the literature were hard to understand using thermodynamic calculations, which will be shown later. Therefore, it was required to check the level of experimental error expected in measuring the start temperature for ε, given that the volume change of transformation might in some cases be rather small (Brooks *et al.*, 1979a; b). A set of six alloys showing a variation in manganese and silicon concentrations, was prepared as 300 g melts, which were cast and vacuum sealed. They were then homogenised for 2 days at 1473 K, after which their chemical compositions were measured as listed in Table 4.1. Cylindrical dilatometer samples 5 mm diameter and 10 mm long were machined and studied using a BAHR DIL805 dilatometer. The samples were heated at 2 K s^{-1} in a vacuum to 873 K for 1 min, and then quenched at 10 K s^{-1} using argon gas to room temperature. Optical

micrography was used to confirm the existence of ε-martensite and two representative examples are shown in Fig. 1.

Table 4.1: Alloy compositions and measured M_S temperatures.

Alloy designation	Mn / wt%	Si / wt%	M_S / K
16Mn 0Si	15.8	0.0	410 ± 3
16Mn 3Si	15.6	2.7	437 ± 7
16Mn 6Si	16.0	5.4	422 ± 1
25Mn 0Si	24.8	0.1	< 293
25Mn 3Si	25.3	2.8	343 ± 2
25Mn 6Si	25.0	5.2	341 ± 1

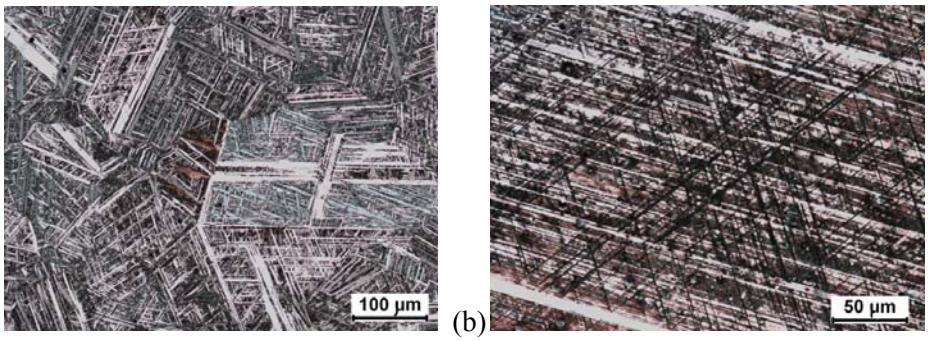

Fig. 4.1: Optical micrographs showing ε-martensite. (a) 16Mn 0Si alloy. (b) 25Mn 3Si alloy.

The results of dilatometric experiments are presented in Fig. 4.2. The Offset method introduced in chapter 1 was used to measure M_S. The technique defines the first onset of transformation to be that at which a critical strain is achieved relative to the thermal contraction of the parent phase. In the present work the critical strain has been taken as 1/100 of the total transformation strain determined at ambient temperature for the 16Mn 0Si alloy, equal to -4.6×10^{-5}. This magnitude is less than

half of the value used in $\alpha`$ M_S measurement, 1.21×10^{-4} (Yang and Bhadeshia, 2007) but enough to make reproducible and clear measurements of M_S (Fig. 4.3). Note that although this small offset should be greater than the noise in the data, it is an arbitrary but reproducible value which is used for all the alloys. It is akin to the arbitrary, small strain used in defining the proof strength in a gradually yielding tensile test.

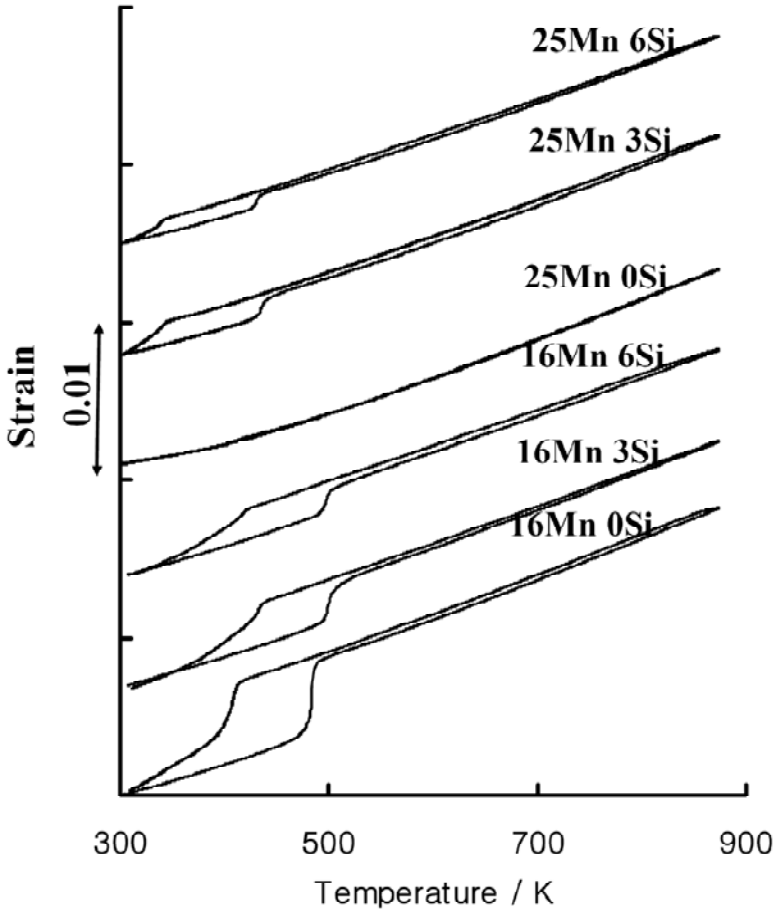

Fig. 4.2: Heating and cooling dilatometric data for all of the experimental alloys. Note that there is a contraction when ε-martensite forms from austenite. The data here are presented with a compressed vertical axis for the sake of brevity.

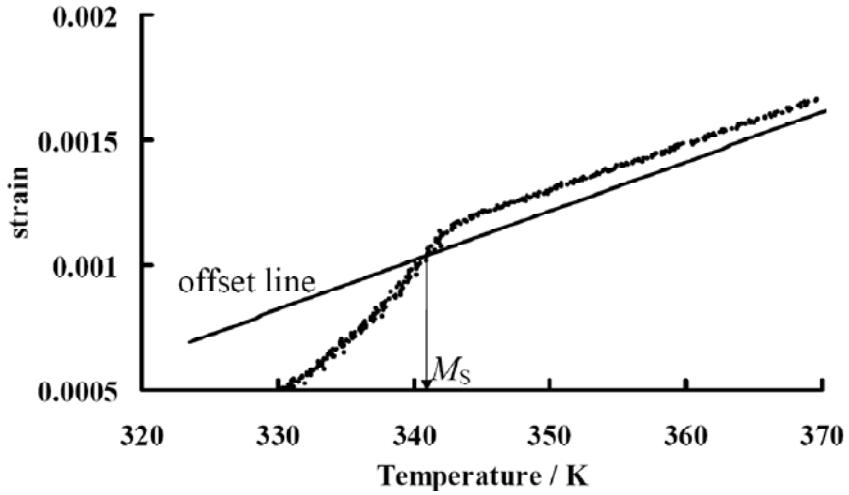

Fig. 4.3: Determination of M_S for 25Mn 6Si alloy of which volume contraction is the smallest.

Samples were quenched 5 times, and averaged M_S values are shown in Table 4.1. It is clear that uncertainties in the determination of ε-martensite start temperatures are small.

4.3 Estimation of ε-Martensite Start Temperatures

There are several approaches to predict M_S as reviewed in chapter 1. Most of the efforts focused on α` martensite. ε-martensite is becoming of increasing importance in low–carbon, often low density, structural steels containing unconventionally large concentrations of manganese; therefore prediction of ε $M_S$ is important. Strategies similar to those used in α` have been applied to ε-martensite here.

4.3.1 Empirical Equation

A search of the literature revealed a large number of sources of data which yielding some 328 combinations of chemical composition and martensite–start temperatures (see Table 4.2). The elements included C, Mn, Ni, Cr, Al, Si, Mo, Co, Cu, Nb, Ti, V and W. The data were subjected to multiple regression analysis to

yield the following relationship which has a standard error of ± 26 K and a correlation coefficient of 0.9:

$$M_S / \mathrm{K} = 576 \pm 8 - (489 \pm 31) w_C - (9.1 \pm 0.4)\, w_{Mn} - (17.6 \pm 2)\, w_{Ni} - (9.2 \pm 1)\, w_{Cr} + (21.3 \pm 2)\, w_{Al} + (4.1 \pm 1)\, w_{Si} - (19.4 \pm 5)\, w_{Mo} - (1 \pm 1)\, w_{Co} - (41.3 \pm 6)\, w_{Cu} - (50 \pm 18)\, w_{Nb} - (86 \pm 12)\, w_{Ti} - (34 \pm 10)\, w_V - (13 \pm 5)\, w_W \quad (4.2)$$

The extent of the fit is illustrated in Fig. 4.4 and forms a rough method of estimating the martensite– start temperature but the linear relationship and the implied lack of dependencies between the independent variables clearly cannot be justified as reviewed in chapter 1.

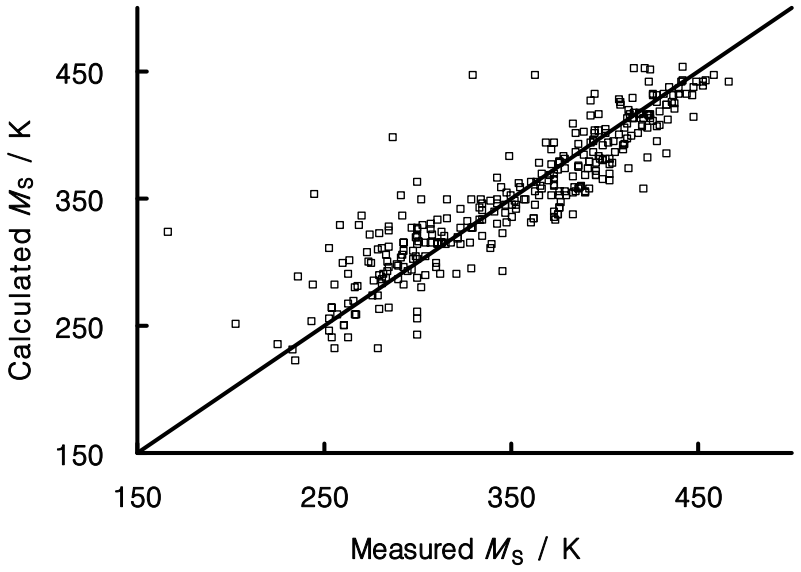

Fig. 4.4: The ε-martensite M_S temperatures estimated using eq. 4.2, versus measured values.

Table 4.2: Epsilon M_S data compiled from the literature. Compositions are in wt %.

#	C	Mn	Ni	Cr	Al	Si	Mo	Co	Cu	Nb	Ti	V	W	M_S / K	$\Delta G_{M_S}^{\gamma\rightarrow\epsilon}$ / J mol^{-1}	Reference
1		31.5				6								293	-29	Dogan and Ozer, 2005
2		27.6		5		6.1								283	901	
3		20.4	5	8		5								261	1837	
4		19.9	5	10.1		5								225	2063	
5		17.5	5.5	8.5		5.1								254	1858	
6		16.9	6.3	10		5								254	2115	
7		16.5	5	8.4		5.1								244	1707	
8		16	4.9	11.6		5								267	2127	
9		13.7	4.4	8		5								274	1459	
10		13.3	5.8	9.6		4.9								276	1812	
11		13	6.8	11.4		4.7								243	2004	
12		25		7		6								279	1212	
13		21		9		6								285	1505	
14	0.07	20.32		2.14										383	-1	Dai *et al*., 2004
15	0.11	16.81		0.18	1.45									287	-381	
16	0.35	18.05		0.19	0.18									263	-97	
17		30.3				6.06								323	-29	
18		26.36				5.87								354	-60	
19		23.37				5.91								372	-83	
20	0.04	20.2		4.1										373	-8	
21	0.16	19.73												322	-159	
22		24				6								378	-64	
23	0.02	17.68												428	-10	
24	0.1	17.84												373	-129	

Table 4.2: (Continued)

#	C	Mn	Ni	Cr	Al	Si	Mo	Co	Cu	Nb	Ti	V	W	M_S / K	$\Delta G_{M_S}^{\gamma\rightarrow\epsilon}$ / J mol^{-1}	Reference
25	0.2	17.86												328	-153	Dai *et al*., 2004
26	0.28	17.32												302	-177	
27		24.3				3								396	-42	
28		24.9				2.2								388	-50	
29		26				3.7								379	-51	
30		27.3				3.4								376	-41	
31		27.9				2.6								362	-60	Sade *et al*., 1990
32		27.8				3.2								375	-37	
33		27.6				3.6								335	-101	
34		28.9				4								361	-40	
35		31.5				4.4								298	-54	
36		32				3.9								300	-45	
37		32.9				3.5								295	-22	
38		33.9				4.1								281	1	
39		35.9				4								263	60	
40	0.02	29.4				6								285	-56	Liu *et al*., 1999
41	0.013	28.3				6.8								323	-36	Caenegem *et al*., 2008
42	0.018	29		5		6.9								283	1042	
43		26.76				0								316	-78	Takaki *et al*., 1990
44		26.32				2.11								335	-132	
45		26.55				4.06								350	-90	
46		26.74				7.12								300	-87	
47		16												426	-65	Lee and Choi, 2000
48		18												412	-79	
49		20												394	-103	

Table 4.2: (Continued)

#	C	Mn	Ni	Cr	Al	Si	Mo	Co	Cu	Nb	Ti	V	W	M_S / K	$\Delta G_{M_S}^{\gamma\rightarrow\epsilon}$ / J mol^{-1}	Reference
50		22												372	-129	Lee and Choi, 2000
51		24												345	-136	
52	0.006	15.7				0.01								437	-24	Tomota *et al*., 1986
53	0.003	16.4				0.02								428	-48	
54	0.001	19.8				0.01								394	-106	
55	0.002	24.4				0.02								348	-117	
56		17.7												397	-137	Jun and Choi, 1998a
57		17.7												414	-77	
58		17.7												419	-60	
59		17.7												423	-46	
60		17.7												425	-39	
61	0.002	24.03												421	52	Tomota *et al*., 1998
62	0.003	24.29				5.88								392	-41	
63	0.02	17.1												426	-27	Lee *et al*., 1996
64	0.025	13.4												454	19	Lee *et al*., 1997
65	0.028	16.2												424	-42	
66	0.019	17												415	-69	
67	0.021	21.3												375	-117	
68	0.018	23												355	-129	
69	0.015	23.2												387	-51	Jun *et al*., 1998
70	0.011	23.3						1.23						384	11	
71	0.018	23.2						2.3						383	70	
72	0.011	23.1						3.42						386	133	
73	0.015	17.2												421	-48	Jun and Choi, 1998b
74	0.015	17.2												425	-34	Jun and Choi, 1998c

Table 4.2: (Continued)

#	C	Mn	Ni	Cr	Al	Si	Mo	Co	Cu	Nb	Ti	V	W	M_S / K	$\Delta G_{M_S}^{\gamma\rightarrow\epsilon}$ / J mol^{-1}	Reference
75	0.01	20.18												410	-39	Jun and Choi, 1998c
76	0.015	23.28												392	-35	
77		13.7												422	-122	Cote *et al*.,1995
78		13.7												416	-144	
79		15.9												432	-45	
80		15.9												426	-67	
81		15.9												444	-1	
82		15.9												440	-15	
83		19.3												401	-93	
84		19.3												395	-113	
85		19.3												418	-36	
86		21.9												396	-61	
87		21.9												404	-37	
88		21.9												376	-120	
89		24.7												380	-48	
90		24.7												376	-59	
91		24.7												372	-68	
92		24.7												365	-81	
93		25.1												329	-120	
94		25.1												302	-141	
95		25.1												334	-116	
96		25.1												316	-131	
97		26.5												292	-97	
98		26.5												270	-101	
99		27.3												303	-67	

Table 4.2: (Continued)

#	C	Mn	Ni	Cr	Al	Si	Mo	Co	Cu	Nb	Ti	V	W	M_S / K	$\Delta G_{M_S}^{\gamma \rightarrow \epsilon}$ / J mol^{-1}	Reference
100		27.3												269	-72	Cote *et al*.,1995
101		27.3												259	-72	
102		27.7												307	-53	
103		29.3												253	-3	
104		29.3												281	-8	
105		22.89												390	-61	Lenkkeri and Levoska, 1983
106		20.36												399	-80	Umebayashi and Ishikawa, 1966
107		22.08												386	-88	
108		26.21												347	-68	
109		26.82												374	-14	
110	0.004	14.69				0.01								424	-92	Takaki *et al*., 1993
111	0.004	14.69				0.01								441	-29	
112	0.004	14.69				0.01								449	1	
113	0.004	14.69				0.01								453	16	
114		32.6				4.2								289	-31	Cotes *et al*., 1998
115		25.6				1								339	-127	
116		28.4				0.99								280	-74	
117		32.3				5								304	-31	
118		17.4				4.5								448	-13	
119		17.5				1.9								436	-23	
120		19.5				2								420	-43	
121		20				4.1								434	-13	
122		22.2				4								410	-39	
123		24.2				1.9								399	-33	

Table 4.2: (Continued)

#	C	Mn	Ni	Cr	Al	Si	Mo	Co	Cu	Nb	Ti	V	W	M_S / K	$\Delta G_{M_S}^{\gamma \rightarrow \epsilon}$ / J mol^{-1}	Reference
124		24.5				4.2								396	-38	Cotes *et al*., 1998
125		25.3				6.4								379	-41	
126		22.7				1								386	-85	
127		29.5				5.2								343	-39	
128		25.9				1.8								358	-99	
129		28.3				2.6								348	-77	
130		30				2.7								318	-74	
131		20.4				0.95								405	-68	
132		19.8				2.03								411	-64	
133		26.5				4.69								376	-44	
134		28.8				4.74								351	-46	
135		22.9				6.1								402	-43	
136		24.4				6.4								379	-54	
137		27				5.9								363	-42	
138		29.5				5.8								335	-37	
139		19.9				1.05								408	-67	
140		22.1				1								399	-58	
141		23.9				0.99								370	-105	
142		22.8				2.78								401	-50	
143		23.6				2.6								391	-62	
144		18.9				3.2								430	-31	
145		21.9				4.76								412	-40	
146	0.045	14												393	-178	Georgiyeva *et al*., 1981
147	0.03	18.5												373	-173	
148	0.02	22.1												343	-176	

Table 4.2: (Continued)

#	C	Mn	Ni	Cr	Al	Si	Mo	Co	Cu	Nb	Ti	V	W	M_S / K	$\Delta G_{M_S}^{\gamma \rightarrow \epsilon}$ / J mol^{-1}	Reference
149	0.02	13.8		10										343	-234	Ishida and Nishizawa, 1974
150	0.02	14.4		12.3										346	-218	
151	0.02	13.9		13.7										311	-307	
152	0.03	21.9		9.7										276	8	
153		16.6			0.3									395	-178	
154		15.9			0.72									363	-319	
155		17.2			1.23									330	-408	
156		16.1						0.97						415	-38	
157		17.3						2.01						416	35	
158		17.2						3						419	123	
159		17.1		0.9										416	-57	
160		17		1.89										401	-85	
161		17.2		2.9										393	-89	
162		17.11							1.04					365	-187	
163		17.3							2.09					333	-212	
164		17.2							3.08					284	-273	
165		17					1.54							386	-222	
166		16.9					3.08							364	-332	
167		16.6					4.46							341	-435	
168		16.9								0.42				389	-188	
169		17								0.85				376	-238	
170		17.2								1.21				366	-279	
171		17.1	0.99											395	-33	
172		17.2	1.51											369	-58	
173		17.2	2.12											349	-50	

Table 4.2: (Continued)

#	C	Mn	Ni	Cr	Al	Si	Mo	Co	Cu	Nb	Ti	V	W	M_S / K	$\Delta G_{M_S}^{\gamma \rightarrow \epsilon}$ / J mol^{-1}	Reference
174		17.1				0.51								409	-108	Ishida and Nishizawa, 1974
175		17.11				1								409	-109	
176		17				1.5								408	-115	
177		17.3									0.58			373	-93	
178		16.8									1.2			335	-88	
180		16.7										0.71		385	-224	
181		17.2										1.52		367	-304	
182		17.4										2.2		351	-377	
183		17											1.44	397	-169	
184		17											3.01	389	-217	
185		17.3											4.48	361	-323	
186	0.1	15.4												385	-125	
187	0.18	15.6												353	-150	
188	0.28	15.7												329	-121	
189		13.6												442	-48	Gulyaev *et al*., 1978
190		14.7												442	-29	
191		15.4												440	-24	
192		16												428	-58	
193		16.86												433	-25	
194		19.5												415	-44	
195		20												428	10	
196		21.36												397	-68	
197		15.24												453	22	Troiano and McGuire, 1943
198		16.74												438	-9	
199		20.23												411	-43	

Table 4.2: (Continued)

#	C	Mn	Ni	Cr	Al	Si	Mo	Co	Cu	Nb	Ti	V	W	M_S / K	$\Delta G_{M_S}^{\gamma \rightarrow \epsilon}$ / J mol^{-1}	Reference
200	0.07	20.12	0.01			0.33								373	-103	Bogachev and Malinov, 1962
201	0.27	20.01	0.05			0.3								300	-68	
202	0.08	19.36	0.11			1.86								383	-71	
203	0.06	20.5				0.1								373	-105	Bogachev *et al*., 1968
204	0.06	20.1		2.2		0.1								363	-64	
205	0.04	19.8		5.8		0.1								313	-101	
206	0.04	20.3		9.8		0.1								293	-14	
207		30			3	3								398	-28	Eskil and Kanaca, 2008
208		30			3	4								433	26	
209		30			5	2								413	-86	
210		35			5	1								403	-64	
211		35			5	4								423	-38	
212		30			2	4								403	8	
213		30			5	1								393	-126	
214		30			5	3								433	-52	
215		35			5	2								413	-51	
216		35			3	4								373	2	
217		30			3	2								403	-22	
218		15	5	9		5								304	1803	Druker *et al*., 2010
219	0.016	30.1				6.01								314	-27	Yang *et al*., 2009
220	0.006	15.7				0.01								447	12	Tsuzaki *et al*., 1991
221	0.002	24.4				0.02								390	-31	
222		28.1				5.9								343	-48	Otsuka *et al*., 1990
223		32.3				6								293	46	
224		26		5		5.9								299	859	

Table 4.2: (Continued)

#	C	Mn	Ni	Cr	Al	Si	Mo	Co	Cu	Nb	Ti	V	W	M_S / K	$\Delta G_{M_S}^{\gamma\rightarrow\epsilon}$ / J mol^{-1}	Reference
225		28.6		5		6								293	912	Otsuka *et al*., 1990
226		24.7		6.6		5.9								301	1137	
227		17.5	5.5	8.5		5.1								254	1858	
228		20.4	5	8		5								261	1837	
229		22.2	5	8.2		4.9								256	1914	
230		11.2	6.7	11.6		4.7								266	1950	
231		16	4.9	11.6		5								267	2127	
232	0.004	14.06				0.01								459	28	Fujita and Uchiyama, 1974
233	0.005	16.9				0.01								438	-1	
234	0.004	18.58				0.01								423	-27	
235	0.005	22.65				0.01								371	-114	
236		25						5						347	132	Hamers and Wayman, 1991
237		25						8						353	285	
238		30						5						310	181	
239		30						8						310	277	
240		24.3				3								396	-42	Donner *et al*., 1989
241		26				3.7								385	-40	
242		26				3.7								390	-31	
243		27.3				3.4								376	-41	
244		27.9				2.6								362	-60	
245		27.8				3.2								375	-37	
246		30.3				4.7								308	-68	
247		32				3.9								298	-45	
248		17.9						5.1						383	138	Baruj *et al*., 1995
249		18.1						3.0						412	-468	

Table 4.2: (Continued)

#	C	Mn	Ni	Cr	Al	Si	Mo	Co	Cu	Nb	Ti	V	W	M_S / K	$\Delta G_{M_S}^{\gamma \rightarrow \epsilon}$ / J mol^{-1}	Reference
250		17.9						0.8						416	-451	Baruj *et al*., 1995
251		21.1						5.0						392	202	
252		20.6						3.0						394	89	
253		21.4						1.1						403	18	
254		24.8						2.9						357	50	
255		25.1						1.0						352	-44	
256		29.3						5.3						292	161	
257		29.1						1.0						285	18	
258		29.8						5.1						274	155	
259		30.0						5.1						260	153	
260		30.3						5.5						285	184	
261		31.0						6.0						280	210	
262		16.1				1.7								435	-45	
263		19.0				2.6								448	24	
264		19.5				1.6								420	-40	
265		20.0				3.1								430	-16	
266		14.79												467	67	Acet *et al*., 1995
267		24.7												291	-169	
268		21												406	-46	Jee *et al*., 1995
269	0.018	31.6				6.45								273	-8	Bouraoui *et al*., 1995
270	0.016	18.5	5.03	7.96		4.75	0.15							253	1670	
271		20		7		6			1					300	1185	Dunne and Li, 1995
272	0.002	16.34				5.73								425	-82	Tomota and Yamaguchi, 1995
273	0.22	17.2				0.04								339	-121	
274	0.27	17.1				0.04								300	-173	

Table 4.2: (Continued)

#	C	Mn	Ni	Cr	Al	Si	Mo	Co	Cu	Nb	Ti	V	W	M_S / K	$\Delta G_{M_S}^{\gamma \rightarrow \epsilon}$ / J mol^{-1}	Reference
275	0.007	30.67				4.95								293	-60	Andersson and Ågren, 1995
276		26.4		5.2		6.2								307	952	Jiang *et al*., 1996
277		26.4		5.2		6.2								311	957	
278		26.4		5.2		6.2								311	957	
279		26.4		5.2		6.2								313	958	
280		26.4		5.2		6.2								313	958	
281		20	4.7	8.1		5.1								257	1807	Rong *et al*., 1995
282		29.9				6								307	-49	
283		26.4		5.2		6.02								323	942	Chen *et al*., 1999
284		28.1		5.2		6.1								275	944	
285		30		5.3		6.1								268	996	
286		30.3				6.1								330	-22	
287	0.035	28.4				6.2								297	-50	Dunne and Kennon, 1999
288	0.01	13	5.6	10		4.9								281	1844	
289	0.005	20.4		7.3		5.6			0.97					299	1170	
290		30.3				6.1								300	-45	Wu and Hsu, 2000
291		26.4		5.2		6								315	934	
292		17.8	4.1	7.8		4.7								263	1484	Wen *et al*., 2001
293		17.8	4.1	7.8		4.7								282	1518	
294		17.8	4.1	7.8		4.7								312	1574	
295		17.8	4.1	7.8		4.7								321	1591	
296		30.3				6.1								329	-24	Zhou *et al*., 1998
297		14.6	4.1	8		4.2								304	1316	Wen *et al*., 2004

Table 4.2: (Continued)

#	C	Mn	Ni	Cr	Al	Si	Mo	Co	Cu	Nb	Ti	V	W	M_S / K	$\Delta G_{M_S}^{\gamma\rightarrow\epsilon}$ / J mol^{-1}	Reference
298	0.052	25.4		7.4		6.1			1.1					279	1407	Wang and Zhu, 2004
299	0.045	20.6		9.3		5.83			1					285	1550	
300	0.027	19.6		7.3		6.15			0.97					291	1220	
301		15.45	4.98	9.11		7.03								297	2347	Maji and Krishnan, 2003
302	0.16	19.57				0.05								322	-163	Zhang *et al*., 2002
303	0.04	23.56				0.05								333	-130	
304	0.19	24.09				0.02								280	-25	
305	0.02	24.22				0.02								377	-52	
306	0.14	24.98				0.05								267	-36	
307	0.16	19.33			1.5	0.05								245	-276	
308	0.15	25.61			0.57	0.16								256	-22	
309	0.16	24.84			0.79	0.05								236	-39	
310	0.15	24.89			2.22	0.05								167	-39	
311	0.18	23.32		3.21		0.06								253	56	
312	0.18	22.81		5.34		0.07								233	104	
313	0.02	27.76				4.1								327	-85	
314	0.02	31.8				5.22								284	-25	
315	0.02	32				6.1								264	-4	
316	0.02	31.58		2.06		6.19								290	417	
317	0.18	15.2	4.16	7.92		4.78								235	83	Wen *et al*., 2007
318		20.5		8.9		5.9								311	1490	Gavriljuk *et al*., 2005
319		16.4	4.03	9.2		5.13								346	1883	
320		30.3				5.8								300	-52	Yamaguchi *et al*., 1996

Table 4.2: (Continued)

321		14.3	4.9	9.2		5.1								290	1785	Li *et al*., 1996
322		15.3	5	7.5		5.3					0.6			203	1395	
323		30	2.5	5		7								300	1593	Yang *et al*., 1992
324		30				5		4						300	-8	
325		29	2	4.5		5.5		3.5						300	1174	
326		13.7	4.9	8.3		6								340	1952	
327	0.002	24.03												367	-98	Tomota *et al*., 1992
328	0.002	24.30				5.88								376	-64	

4.3.2 Thermodynamic Calculations

By analogy with the transformation of austenite into α' martensite described in chapter 1, the martensite–start temperature for ε–martensite corresponds to that at which the driving force $\Delta G^{\gamma\rightarrow\epsilon}$ achieves a critical value $\Delta G^{\gamma\rightarrow\epsilon}_{M_S}$. Values of the driving force can in principle be calculated using standard thermodynamic databases in combination with programs such as Thermocalc or MTDATA. In the present work, the TCFE6 database and Thermocalc software were used.

Fe-Mn binary system was examined in detail because every alloy contains manganese at least 11 wt % and there are lots of data for Fe-Mn binary alloys in literature. Fig. 4.5 shows the M_S of Fe-Mn binary alloys as a function of Mn content. There is large scatter in alloys which contain roughly more than 25 wt %. That comes from magnetic transition (Palumbo, 2008). As the manganese content increases, Néel temperature of austenite (T_N^{γ}) decreases, and the intersection point between T_0 and T_N^{γ} is around 25 wt % Mn. Therefore, M_S are depressed further as Mn increases, and the overlapping of magnetic transition and structure transformation makes it difficult to detect M_S, which causes large error.

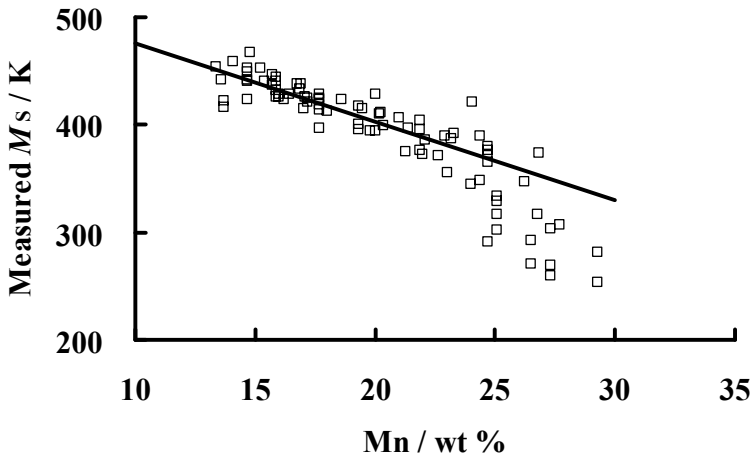

Fig. 4.5: M_S of Fe-Mn binary alloys. Linear line shows the fitted line for alloys of which manganese content is lower than 25 wt %.

The linear part of the Fig. 4.5 (Mn less than 25 wt %) was fitted to a line, expressed as:

$$M_S\ (\mathrm{K}) = 549 - 7.3\mathrm{Mn}\ (\mathrm{wt}\ \%) \quad (4.3)$$

The equation can be used to obtain the driving force at M_S as a function of manganese content. Calculated free energy changes as a function of Mn are shown in Fig. 4.6a, square point represents M_S calculated by eq. 4.3. The Figure was converted into a function of Mn as shown in Fig. 4.6b. If the manganese affects the $\Delta G_{M_S}^{\gamma\rightarrow\epsilon}$, other elements will also do so. However, if every alloy contains high manganese content, the effect of Mn should be dominant. Therefore, the fitted line in Fig. 4.6b was used as critical energy change for the epsilon martensite transformation. The critical driving force therefore varies between -30 and -90 J mol^{-1}. $\Delta G_{M_S}^{\gamma\rightarrow\epsilon}$ was assumed as the only function of manganese. The other elements only affect M_S by varying the relative thermodynamic stabilities of the γ and ε phases.

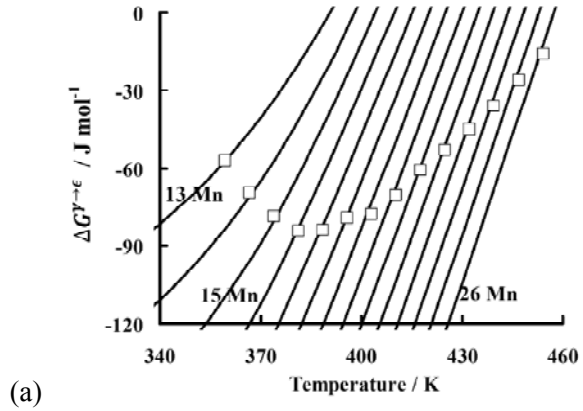

(a)

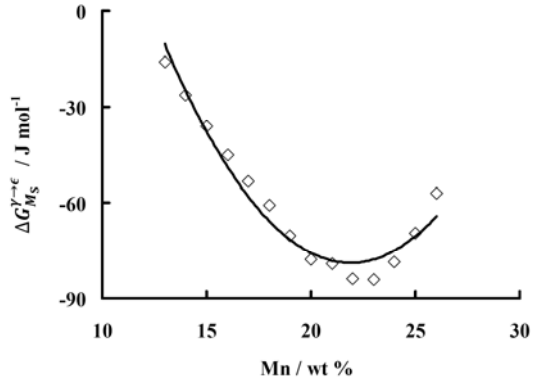

(b)

Fig. 4.6: (a) Calculated free energy change of Fe-Mn alloy for fcc→hcp transformation as a function of temperature and manganese content. The square points represent M_S of each alloy. Differences between lines are 1 wt % manganese. (b) Critical free energy change required for ε-martensite nucleation, as a function of manganese content.

M_S calculation results were different depending on alloy systems. Fig. 4.7 shows the result of the M_S calculation for Fe-Mn binary alloys. The calculated M_S is consistent for the alloys which contain Mn less than 25 wt %, but shows less accordance with high Mn alloys. The essential part of the error is scatter in the data. As shown in Fig. 4.5, there is large scatter in high Mn alloys. The other reason is that the M_S data of high Mn alloys were ignored during the fitting to derive the

critical driving force $\Delta G_{M_S}^{\gamma\rightarrow\epsilon}$. The prediction overestimates M_S because the fitting line is above the measurement points illustrated in Fig. 4.5.

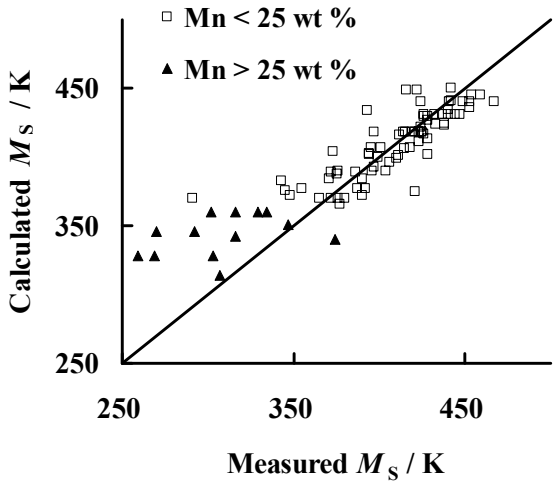

Fig. 4.7: ε-martensite start temperatures of the Fe-Mn binary alloys. It's well predicted when the manganese content is less than 25 wt %.

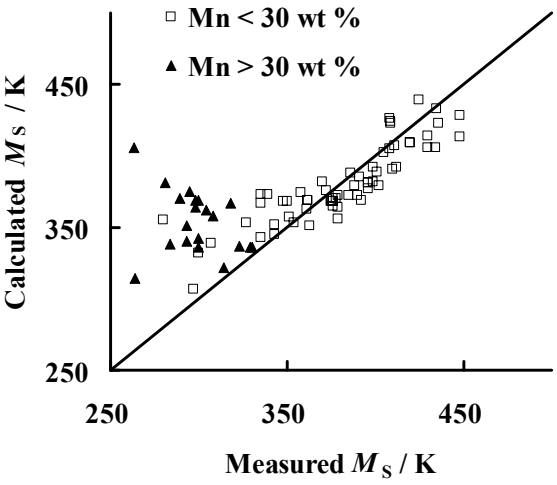

Fig. 4.8: ε-martensite start temperatures of the Fe-Mn-Si ternary alloys. The model predicts well when the manganese content is less than 30 wt %.

The other alloy system where many data are available is Fe-Mn-Si alloys. The model predicts the M_S with reasonable error up to 30 wt % manganese even though the start of the model was fitting up to 25 wt % manganese. However, the accuracy decreases when the manganese content exceeds 30 wt %.

The model still predicts the M_S well when carbon is added to Fe-Mn or Fe-Mn-Si alloys. The results are shown in Fig. 4.9a. The model also works well on Fe-Mn-Ni, Fe-Mn-Ti and Fe-Mn-Low Cr alloys. Low Cr means that the alloy contains Cr less than 4 wt %.

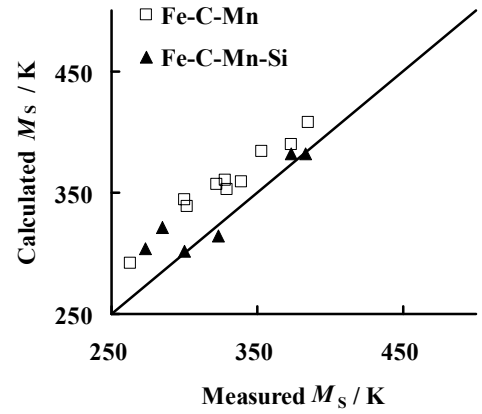

(a)

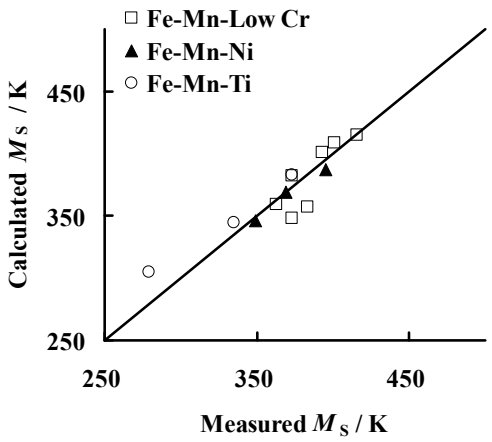

(b)

Fig. 4.9: ε-martensite start temperatures. (a) Fe-C-Mn and Fe-C-Mn-Si alloys. (b) Fe-Mn-Low Cr, Fe-Mn-Ni and Fe-Mn-Ti alloys.

Cobalt hardly affects M_S in literature data (Ishida and Nishizawa, 1974; Hamers and Wayman, 1991; Baruj *et al*., 1995; Jun *et al*., 1998;). However, cobalt decreases $|\Delta G^{\gamma\rightarrow\epsilon}|$, therefore depresses M_S in the present model. The results are shown in Fig. 4.10a. Other alloy systems of which predictions are poor are also shown in Fig. 4.10b. The data in Fig. 4.10b look substantial but all data are from 2 sources of literature. Data of 6 ternary alloy systems are all from Ishida and Nishizawa's work (1974) and Fe-Mn-Al-Si data are from Eskil and Kanca (2008).

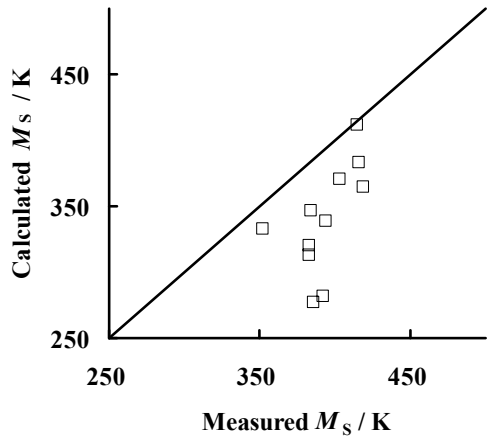

(a)

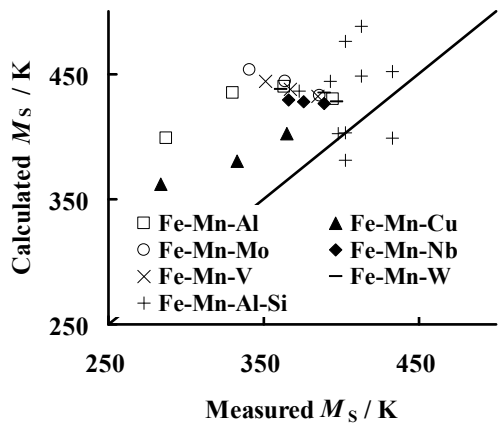

(b)

Fig. 4.10: Alloy systems of which prediction is poor. (a) Fe-Mn-Co alloys. (b) Other alloy systems.

Predictions of the model are good in some alloy systems, but it doesn't work well on certain types of alloy systems. Besides such alloy systems, there are systems where severe problems occur. There are large errors when the solute concentration is large as in the Fe-20Mn-7Cr-6Si wt % alloy. Fig. 4.11 illustrates all $\Delta G_{M_S}^{\gamma\rightarrow\epsilon}$ as a function of the measured transformation–start temperatures obtained from the literature.

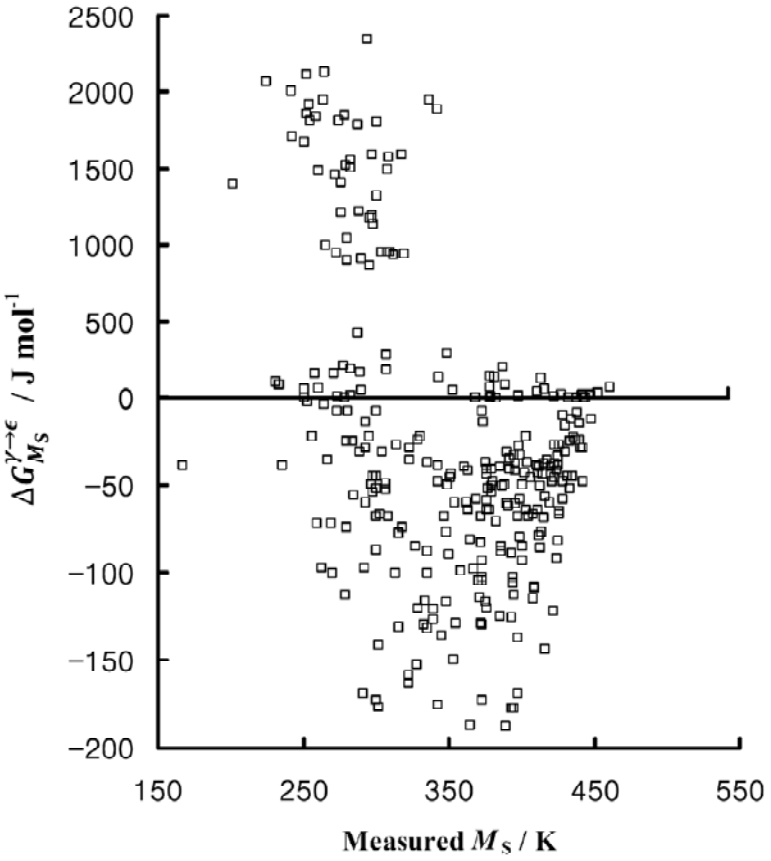

Fig. 4.11: The calculated free energy change accompanying the formation of ε-martensite at the measured M_S temperature. Notice that the scales above and below the abscissa are different. The samples for which $\Delta G_{M_S}^{\gamma\rightarrow\epsilon} \geq 0$ are generally those which have large total solute concentrations, for example, alloy 228: Fe-20Mn-5Ni-8Cr-5Si wt %.

The results are worrying in two respects; first, that the driving force for a large number of alloys is positive, i.e., it is thermodynamically impossible for ε to form even though it is actually observed, and secondly, even when $\Delta G_{M_S}^{\gamma\rightarrow\epsilon}$ is negative, its magnitude is in many cases very small and possibly insufficient to account for the strain energy of transformation.

There are two ways in which these results might be understood. The first is that the experimental measurements of M_S temperatures are faulty, but experimental work proved that uncertainties in dilatometric measurements of M_S are small even though the volume change is small. And a detailed examination of the original sources of information indicated that any error in M_S is much smaller than required to explain the sign and magnitude of the free energy change in cases where $\Delta G_{M_S}^{\gamma\rightarrow\epsilon} \gg 0$. The second and more likely explanation is that the database which forms the basis of the thermodynamic calculations is insufficiently populated to represent ε–martensite in concentrated alloys and at the relatively low temperatures involved. First principles calculations based on electron theory can be used to check this second explanation (Yang *et al.*, 2011).

The formation energies at 0 K and zero pressure were calculated to give $\Delta G^{\gamma\rightarrow\epsilon}$ as -5.57 kJ mol^{-1} and -3.49 kJ mol^{-1} for the transformation in pure iron and Fe-22Mn-4Si-8Cr wt % alloy respectively. The value for pure iron is consistent with -5.45 kJ mol^{-1} reported by Kaufman *et al*. (1963) for one atmosphere of pressure and 0 K. TCFE6 calculation gave large positive $\Delta G^{\gamma\rightarrow\epsilon}$ for such concentrated alloyed system. The calculation proves the need for better thermodynamic data for use in software such as Thermocalc or MTDATA.

4.3.3 Neural Network

The last strategy for the estimation of ε M_S is the neural network analysis, the most general method of regression, it is able to capture non–linear, non–periodic functions of immense complexity without bias on the form of the function. To create a network which is not too simple, nor so complex that is models the noise in

the information, the data were partitioned at random into approximately equal training and test sets. The former was used to create the models and the latter to test their ability to generalise. Once the appropriate level of complexity is achieved, the entire data can be used to retrain the network without changing its conFiguration. The results, having gone through these procedures, are illustrated in Fig. 4.12 and show that the optimised network performs well on the unseen test data.

It is possible now to illustrate the non–linear capability of the neural network, which is consistent with expectations from physical metallurgy but would not be captured by a linear regression equation. The Néel temperature T_N of austenite is raised almost linearly by the addition of manganese (Umebayashi and Ishikawa, 1966) and this has an enhanced effect on suppressing the ε martensite–start temperature if the latter is below T_N (Palumbo, 2008) as mentioned earlier. That this phenomenon is correctly represented by the neural network is illustrated in Fig. 4.13.

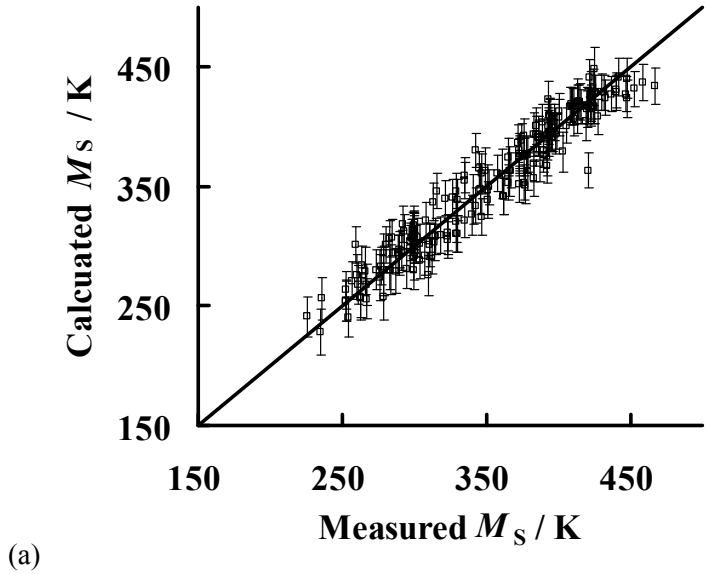

(a)

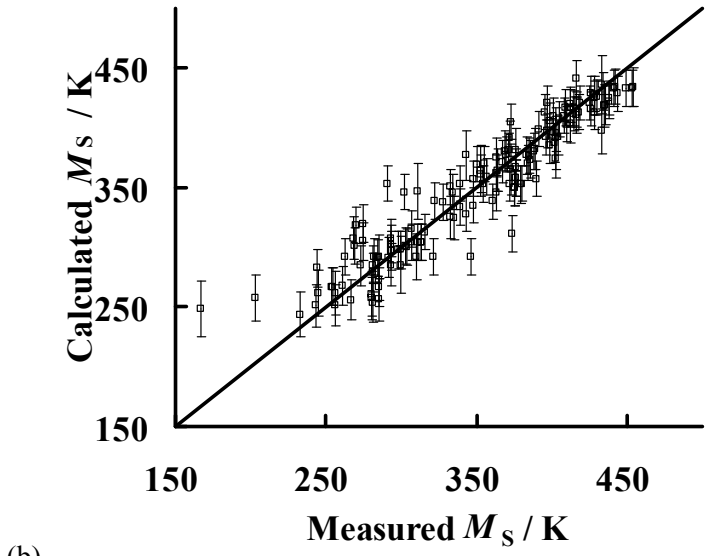

(b)

Fig. 4.12: Illustration of the fit achieved with a neural network of optimum complexity. The error bars represent ± 1σ modeling uncertainty. (a) Data used to create the network. (b) Unseen data used to test the network.

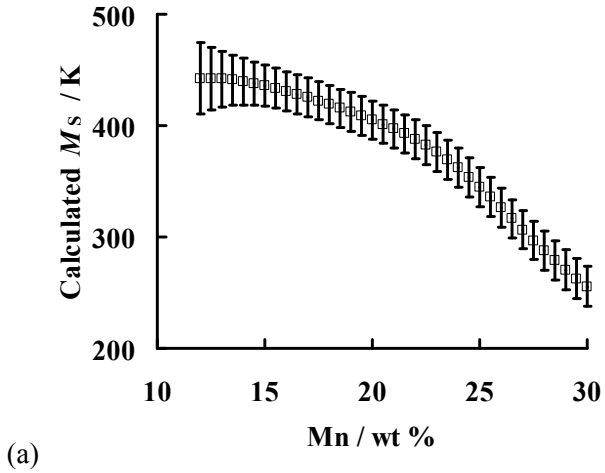

(a)

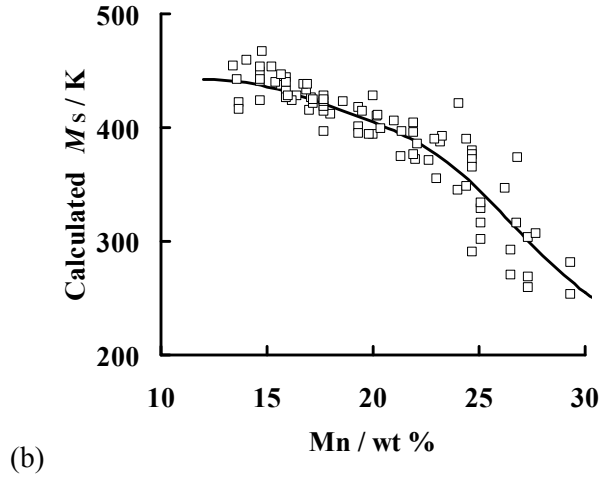

(b)

Fig. 4.13: Variation in the martensite-start temperature in Fe-Mn binary alloys as a function of the manganese concentration. (a) Calculated using neural network. (b) Measured values (Fig. 4.5), together with calculated curve from (a).

The silicon effect on ε-martensite start temperature is not monotonic (Georgiyeva *et al*., 1981; Donner *et al*., 1989) and hard to understand. Experimental work, neural network analysis and thermodymic model described previously, all predict the same trend. They are shown in Fig. 4.14. Basically M_S decreases as manganese or chrome increases. Silicon increases M_S up to middle silicon alloying

and depresses M_S at high silicon concentrations. Even critical driving force is assumed as constant for alloys containing the same manganese, M_S increase and decrease in same Mn alloy according to Si in thermodynamic calculations. Thermodynamic model is also successful to reproduce the trend of Si effect on ε M_S.

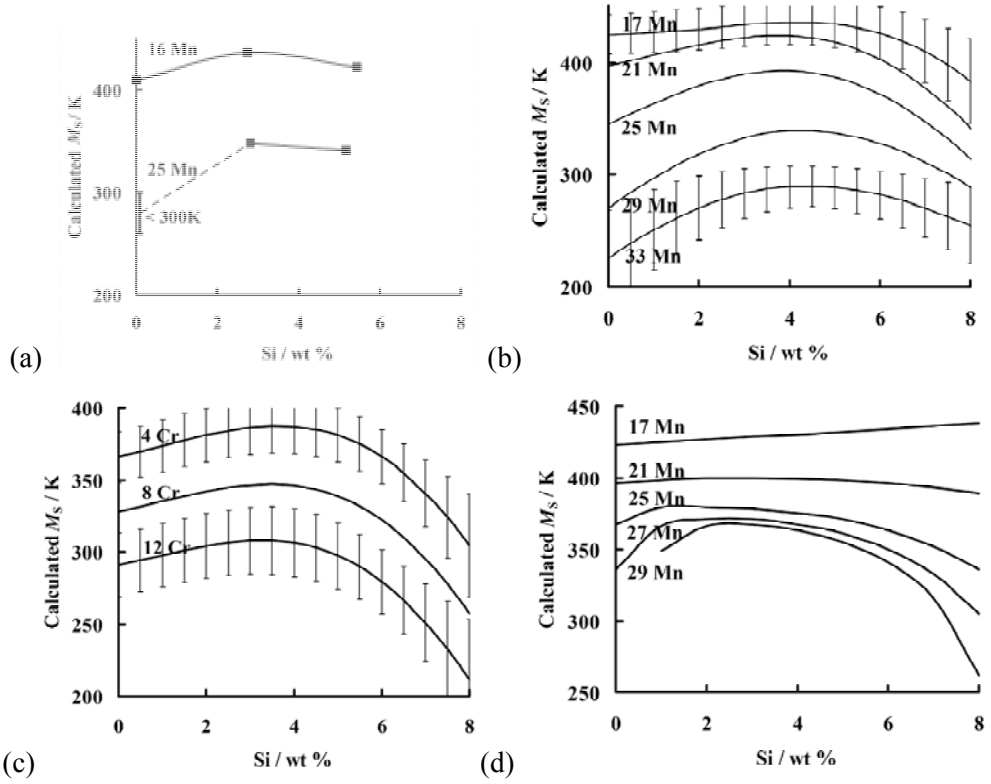

Fig. 4.14: Silicon effects on ε M_S. (a) New experimental data of Fe-Mn-Si alloys. Fe-25Mn-0Si wt % alloy' M_S is below room temperature. (b) Neural network prediction on Fe-Mn-Si alloys. (c) Neural network prediction on Fe-20Mn-Cr-Si wt % alloys. (d) Thermodynamic model's prediction described previously.

4.4 Summary

Several methods for prediction of ε M_S were investigated. An empirical linear equation was developed which provides rough method for the prediction. Even though the current thermodynamic database especially the hcp phase is faulty, the

assumption that the critical driving force for ε-martensite is a function of manganese led to a successful prediction of the M_S in alloy systems of Fe-Mn, Fe-Mn-Si, Fe-C-Mn, etc. Most alloys which have large concentration of solutes showed an impossibly large positive $\Delta G_{M_S}^{\gamma\rightarrow\epsilon}$ using the standard thermodynamic database. This cannot be explained by experimental uncertainties. First principle calculation proved that current thermodynamic database is not suitable for calculating such highly concentrated system's fcc→hcp transformation. Finally, neural network analysis was applied, and shown to be capable of predicting the transformation temperature for a wide range of compositions and complex phenomena. Some examples of the complex prediction ability have been illustrated. The neural network models, thermodynamic calculations and the full set of compiled data can be downloaded elsewhere.[*]

[*] http://www.msm.cam.ac.uk/map/steel/programs/epsilon.Ms.html
http://cml.postech.ac.kr/2011/epsilon.zip

Chapter 5: Design of Low-Carbon, Low-Temperature Bainite

5. 1 Introduction

The scale and extent of the microstructure obtained when austenite transforms into bainite is dependent directly on the fact that the atoms move in a disciplined fashion. This information has been exploited to develop unconventional alloys based on carbide free mixtures of bainitic ferrite and carbon enriched retained austenite. Examples include the austempered ductile cast irons (Dorazil *et al*., 1982; Moore *et al*., 1985), transformation induced plasticity assisted steels (Girault, 1999; Jacques, 2004; DeCooman, 2004), rail steels which do not rely on carbides for their properties (Zhang and Gu, 2007; Bhadeshia, 2008b), and recently, the hardest ever bainite (Caballero *et al*., 2002; Garcia-Mateo *et al*., 2003 a-c; 2004).

The low-temperature bainite is particularly fascinating in that it can be produced in bulk form, without the need for rapid heat treatment or mechanical processing, by transformation at low temperatures (typically 200 ℃), resulting in plates of ferrite which are remarkably thin (20–40 nm). This fine scale of the microstructure is largely responsible for hardnesses as high as 690 HV (Garcia-Mateo, 2003a). The very low transformation temperature is achieved primarily by increasing the carbon concentration of the steel to ~ 1 wt %. This might make the alloys difficult to weld because of the danger of forming untempered, brittle martensite in the heat affected zones of any joints. Coarse martensite is prone to fracture under the influence of small stresses, in which case it would compromise the structural integrity of the joint. For this reason, the vast majority of weldable steels have low carbon concentrations.

Since much of the strength of the bainite comes from its fine scale and not from dissolved carbon, it should be possible to reduce its concentration and instead to suppress the transformation temperature using substitutional solutes. One obvious requirement is that the B_S must be maintained above that for martensite M_S.

Yang and Bhadeshia (2008) investigated Fe - 0.1C - 2Mn - (4~6)Ni wt % alloys.

They showed that it is possible to depress the transformation start temperatures using a high concentration of substitutional alloys. However the transformation temperatures were not low enough, the gap between B_S and M_S was diminished at high solute concentrations. It also revealed another problem, formation of coalesced bainite which is detrimental to coalesced bainite. This chapter investigates another set of alloys to see the possibility of low-carbon, low-temperature bainite maintaining weldability and mechanical properties.

5.2 Alloy Design

The theory described in chapter 1 and MTDATA were used for calculating the transformation-start temperatures for several alloy systems (Okumura and Sourmail, 2004). Three alloys were chosen for investigation, they are shown in Table 5.1. The table also includes alloys (4Ni, 5Ni and 6Ni alloys) investigated in previous research (Yang, 2008) for comparison. Some calculation and measured data are shown in Table 5.2. The M_S temperature of 6Ni alloy was the lowest among 3 alloys at 270 ℃. However, the kinetics of transformation were very slow (3 months for completion) and caused the formation of coalesced bainite. The alloy A was designed to investigate the silicon effect on formation of coalesced bainite. Silicon is known to suppress carbide formation (Cooman, 2004), permitting carbon to remain in solution and increases the stability of the residual austenite. The idea is that presence of stabilised austenite films between bainite plates would prevent the coalescence process. The high concentration of manganese causes a banded structure (Yang, 2008), so its concentrations was reduced to 0.5 wt %. The carbon concentration was increased to compensate for the reduced manganese level in alloy B. The bainite transformation took 3 months to complete in the 6Ni alloy. Therefore cobalt was added to accelerate the reaction in alloy C.

Table 5.1: Chemical compositions of the alloys in wt %.

Designation	C	Mn	Ni	Si	Co
4Ni	0.13	2.3	4.0		
5Ni	0.13	2.3	5.0		
6Ni	0.20	2.5	6.7		
Target A	0.2	2	6	1.5	
Target B	0.3	0.5	6	1.5	
Target C	0.3	0.5	6	1.5	1
A	0.18	1.9	5.4	1.4	
B	0.23	0.5	5.6	1.4	
C	0.28	0.5	5.5	1.4	0.9

Table 5.2: Properties of the alloys. Incubation time means the calculated time required for initiating the bainite transformation. Long incubation time imply slow kinetics.

Alloy	Calculated			Measured		
	M_S / ℃	T'_0 / ℃	Incubation time / s	M_S / ℃	B_S / ℃	Time scale for bainite transformation
4Ni	360	525	62	373 ± 12	485	~1h
5Ni	350	505	100	372 ± 13	465	~1h
6Ni	280	445	760	272 ± 14	~300	~3 months
Target A	280	435	870			
Target B	290	445	330			
Target C	300	455	220			
A	300	465	360	259 ± 3	410	~10 h
B	320	475	130	324 ± 3	~500	~1h
C	320	475	110	295 ± 4	~480	~1h

5.3 Experimental

The alloy was made in a vacuum induction furnace; the ingot was reheated to 1200 ℃ for 1 h followed by hot rolling into 30 mm plate. The carbon concentration was analysed using a LECO instrument to a reproducibility of ± 0.0013 wt %, and the remaining elements using spark optical emission spectroscopy to a reproducibility of ± 0.003 wt %. Small blocks of the alloys were vacuum sealed in quartz tube and homogenised at 1200 ℃ for 2 days before each experiment.

A push rod BAHR DIL805 high speed dilatometer was used for investigating transformation behaviour. Cylindrical dilatometric samples of diameter 5 mm and length 10 mm were used. Dilatometer experiments were done in vacuum or argon atmosphere. The heating rate was 10 ℃ s^{-1}. The cooling rate was -10 ℃ s^{-1} for the alloy A and -30 ℃ s^{-1} for the alloy B and C because the former rate was not fast enough to avoid high temperature products. Austenitisation was done at 800 ℃ for 30 s for the alloy A and 900 ℃ for the alloys B and C. M_S temperature were measured by quenching experiments in dilatometer analysed using offset method (Yang and Bhadeshia, 2007).

Samples for optical microscopy were etched using nital 2 % or using a solution of 1 g sodium metabisulfite in 100 mL water mixed with 4 g of picric acid dissolved in 100 mL of water for 5-30 s (LePera, 1979). Hardness was measured 5 times using 2 or 10 kg load and averaged. X-ray diffraction specimens were ground using SiC paper and etched to remove the stress-affected surface. They were analysed using a BRUCKER D8 X-ray diffractometer, with step scanning at 0.15^{o} per minute using Cu K_{α} X-rays. Samples for transmission electron microscopy were prepared from 300 mm thick slit specimens which were then reduced in thickness from both sides using SiC paper to a thickness of 80 μm before punching out 3 mm discs. These foils were electropolished at room temperature, until perforation occurred, using a Tenupol-5 polisher set at 20-40 V. The electrolyte consisted of 8 % perchloric acid and 92 % acetic acid. The thin foils were examined in a Philips CM200 transmission electron microscope operated at 200 kV. Tensile tests were carried out

at room temperature. Tensile specimens 1 mm in thickness and 25 mm in gage length were tested on an Instron 5582 machine at a crosshead speed of 2 mm min^{-1} or on a Zwick / Roell Z100 machine with strain rate of 10^{-3}. A scanning electron microscope JEOL JSM-6610 was used for fractographic analysis with an operating voltage of 10-20 kV.

5.4 Alloy A

The transformation behaviours of the alloys were charaterised. The trend of the results was similar for alloy B and C, so they will be discussed separately. The results of isothermal experiments conducted on alloy A are shown in Fig. 5.1. The bainite fraction decreased as the temperature increased which can be well understood on the basis of the incomplete reaction phenomenon (Bhadeshia, 2001a). The Retained austenite fraction decreased as the bainite fraction decreased (Fig. 5.1b).

The microstructure of alloy A is bainite, martensite and some retained austenite. Bainite formed during the isothermal transformation and the blocky residual austenite transformed into martensite on subsequent cooling. Optical micrographs of Alloy A are shown in Fig. 5.2. The martensite fraction obtained at room temperature increases as the isothermal transformation temperature increased because of decreasing bainite fraction (Fig. 5.2c-f).

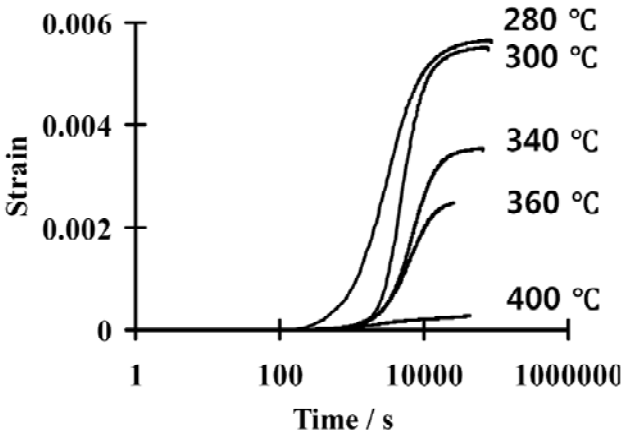

(a)

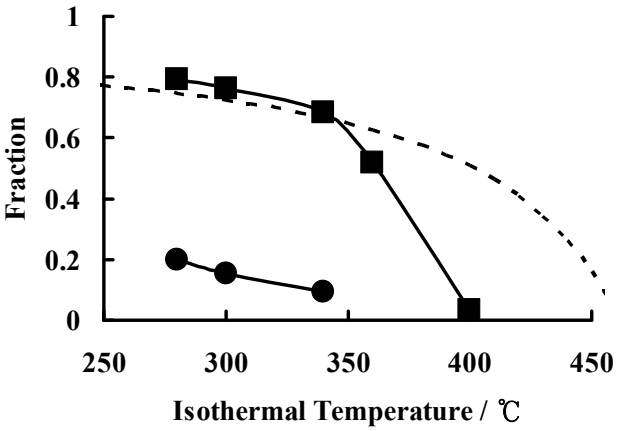

(b)

Fig. 5.1: (a) Dilatometric curves of isothermal experiments for the alloy A. (b) Measured bainite fraction (squares) and retained austenite (circles). Dashed line represents the calculated fraction of bainite predicted by lever rule with $T_0^{`}$ criterion.

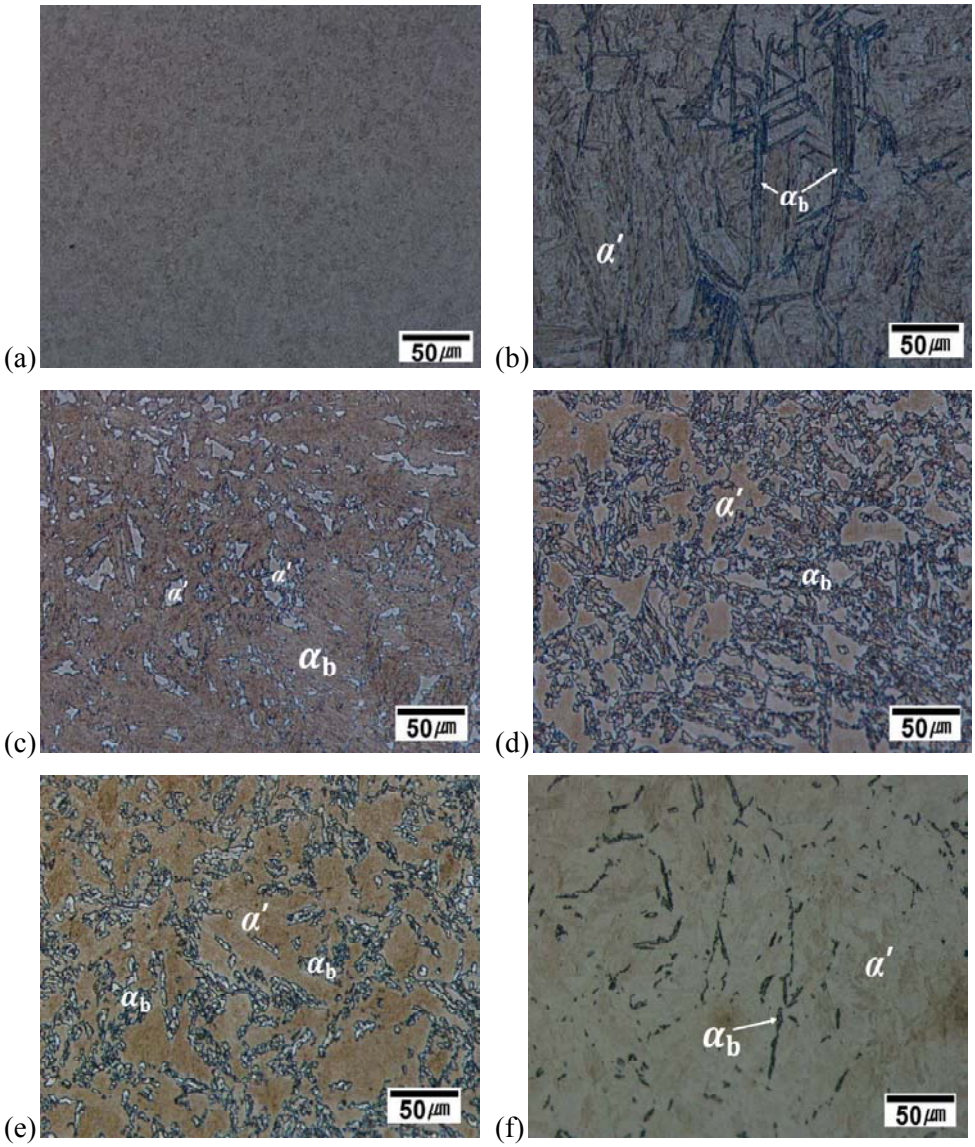

Fig. 5.2: Optical micrographs of the alloy A. (a) Quenched sample, fully martensitic. (b) Transformed at 300 ℃ for 0.5 h, partially transformed to bainite. (c) Transformed at 300 ℃ for 20 h. (d) Transformed at 340 ℃ (e) Transformed at 360 ℃, bainite fraction is decreasing (f) Transformed at 400 ℃, bainite fraction is small.

Dilatometric data and optical micrographs both indicate that bainite fraction decreases and martensite fraction increases with temperature. This can be confirmed again using hardness tests. Hardness increases as the temperature at which bainite is generated is increasing as shown in Fig. 5.3.

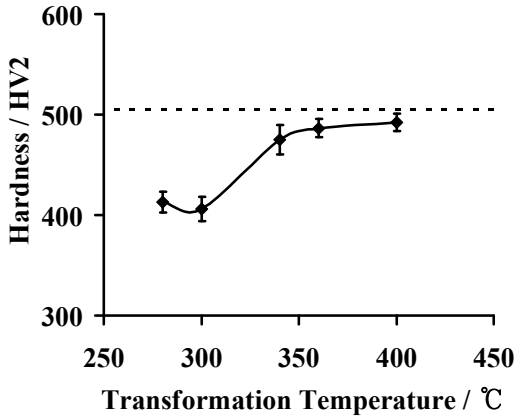

Fig. 5.3: Hardness of the alloy A. Dashed line represents the hardness of fully martensitic sample.

TEM micrographs of the alloy A are shown in Fig. 5.4. They show bainitic and martensitic regions. Bainitic regions consist of ferrite plates and retained austenite films. Coalesced bainite was not observed. Considering that the alloy of which composition is similar with alloy A without silicon contained coalesced bainite, silicon is clearly helping to prevent the formation of coalesced bainite by the mechanism described previously.

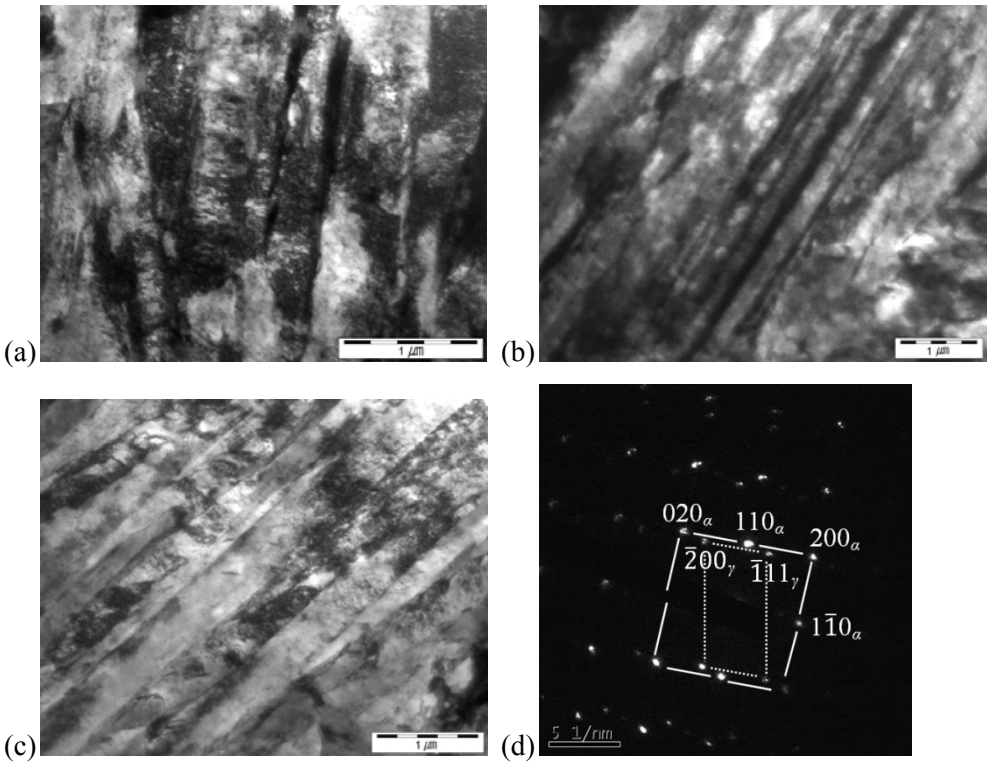

Fig. 5.4: TEM micrographs of alloy A transformed at 280 ℃. (a) and (b) show bainitic plates and retained austenite. (c) shows martensitic region. (d) diffraction pattern of the bainitic region, **B** = $[0\ 0\ 1]_\alpha = [0\ \bar{1}\ 1]_\gamma$

5.5 Alloys B and C

Isothermal dilatometric data of alloys B and C are shown in Fig. 5.5. The trends are similar with those observed for alloy A. The fraction of the isothermal products decreases as the temperature increases. However, the fraction does not reduce to 0 at high temperatures. The microstructures of alloy B are shown in Fig. 5.6. Blocky residual austenite after bainite transformation did not transform into martensite on cooling but was retained. And the fraction of the retained austenite islands increased as the transformation temperature was increased. Another difference of alloys B and C with the alloy A is the extent to which the fraction of bainite decreases as the temperature increases. The bainite fraction decreases much more rapidly for alloy A

as shown Fig. 5.1. The retained austenite islands were also revealed in the electron back scattered diffraction experiment (Fig. 5.7).

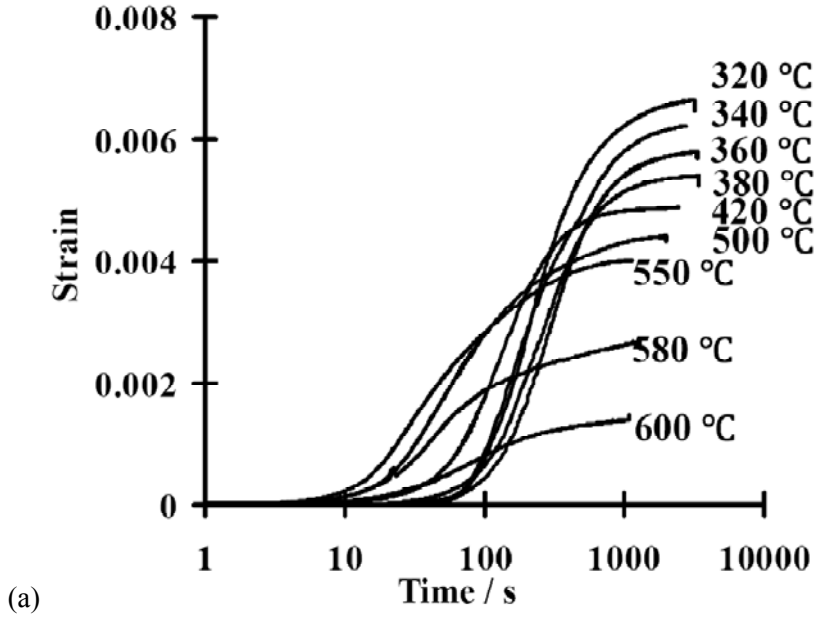

(a)

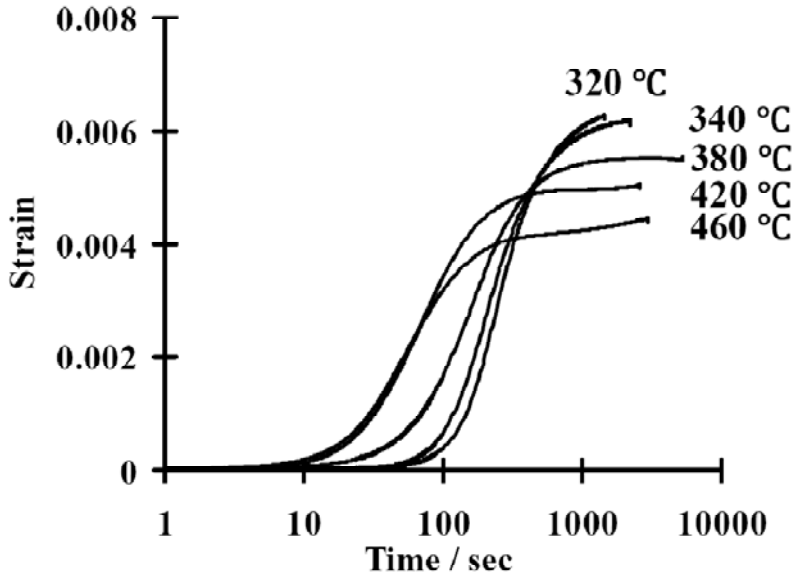

(b)

Fig. 5.5: Results for isothermal transformation experiments on alloys (a) B and (b) C.

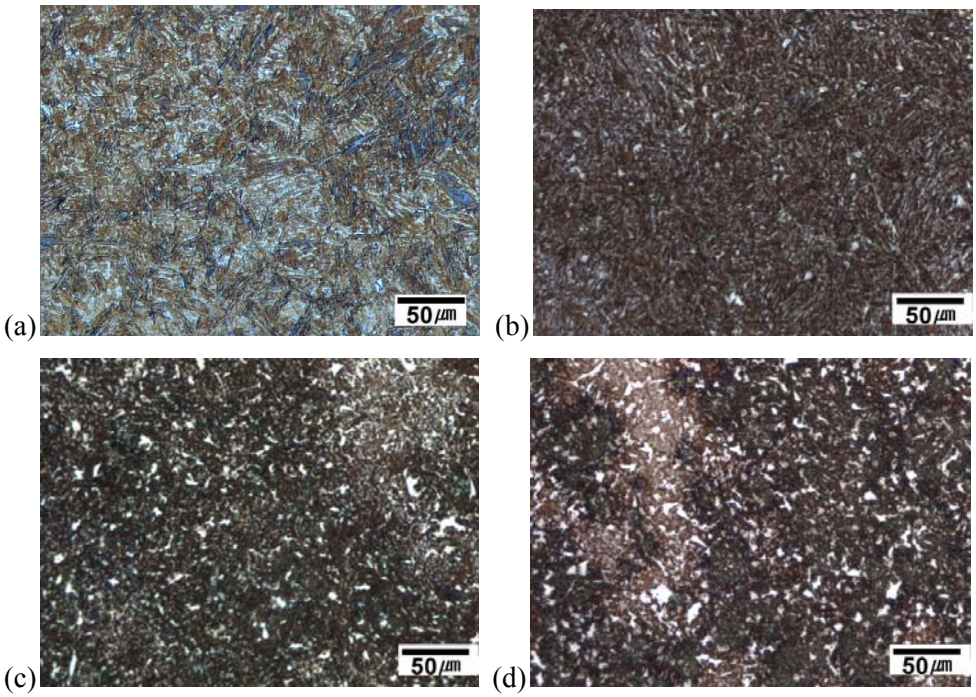

Fig 5.6: Optical micrographs of the alloy B. (a) quenched sample (b) transformed at 320 ℃ (c) 380 ℃ (d) 420 ℃. White austenite islands are seen.

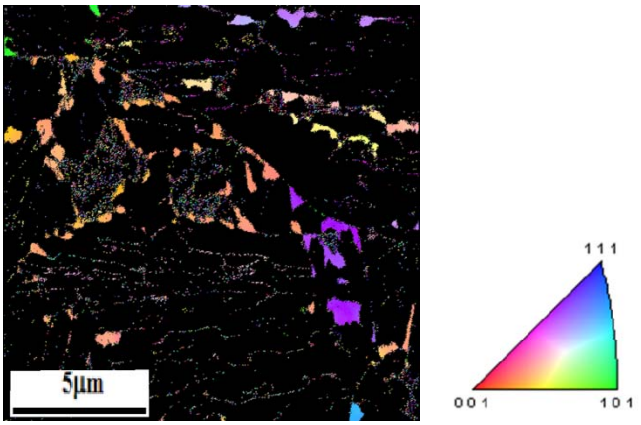

Fig. 5.7: Orientation map of retained austenite, alloy C transformed at 340 ℃. The groups of the retained austenite islands which have same orientations identified by the colour are shown.

Other transformation products besides bainite started to form as the transformation temperature was increased. Reconstructive ferrite started to form above 420 ℃ as shown in Fig. 5.8. The two C-curves in TTT diagram are separated perfectly in alloy A, but they overlap in alloys B and C.

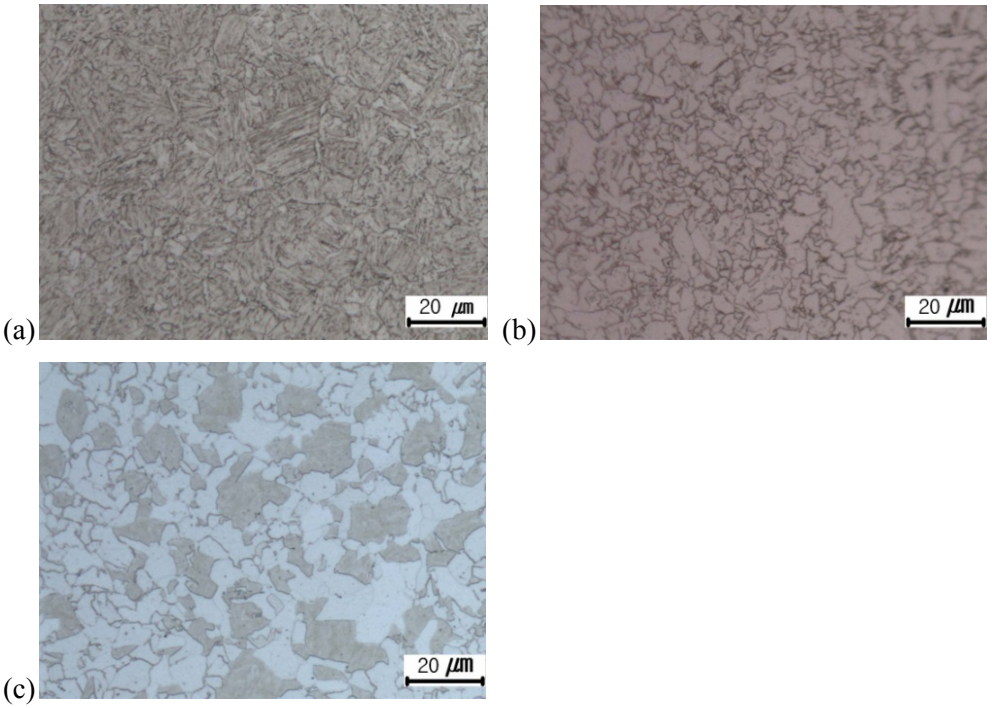

Fig. 5.8: Micrographs of the alloy B (a) transformed at 340 ℃, fully bainitic (b) 500 ℃, reconstructive ferrite are seen. (c) 580 ℃, mixture of martensite and reconstructive ferrite.

Hardness decreased as the temperature increased in bainitic transformation regions as shown Fig. 5.9, opposite trend of the alloy A. The reason comes from bainitic plate thickness and dislocation density because the difference in bainite fraction according to temperature is small. Hardness increased rapidly at higher temperatures for alloy B because of the large fraction of martensite in the final microstructure. TEM micrographs of the alloys B and C are shown in Fig. 5.10 showing bainitic plates with austenite films. The plates of them are as thin as about 200 nm.

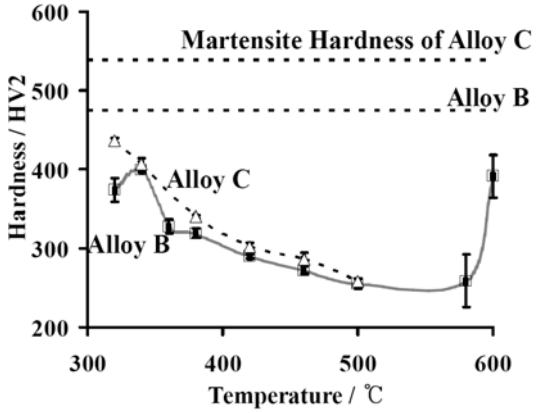

Fig. 5.9: Hardness data of the alloys B and C.

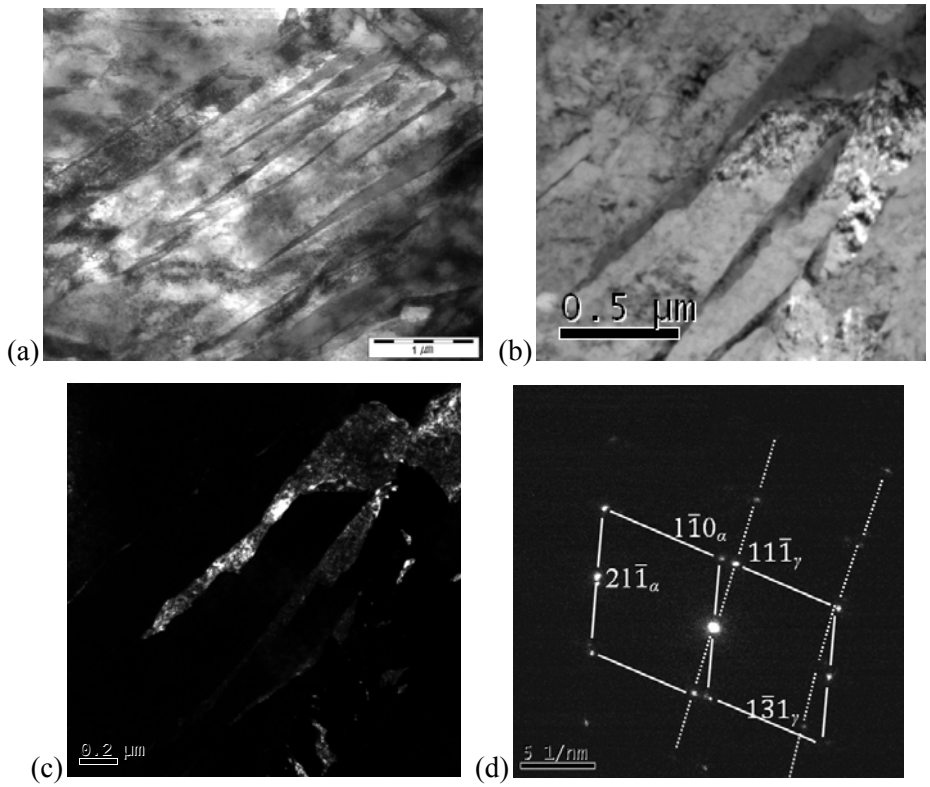

Fig. 5.10: TEM micrographs (a) alloy B, transformed at 320 ℃ (b) alloy B, 320 ℃ (c) retained austenite dark field image (d) corresponding diffraction pattern, **B** = $[113]_\alpha$=$[112]_\gamma$.

(e) 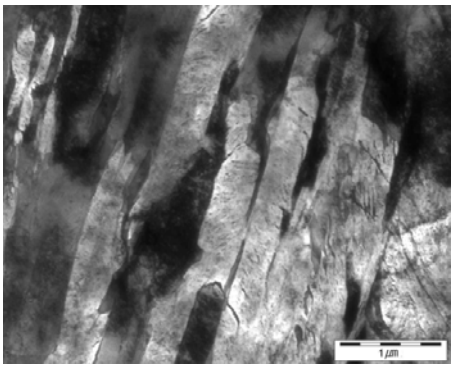 (f) 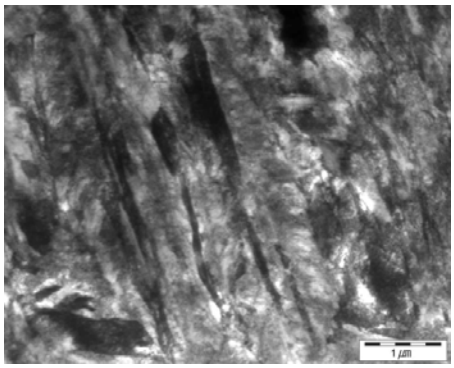

(g) 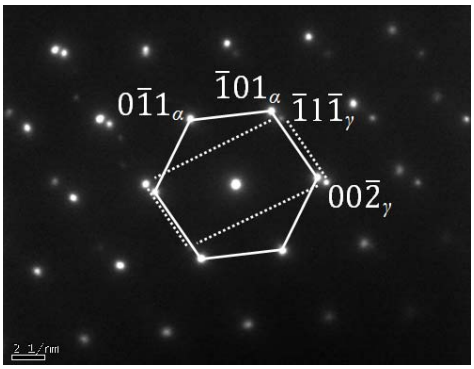

Fig. 5.10: (e) alloy C, 340 ℃ (f) alloy C, 320 ℃ (g) diffraction pattern of alloy C transformed at 320 ℃, $\mathbf{B} = [111]_\alpha = [110]_\gamma$

5.6 Parameters Affecting Bainite Transformation Kinetics

One of the key parameters in designing low temperature bainite is the rate of transformation. In some cases, it takes 3 months to complete the reaction (Yang, 2008). One of the affecting parameters is the prior austenite grain size. Alloy A has slow kinetics, so it was appropriate for investigation. The results are shown in Fig. 5.11. Prior austenite grain sizes were varied by altering the austenitisation temperature and the results show that a large grain size is helpful for the acceleration of the bainite transformation in spite of the decrease in grain boundary nucleation sites. This depends on the morphology of the bainite (Matsuzaki and Bhadeshia, 1995) as shown in Fig. 5.12. If the bainite sheaf grows until encounters obstacles such as a grain boundary or another bainite sheaf, a large grain leads to a

larger sheaf and is helpful for fast kinetics. This is similar with the reason why large grain sample has higher a M_S temperature. Fig. 5.11b shows that bainite sheaves grow until they meet obstacles.

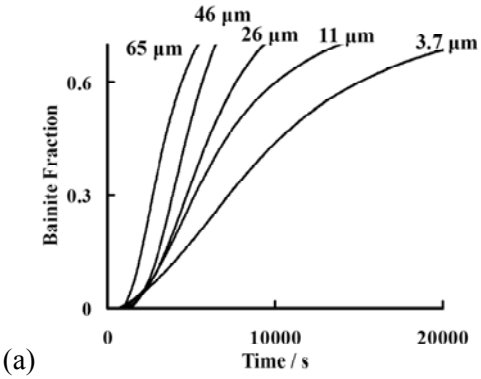

(a)

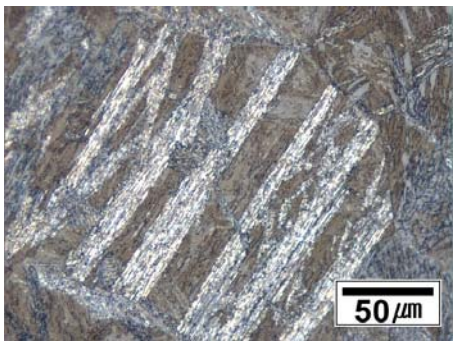

(b)

Fig. 5.11: Alloy A, transformed at 320 ℃, (a) Dilatometric data, austenite grain sizes are also shown. (b) Partially transformed sample showing that bainite sheaves grow until they meet obstacles for the alloy A. Sample austenitised at 1100 ℃, the largest prior austenite grain size.

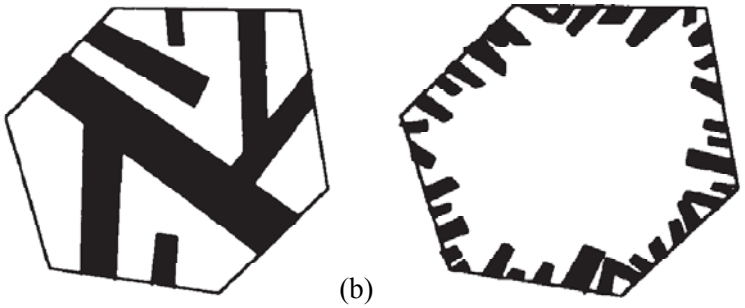
(a) (b)

Fig. 5.12: Schematic representation of bainite morphologies. (a) Sheaf grows within whole compartment. Sheaf size is more important than number of sheaf. Large grain size sample is fast in kinetics. (b) Sheaf size is independent of grain size. Nucleation is dominant parameter for the kinetics. Small austenite grain is favoured for fast kinetics (Matsuzaki and Bhadeshia, 1995).

It is known that cobalt increases the austenite decomposition driving force, therefore accelerates the transformation (Garcia-Mateo *et al*., 2003d). Alloy C was therefore expected to show faster kinetics than alloy B as shown Table 5.2. But actually the real composition of alloy C has more carbon than alloy B, which made the reaction relatively slow. Retardation by carbon was compensated with acceleration by cobalt. Therefore these two alloys showed similar kinetics as shown in Fig. 5.13.

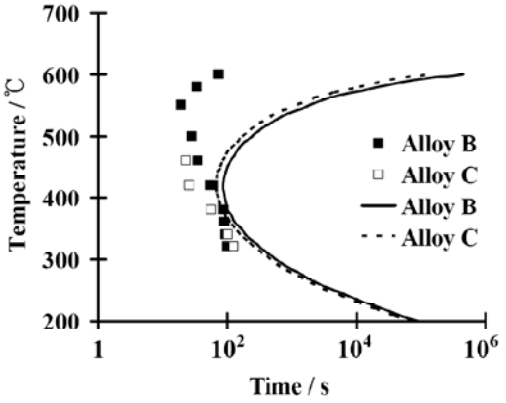

Fig. 5.13: Measured and calculated TTT diagrams of the alloy B and C. Points and lines represent measured and calculated data, respectively.

5.7 Incomplete Reaction

XRD data have been analysed to see carbon content in the austenite. Austenite peak positions were used to get lattice parameter data. Carbon content was calculated using the eq. 5.1 (Sherif, 2006).

$$a_\gamma(\text{nm}) = 0.35770 + 0.00065\text{C} + 0.0001\text{Mn} - 0.00002\text{Ni} + 0.00006\text{Cr} + 0.00056\text{N} + 0.00028\text{Al} - 0.00004\text{Co} + 0.00014\text{Cu} + 0.00053\text{Mo} + 0.00079\text{Nb} + 0.00032\text{Ti} + 0.00017\text{V} + 0.00057\text{W} \quad (5.1)$$

where concentrations are in at %. T_0' analysis are shown in the Fig. 5.14. The bainite reaction stops when the austenite carbon content reaches T_0' in the theory.

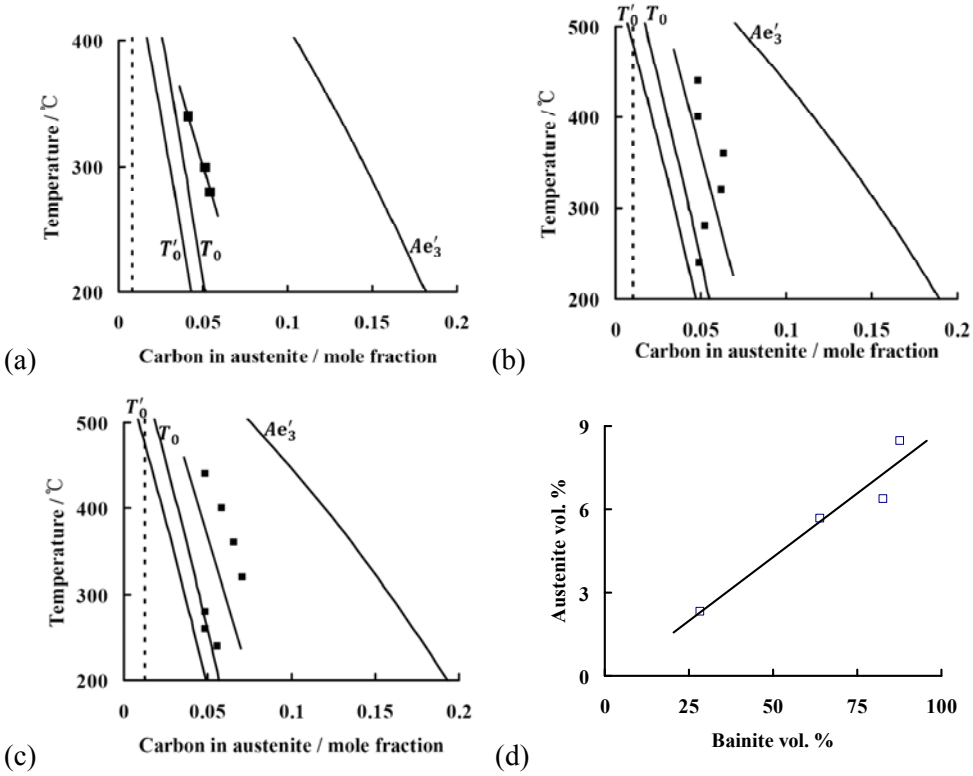

Fig. 5.14: T_0' analysis of (a) alloy A, (b) alloy B and (c) alloy C. Alloys carbon compositions are shown as dashed lines. (d) Austenite volume percent of alloy B as a function of bainite volume percent, partially transformed at 320 ℃.

Carbon concentrations of the retained austenite in this study are a little higher than the predictions. Retained austenite fractions were also measured. The austenite fraction was from 0.04 to 0.1 for the alloy B and C. Retained austenite fraction is one of the favourite parameters in mechanical properties as mentioned in chapter 1. One of the ways to increase austenite fraction is to transform partially into bainite to promote the retention of more residual austenite. However, the residual austenite transformed to martensite because the carbon enrichment was not enough to make stablise it to room temperatures. Only the austenite adjacent to bainite was retained, its fraction being proportional to that of bainite (Fig. 5.14d).

5.8 Mechanical Properties

Alloys were austenitised using a furnace and alloy A was put into the salt bath for 10 h. Alloy B and C were each heat treated for 1 h. Bainitic microstructures were obtained and they were machined as 1 mm thick, 25 mm gage length subsize sheet specimen (ASTM, 2000). Their mechanical properties are summarised in Fig. 5.15, not as good as those reported for high-carbon low-temperature bainite. An ultimate tensile strength of 1.6 GPa and 11 % total elongation was obtained. The strength increases as the transformation temperature is reduced because of the finer microstructure and the expected higher dislocation density at low temperatures. Tomita (1988) investigated AISI 4340 steel and showed that strength of a tempered mixture of lower bainite and martensite can exceed that of the martensite alone, and yet can be tougher. Therefore, some of the samples that transformed below M_S are also included in the Fig. 5.15. Bainite formed below M_S would be stronger due to finer structure, high dislocation densities and constraints from martensite. They were indeed stronger, however the improvements were not significant.

The total elongation of the alloy A transformed at 320 ℃ showed large scatter. It contains about 20 vol. % martensite, and the tensile specimens are thin. These two factors can in principle account for the large scatter in elongation. Their fractographs are shown in Fig. 5.16. If stress-concentrated regions are mostly occupied by martensite, it would cause brittle fracture. The distribution and orientation of the brittle martensite could change the elongation properties due to the small dimension of the specimens. Use of a large dimension specimen would eliminate these problems and give greater consistency in elongation values.

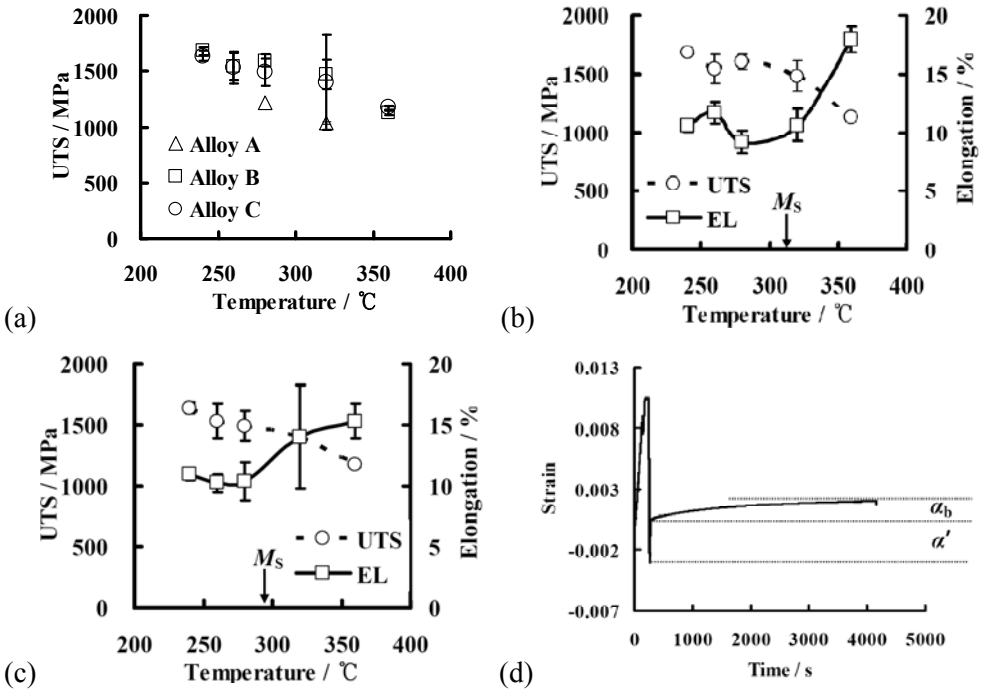

Fig. 5.15: Results of tensile tests. (a) Ultimate tensile strength of the alloys. UTS and total elongations of the (b) alloy B and (c) alloy C. (d) Dilatometric data for isothermal experiments below M_S.

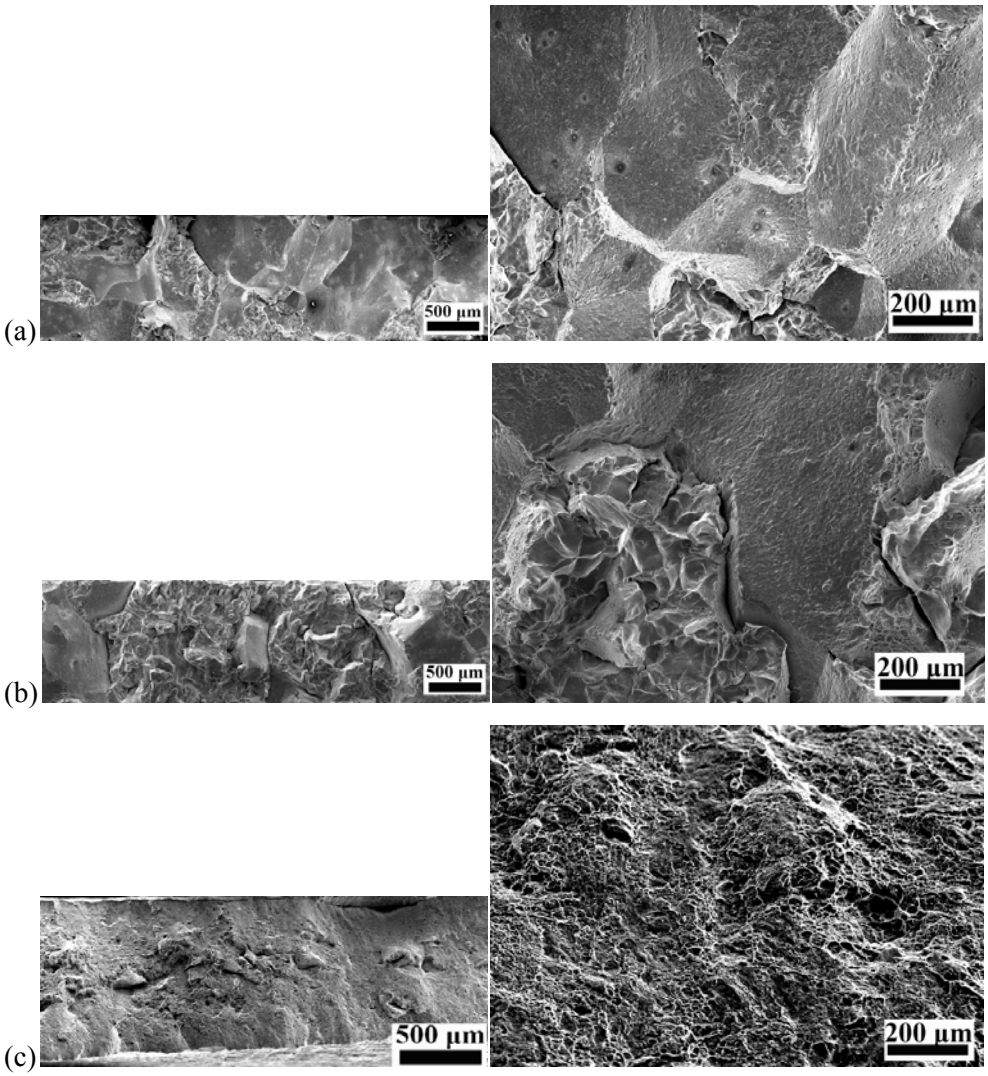

Fig. 5.16: Fractographs of the Alloy A transformed at 320 ℃, total elongation (a) 4 % specimen (b) 10 % (c) 16 %. Same alloy and heat-treatment, but large scatter in elongation.

5.9 Summary

Low-temperature bainite has limits in wide application due to poor weldability. The work presented in this chapter aimed to reduce the carbon content maintaining the mechanical properties. Carbon has been replaced by a higher concentration of

substitutional alloying elements to depress the transformation-start temperatures.

Several problems were predicted for design low-carbon, low-temperature bainite. One of them is the merge of M_S and B_S. B_S decreases more steeply than M_S as substitutional alloying elements increase, B_S can be depressed even below M_S. This particular issue had been predicted (Bhadeshia, 2005c) but not verified experimentally. Another problem is the coalescence of bainite. Due to the low temperatures where bainite forms, coalesced bainite can form. Coalesced bainite eliminates the advantage of fine structure, causes a decrease in strength and elongation. Another problem is the fraction of retained austenite. Retained austenite is helpful for mechanical properties in many respects for low-temperature bainite. Retained austenite in bainite is stabilised with help of carbon partitioning, but the low-carbon concentration of the alloys results in a somewhat smaller fraction of retained austenite.

Three alloys were studied to see weather all of the problems can be solved. The merging of M_S and B_S can be avoided utilising proper concentration of substitutional elements alloying, it was possible to get a predominantly bainitic microstructure. The silicon effect on coalesced bainite has been investigated. Coalesced bainite didn't form in the silicon added steel. Silicon stabilised the austenite which can act as a barrier in the coalescence process. It was possible to depress the transformation temperatures to as low as 280 ℃. However, UTS about 1 GPa and elongation about 10 % were obtained which can easily obtained using ordinary alloys and processes. The reason comes from the fraction of retained austenite. Fractions of retained austenite of the alloys are less than 0.1, similar with the value where austenite loses percolation (Bhadeshia, 2008). The Lack of significant retained austenite resulted in poor ductilities.

Slow kinetics is a potential problem in designing low-carbon, low-temperature bainite. Therefore some factors affecting bainite transformation have been also investigated. Large prior austenite grain size is helpful for rapid transformation in case of the morphologies of the alloys studied. The study also indirectly showed

that cobalt alloying accelerates the bainite transformation.

A large concentration of substitutional solutes was applied to depress the transformation temperatures, and it was possible to get bainite at temperatures as low as 280 ℃ with applicable kinetics. Nanostructured bainite was obtained without coalesced bainite, but it was not possible to get promising mechanical properties.

Chapter 6: Conclusions

One of the most exciting developments in very strong steels has been the so-called “superbainite”, but its carbon concentration, which is about 1 wt%, limits its wider applications because the material cannot be welded. There is a clear need to achieve the same structure and properties but with a much reduced carbon concentration.

The superbainitic steel relies on a suppression of transformation temperatures in order to achieve the incredibly fine structure which renders its properties. However, the suppression can in some circumstances also reduces the gap between the B_S and M_S temperatures. The characterization of the temperatures therefore requires precision. It was discovered at an early stage of the work that there is no objective method of determining the temperatures using dilatometry. In other words, investigators presented with the same dilatometric data may reach different conclusions regarding the onset temperature. Therefore, a new method (offset method) was developed during related work and applied in this research.

One of the constraints in design of low-temperature bainite is the onset of martensite. One of the ways to vary M_S independently of alloy content is the prior austenite grain size. Therefore a theory has been developed to express the dependence of the M_S temperature on the grain size and in order to gain insight into the mechanisms involved. In doing this, M_S was defined as a temperature specific fraction of martensite forms (e.g., 1 vol. % in offset method). The number of martensite plates to reach the specified, detectable fraction of martensite, depends on grain size because the plate size is proportional to grain size. It was shown that number of activated nuclei is the same regardless of grain, which exponentially increases as the temperature decreases. A large grain sample needs a smaller number of plates to reach the detectable fraction and hence results in a high M_S. The theory was verified by comparison with wide range of literature data including lath,

plate and hcp martensite. An interesting outcome is that a fundamental value of the start-temperature is defined for the case when the austenite grain size is infinite.

There should be difference in initial number of potential nuclei according to grain size. The effect of initial number diminishes as autocatalysis dominates the kinetics like previous paragraph. This was revealed in the analysis of grain size effect on martensite kinetics. The analysis showed that martensite transformation rate rapidly increases up to f = 0.1~0.2 then smoothly decreases. Small grain sized samples show rapid kinetics at the earlier stage with the help of the larger number of initial nucleation sites, but the differences in the kinetics of transformation diminish with large grain sized samples at the later stages of transformation.

The accumulated knowledge of body-centered cubic martensite was applied to hexagonal close-packed martensite in steels. It rapidly became clear that there are problems with this kind of martensite because the depth of published research is weak when compared with the ordinary marensite. To ensure that the difficulties with epsilon martensite are not due to inaccurate experiments, some verification experiments were done using three different experimental alloys. These confirmed that the temperatures can be measured accurately.

Three different approaches were investigated for estimating ε martensite-start temperature with data from the published literature. Linear empirical equation was developed for convenient and easy application. Predictions based on thermodynamic calculations were possible for some extent. But analysis revealed that the current thermodynamic database simply is not suitable for describing in $\gamma \rightarrow \varepsilon$ transformation, especially for highly concentrated ferrous alloys. The fact that it is the thermodynamic data that are problematic was confirmed using first-principles calculations. Given these difficulties, a neural network model for predicting ε M_S was developed. The model estimates M_S well, and is suitable for understanding complex trends in experimental results. It is found the just like ordinary martensite, the austenite grain size effect manifests with epsilon and can be represented using the same theory.

Three alloys were designed, manufactured and investigated to evaluate the validity of low-carbon version of low-temperature bainite. Several problems such as low transformation temperature, merge of B_S into M_S, presence of coalesced bainite and slow kinetics could be solved. However, small fraction of retained austenite coming from low-carbon concentration of initial alloy could not be avoided. That resulted in ordinary mechanical properties.

There is potential way to develop low-carbon, low-temperature bainite. Two step heat-treatment might show promising properties. Process consists of full austenitisation and two isothermal heat-treatments below B_S. First isothermal treatments can be done at relatively high temperatures. The fraction of bainite and carbon concentration of residual austenite can be controlled because they are determined by $T_0^{`}$ criteria. Residual austenite then transformed to bainite in second heat-treatment at low temperature. The principle is similar with TRIP aided steel. But the allotriomorphic ferrite is replaced by high-temperature bainite, and austempering is done at low temperatures.

Appendix: Neural Network Predictor

The neural network predictor for the prediction of ε martensite-start temperatures is available in
http://www.msm.ac.uk/map/steel/programs/epsilon.Ms.html

Program MAP_NEURAL_EPSILON_M_S

1. Provenance of Source Code

Hong-Seok Yang
Computational Metallurgy Laboratory,
Graduate Institute of Ferrous Metallurgy (GIFT),
Pohang University of Science and Technology (POSTECH),
Pohang, Republic of Korea
Added to MAP: January 2011

2. Purpose

Prediction of the epsilon martensite-start temperature as a function of chemical composition

3. Specification

Language: C

Product form: Source code / Executable files

Operating System: Linux / Window

4. Description

MAP_NEURAL_EPSILON_M_S contains programs which enable the user to predict the epsilon martensite-start temperature as a function of chemical composition. The

neural network model was made based on literature data using Models Manager, Neuromat Ltd. This program predicts the ε M_S of the alloys using the neural network model.

MINMAX

A text file containing the minimum and maximum limits of each input and output variable

test.dat

An input text file containing the input variables used for predictions. Each column represents C, Mn, Ni, Cr, Al, Si, Mo, Co, Cu, Nb, Ti, V and W in wt %, respectively.

model.gen

This is a unix command file. It can be excuted by typing **csh model.gen** at the command prompt.

MODEL.exe

This is executable program for the PC correspond to the unix command file.

Result

An output text file. Each column represents (M_S), (Uncertainty), (M_S-Uncertainty) and (M_S+Uncertainty) in K respectively.

5. References

H.-S. Yang, J. H. Jang, H. K. D. H. Bhadeshia and D. W. Suh. Critical Assessment: Martensite-Start Temperature for the $\varepsilon \rightarrow \gamma$ Transformation, will be published

References

Acet, A., Schneider, T., Gehrmann, B. and Wassermann, E. F.: The magnetic aspects of the $\gamma \rightarrow \alpha$ and $\gamma \rightarrow \varepsilon$ martensitic transformations in Fe-Mn alloys. *Journal de Physique Colloque*, Vol. 5 (1995) C8 pp. 379-384

Ali, A. and Bhadeshia, H. K. D. H.: Aspects of the nucleation of Widmanstätten ferrite, *Materials Science and Technology*, Vol. 6 (1990) pp. 781-784

Andersson, M. and Ågren, J.: Effect of prestraining and training on the $\gamma \rightarrow \varepsilon$ transformation in Fe-Mn-Si alloys. *Journal de Physique Colloque*, Vol. 5 (1995) C8 pp. 457-462

Ankara, O. A., Sastri, A. S. and West, D. R. F.: Some effects of austenitizining condition on martensite formation in an iron-20% nickel alloy. JISI, Vol. 204 (1966) pp. 509-511

Ansell, G. S., Brofman, P. J., Nichol, T. J. and Judd, G.: Effect of austenite strength on the transformation to martensite in Fe-Ni and Fe-Ni-C alloys, in G. B. Olson, M. Cohen (Eds.), International Conference on Martensitic Transformations ICOMAT'79 (1979) pp. 350-355

Andrews, K. W.: Empirical formulae for the calculation of some transformation temperatures. *Journal of Iron and Steel Research International*, Vol. 203 (1965) pp. 721-727

ASTM E 8M-00: Standard test methods for tension testing of metallic materials (2000)

Baik, Seung-Han, Kim, Jung-Chul, Jee, Kwang-Koo, Shin, Myung-Chul and Choi, Chong-Sool: Transformation behavior and damping capacity in Fe-17%Mn-X%C-Y%Ti alloy. *ISIJ International* Vol. 37 (1997) pp. 519-522

Baruj, A., Cotes, S., Sade, M. and Guillermet, A. Fernández: Coupling binary and ternary information in assessing the fcc/hcp relative phase stability and martensitic transformation in Fe-Mn-Co and Fe-Mn-Si alloys. *Journal de Physique Colloque*, Vol. 5 (1995) C8 pp. 373-378

Bhadeshia, H. K. D. H.: The bainite transformation in a silicon steel. *Metallurgical Trnasactions A*, Vol. 10A (1979) pp. 895-907

Bhadeshia, H. K. D. H.: Driving force for martensitic transformation. *Metal Science*, (1981a) pp. 175-177

Bhadeshia, H. K. D. H.: Thermodynamic extrapolation and martensite-start temperature of substitutionally alloyed steels. *Metal Science*. (1981b) pp. 178-180

Bhadeshia, H. K. D. H.: A rationalisation of shear transformation in steels, *Acta Metallurgica*, Vol. 29 (1981c) pp. 1117-1130

Bhadeshia, H. K. D. H. and Waugh, A. R.: Bainite: An atom-probe study of the incomplete reaction phenomenon. *Acta Metallurgica.*, Vol. 30 (1982) pp. 775-784

Bhadeshia, H. K. D. H., David, S. A., Vitek, J. M. and Reed, R. W.: Stress-induced transformation to bainite in a Fe-Cr-Mo-C pressure vessel steel. *Materials Science and Technology*, Vol. 7 (1991) pp. 686-698

Bhadeshia, H. K. D. H.: New bainitic steels by design, *Modelling and simulation for materials design*, National Research Institute for Metals, Japan, (1998) pp. 227-232

Bhadeshia, H. K. D. H.: Bainite in steels 2nd edition. (2001a) IOM Communications Ltd

Bhadeshia, H. K. D. H.: Worked examples in the geometry of crystals 2nd edition. (2001b) Institute of Metals

Bhadeshia, H. K. D. H.: Large Chunks of Very Strong Steel, *Millenium Steel,* Vol. 5 (2004) pp. 25-28

Bhadeshia, H. K. D. H.: Hard Bainite, *Solid→Solid Phase Transformation in Inorganic Materials*, Vol. 1 (2005a) pp. 469-484

Bhadeshia, H. K. D. H.: High performance bainitic steels, *Materials Science Forum*, 500-501 (2005b) pp. 63-74

Bhadeshia, H. K. D. H.: Hard bainite. *Solid→Solid Phase Transformations in Inorganic Materials*, Vol. 1 (2005c) pp. 469-484

Bhadeshia, H. K. D. H.: Bainitic Bulk-Nanocrystalline steel, *The 3rd international Conference on Advanced Structural Steels*, (2006)

Bhadeshia, H. K. D. H. and Honeycombe, R. W. K.: Steels 3rd edition. (2006) Butterworth-Heinemann

Bhadeshia, H. K. D. H.: The nature, mechanism and properties of strong bainite, *Proceedings of the 1st International Symposium on Steel Science (IS3-2007)*, Iron and Steel Society of Japan (2007)

Bhadeshia, H. K. D. H.: Properties of fine-grained steels generated by displacive transformation. *Materials Science Engineering A*, Vol. 481-482 (2008a) pp. 36-29

Bhadeshia, H. K. D. H.: Steels for rails, novel. *Encyclopedia of Materials: Science and Technology*. (2008b) pp. 1-7

Bhadeshia, H. K. D. H.: Neural networks and information in materials science. *Statistical Analysis and Data Mining*, Vol. 1 (2009) pp. 296-305

Bogachev, I. N. and Malinov, L. S.: Influence of chromium and nickel on the $\gamma \leftrightarrow \varepsilon$ transformations in a ferro-manganese alloy. *Physics of Metals and Metallography*, Vol. 14 (1962) pp. 828-833

Bogachev, I. N., Yegolayev, V. F., Zvigintseva, G. Ye. and Zhuravel, L. V.: Effect of alloying on austenite imperfection and tendency of an iron-manganese alloy to $\gamma \rightarrow \varepsilon$ transformation. *Physics of Metals and Metallography*, Vol. 28 (1969) pp. 885-888

Bohemen, S. M. C. van, Santofimia, M. J. and Sietsma, J.: Experimental evidence for bainite formation below M_S in Fe-0.66C. *Scripta Materialia*, Vol. 58 (2008) pp.488-491

Bohemen, S. M. C. van and Sietsma, J.: Effect of composition on kinetics of athermal martensite formation in plain carbon steels. *Materials Science and Technology*, Vol. 25 (2009) pp. 1009-1012

Bokros, J. C. and Parker, E. R.: The mechanism of the martensite burst transformation in Fe-Ni single crystals. *Acta Matallurgica*, Vol. 11 (1963) pp. 1291-1301

Borgenstam, A., Hillert, M. and Ågren J.: Metallographic evidence of carbon diffusion in the growth of bainite. Acta Materialia, Vol. 57 (2009) pp. 3242-3252

Bouraoui, T., Neste, A. van and Dubois, B.: Comparative effects of thermal treatments on the shape memory phenomenon of Fe-Mn-Si and Fe-Mn-Cr-Ni-Si steels. *Journal de Physique Colloque*, Vol. 5 (1995) C8 pp. 403-408

Bowles, J. S. and Mackenzie, J. K.: The crystallography of martensite transformations I. *Acta Metallurgica*, Vol. 2 (1954a) pp. 129-137

Bowles, J. S. and Mackenzie, J. K.: The crystallography of martensite transformations III. Face-centerd cubic to body-centered tetragonal transformations. *Acta Metallurgica*, Vol. 2 (1954b) pp. 224-234

Brofman, P. J. and Ansell, G. S.: On the effect of fine grain size on the M_S temperature in Fe-27Ni-0.025C alloys. *Metallurgical Transactions A*. Vol. 14A (1983) pp. 1929-1931

Brooks, J. W., Loretto, M. H. and Smallman, R. E.: In situ observations of martensite formation in stainless steel. *Acta Metallurgica*, Vol. 27 (1979a) pp. 1829-1838

Brooks, J. W., Loretto, M. H. and Smallman, R. E.: Direct observations of martensite nuclei in stainless steel. *Acta Metallurgica*, Vol. 27 (1979b) pp. 1839-1847

Caballero, F. G., Bhadeshia, H. K. D. H., Mawella, K. J. A., Jones, D. G. and Brown, P.: Very strong low temperature bainite. *Materials science and technology*, Vol. 18 (2002) pp. 279-284

Caballero, F. G. and Bhadeshia, H. K. D. H.: Very strong bainite. *Current Opinion in Solid State and Materials Science*, Vol. 8 (2005) pp. 251-257

Caballero, F. G., Miller, M. K., Babu, S. S. and Garcia-Mateo, C.: Atomic scale observations of bainite transformation in a high carbon high silicon steel. *Acta Materialia*, Vol. 55 (2007) pp. 381-390

Caballero, F. G., Garcia-Mateo, C., Santofimia, M. J., Miller, M. K. and Garcia de Andrés, C.: New experimental evidence on the incomplete transformation phenomenon in steel. *Acta Materialia*, Vol. 57 (2009) pp. 8-17

Cao, W., Krumhansl, J. A. and Gooding, R. J.: Defect-induced heterogeneous transformations and thermal growth in athermal martensite. *Physical Review B*, Vol. 41 (1990) pp.11319-11327

Caballero, F. G., Mateo, C. G., Chao, J and Santofimia, M. J.: Effects of morphology and stability of retained austenite on the ductility of TRIP-aided bainitic steels. *ISIJ International*, Vol. 48 (2008) pp. 1256-1262

Capdevila, C., Caballero, F. G. and Garcĭa de Andrés: Analysis of effect of alloying elements on martensite start temperature of steels. *Materials Science and Technology*, Vol. 19 (2003) pp. 581-586

Caenegem, N. van, Duprez, L., Verbeken, K., Segers, D. and Houbaert, Y.: Stresses related to the shape memory effect in Fe-Mn-Si-based shape memory alloys. *Materials Science and Engineering A.* Vol. 481-482 (2008) pp. 183-189

Chatterjee, S. and Bhadeshia, H. K. D. H.: TRIP-assisted steels: cracking of high carbon martensite. *Materials Science and Technology*, Vol. 22 (2006) pp. 645–649.

Chen, S., Chung, C. Y., Yan, C., Hsu, T. Y.: Effect of f.c.c. antiferromagnetism on martensitic transformation in Fe-Mn-Si based alloys. *Materials Science and Engineering A*, Vol. 264 (1999) pp. 262-268

Christian, J. W.: Thermodynamics and kinetics of martensite. G. B. Olson, M. Cohen (Eds.), International Conference on Martensitic Transformations ICOMAT'79 (1979) pp. 220-234

Christian, J. W.: The theory of transformations in metals and alloys, part II. Elsevier Science Ltd. (2002) pp. 961-1113

Cool, T. and Bhadeshia, H. K. D. H.: Prediction of martensite start temperature of power plant steels. *Materials Science and Technology*, Vol. 12 (1996) pp. 40-44

Cooman, B. C. De: Structure-properties relationship in TRIP steels containing carbide-free bainite. *Current Opinion in Solid State materials Science*, Vol. 8 (2004) pp. 285-303

Cotes, C., Sade, M. and Guillermet, A. Fernández: Fcc/hcp martensitic transformation in the Fe-Mn system: Experimental study and Thermodynamic analysis of phase stability. *Metallurgical and Materials Transactions A*, Vol. 26 (1995) pp. 1957-1969

Cotes, C., Sade, M. and Guillermet, A. Fernández: Phase stability and fcc/hcp martensitic transformation in Fe-Mn-Si alloys Part I. Experimental study and systematics of the M_S and A_S temperatures. *Journal of Alloys and Compounds*, Vol. 278 (1998) pp. 231- 238

Czichos, H.: Adolf martens and the research on martensite. *European Symposium on Martensitic Transformation*, (1989) 3-14

Dai, Q. X., Cheng, X. N., Zhao, Y. T., Luo, X. M. and Yuan, Z. Z.: Design of martensite transformation temperature by calculation for austenitic steels. *Materials Characterization,* Vol. 52 (2004) pp. 349-354

Dehoff, R. T. and Rhines, F. N.: Quantitative microscopy, McGraw Hill, New York (1968)

Dogan, A. and Ozer, T.: Determination of martensite transformation temperatures associated with Fe-Mn-Si-Ni-Cr-Ce-Ti-N shape memory alloys. *Canadian Metallurgical Quarterly*, Vol. 44 (2005) pp. 555-562

Donner, P., Hornbogen, E. and Sade, M.: Shape memory effects in melt spun Fe-Mn-Si alloys. *Journal of Materials Science*, Vol. 8 (1989) pp. 37-40

Dorazil, E., Barta, B., Munsterova, E., Stransky, L. and Huvar, A.: High-strength bainitic ductile cast iron. *International Cast Metals Journal*, Vol. 7 (1982) pp. 52-62

Druker, A., Baruj, A. and Malarría, J.: Effect of rolling conditions on the structure and shape memory properties of Fe-Mn-Si alloys. *Materials Characterization*, Vol. 61 (2010) pp. 603-612

Dunne, D. P. and Wayman, C. M.: The crystallography of ferrous martensites, M*etallurgical transactions*, Vol. 2 (1971) pp. 2327-2341

Dunne, D. P. and Li, H.: The mechanism of therrmomechanical training of a newly developed Fe-Mn-Si-Cr-Cu shape memory alloy. *Journal de Physique Colloque*, Vol. 5 (1995) C8 pp. 415-420

Dyson, D. J. and Holmes, B.: Effect of alloying additions on the lattice parameter of austenite, *Journal of the Iron and Steel Institute*, 208 (1970) pp. 469-474

Embury, D. and Bouazia, O.: Steel-based composites: driving force and classifications. *Annual Reviews in Materials Science*, Vol. 40 (2010) pp. 213-421

Eskil, M. and Kanca, E.: A new formulation for martensite start temperature of Fe-Mn-Si shape memory alloys using genetic programming. *Computational Materials Science*, Vol. 43 (2008) pp. 774-784

Fisher, J. C., Hollomon J. H. and Turnbull, D.: Kinetics of the austenite-martensite transformation. *Journal of Metals Transactions*, Vol. 185 (1949) pp. 691-700

Frommeyer, G., Brüx, U. and Neumann, P.: Supra-ductile and high-strength manganese-TRIP/TWIP steels for high energy absorption purpose. *ISIJ International*, Vol. 43 (2003) pp. 438-446

Fujita, M. and Uchiyama, I.: Formation of ε phase in Fe-Mn alloys under high pressure and its stability under tensile stress. *Tetsu-to-Hagané*, Vol. 60 (1974) pp. 525-539

Garboczi, E. J., Snyder, K. A., Douglas, J. F. and Thorpe, M. F.: Geometrical percolation threshold of overlapping ellipsoids. *Physical Review E*, Vol. 52 (1995) pp. 819-828

García-Junceda, A., Capdevila, C., Caballero, F. G. and García de Andrés, C.: Dependence of martensite start temperature on fine austenite grain size. *Scripta Materialia*, Vol. 58 (2008) pp. 134-137

Garcia-Mateo, C., Caballero, F. G. and Bhadeshia, H. K. D. H.: Low temperature bainite. *Journal de physique*, Vol. 112 (2003a) pp. 285-288

Garcia-Mateo, C., Caballero, F. G. and Bhadeshia, H. K. D. H.: Hard bainite. *ISIJ International*, Vol. 43 (2003b) pp. 1238-1243

Garcia-Mateo, C., Caballero, F. G. and Bhadeshia, H. K. D. H.: Development of hard bainite. *ISIJ International*, Vol. 43 (2003c) pp. 1238-1243

Garcia-Mateo, C., Caballero, F. G. and Bhadeshia, H. K. D. H.: Acceleration of low-temperature bainite. *ISIJ International*, Vol. 43 (2003d) pp. 1821-1825

Garcia-Mateo, C. Peet, M., Caballero, F. G. and Bhadeshia, H. K. D. H.: Tempering of hard mixture of bainitic ferrite and austenite. *Materials Science and Technology*, Vol. 20 (2004) pp. 814-818

Garcia-Mateo, C. and Caballero, F. G.: Role of retained austenite on tensile properties of steels with bainitic microstructures. *Materials Transactions*, Vol. 46 (2005) pp. 1839-1846

Gavriljuk, V. G., Bliznuk, V. V., Shanina, B. D. and Kolesnik, S. P.: Effect of silicon on atomic distribution and shape memory in Fe-Mn base alloys. *Materials Science and Engineering A*, Vol. 406 (2005) pp. 1-10

Georgiyeva, I. Ya., Sorokina, N. A. and Gal'tsova, V. I.: Investigation of phase transformations in Fe-Cr-Mn steels. *Physics of Metals and Metallography*, Vol. 49 (1981) pp. 178-181

Ghosh, G. and Olson, G. B.: Kinetics of f.c.c.→b.c.c. teterogeneous martensitic nucleation-I. The Critical driving force for athermal nucleation, *Acta Metallurgica et Materialia*. Vol. 42 (1994) pp. 3361-3370

Ghosh, G. and Olson, G. B.: Computational thermodynamics and kinetics of martensitic transformation. *Journal of Phase Equilibria*, Vol. 22 (2001) pp. 199-207

Ghosh, G. and Olson, G. B.: The isotropic shear modulus of multicomponent Fe-base solid solutions. *Acta Materialia*, Vol. 50 (2002) pp. 2655-2675

Grange, R. A. and Stewrt, H. M.: The temperature range of martensite formation. T*ransactions of AIME*, Vol. 167 (1945) pp. 467-494

Girault, E.: Bainite transformation in TRIP-assisted steels and its influence on mechanical properties, PhD theis, Katholieke Uniersiteit (1999)

Grässel, O., Kruger, L., Frommeyer,G. and Meyer, L. W.: High strength Fe-Mn-(Al-Si) TRIP/TWIP steels development-properties-application. *International Journal of Plasticity*, Vol. 16 (2000) pp. 13911409

Greninger, A. B. and Troiano, A. R.: The mechanism of martensite formation. *Transactions of AIME*, Vol. 1 (1949) pp. 590-598

Guimarães, J. R. C. and Gomes, J. C.: A metallographic study of the influence of the austenite grain size on martensite kinetics in Fe-31.9Ni-0.02C. *Acta Metallurgica*, Vol. 26 (1978) pp. 1591-1596

Gulyaev, A. P., Volynova, T. F. and Georgiyeva, I. Ya.: Phase transformations in high-purity Fe-Mn alloys. *Metals Science and Heat Treatment*, Vol. 20 (1978) pp. 179-182

Hamers, A. A. H. and Wayman, C. M.: Shape memory behavior in Fe-Mn-Co alloys. *Scripta Metallurgica and Materials*, Vol. 25 (1991) pp. 2723-2728

Hannink, R. H. J., Kelly, P. M. and Muddle, B. C.: Transformation toughening in zirconia-containing ceramics. *Journal of the American Ceramic Society*, Vol. 83 (2000) pp. 61-487

Hillert, M.: Paradigm shift for bainite. *Scripta Materialia*, Vol. 47 (2002) pp. 175-180

Hillert, M., Höglund, L. and Ågren, J.: Role of carbon and alloying elements in the formation of bainitic ferrite. *Metallurgical and Materials Transactions A*, Vol. 35A (2004) pp.3693-3700

Hsu, T. Y.: An approximate approach for the calculation of M_S in iron-base alloys. *Journal of Materials Science,* Vol. 20 (1985) pp. 23-31

Huang, J. and Xu, Z.: Effect of dynamically recrystallized austenite on the martensite start temperature of martensitic transformation. *Materials Science and Engineering A*, Vol. 438-440 (2006) pp. 254-257

Ishida, K. and Nishizawa, T.: Effect of alloying elements on stability of epsilon iron. *Transactions of the Japan Institute of Metals*, Vol. 15 (1974) pp. 225-231

Jacques, P. J.: Transformation-induced plasticity for high strength formable steels. *Current Opinion in Solid State and Materials Science*, Vol. 8 (2004) pp. 259-265

Jee, K. K., Jang, W. Y., Baik, S. H., Shin, M. C. and Choi, C. S.: Transformation behavior and its effect on damping capacity in Fe-Mn based alloys. *Journal de Physique Colloque*, Vol. 5 (1995) C8 pp. 385-390

Jiang, B. H., Qi, X., Zhou, W. and Hsu, T. Y.: Comment on "Influence of austenite grain size on $\gamma \rightarrow \varepsilon$ martensitic transformation temperature in Fe-Mn-Si-Cr alloys". *Scripta Materialia*, Vol. 34 (1996) pp. 771-773

Jun, J. H. and Choi, C. S.: Variation of stacking fault energy with austenite grain size and its effect on the M_S temperature of $\gamma \rightarrow \varepsilon$ martensitic transformation in Fe-Mn alloy. *Materials Science Engineering A*, Vol. 257 (1998a) pp. 535-556

Jun, J. H. and Choi, C. S.: Strain amplitude dependence of the damping capacity in Fe-17%Mn alloy. *Scripta Materialia*, Vol. 38 (1998b) pp. 543-549

Jun, J. H. and Choi, C. S.: The influence of Mn content on microstructure and damping capacity in Fe-(17~23)%Mn alloys. *Materials Science and Engineering A*, Vol. 252 (1998c) pp. 133-138

Jun, J. H., Kong, D. K. and Choi, C. S.: The influence of Co on damping capacity of Fe-Mn-Co alloys. *Materials Research Bulletin,* Vol. 33 (1998) pp. 1419-1425

Kaufman, L., Colugherty, E. V. and Weiss, R. J.: The lattice stability of metals – iii iron. *Acta Metallurgica*, Vol. 11 (1963) pp. 323-335

Kelly, P. M. and Nutting J.: The martensite transformation in carbon steels. *Proceedings of the Royal Society A*. Vol. 259 (1960) pp. 45-58

Koistinen, D. P. and Marburger, R. E.: A general equation prescribing the extent of the austenite-martensite transformation in pure iron-carbon alloys and plain carbon steels, *Acta Metallurgica*, Vol. 7 (1959) pp. 59-60

Kozeschnik, E. and Bhadeshia, H. K. D. H.: Influence of silicon on cementite precipitation in steels, *Materials Science and Technology*, Vol. 24 (2008), pp.343-347

Kurdjumov, G. and Sachs, G.: Über den mechanismus der stahlhärung. *Zeitschrift fűr Physik*, Vol. 64 (1930) pp. 325-343

Langford, G. and Cohen, M.: Calculation of cell-size strengthening of wire-drawn iron, *M Met. Trans.* Vol. 1 (1970) no. 5 pp. 1478-1480.

Lee, Y. K., Jun, J. H. and Choi, C. S.: Effect of ε martensite content on the damping capacity of Fe-17% Mn alloy. *Scripta Materialia*, Vol. 35 (1996) pp. 825-830

Lee, Y. K., Jun, J. H. and Choi, C. S.: Damping capacity in Fe-Mn binary alloys. *ISIJ International*, Vol. 37 (1997) pp. 1023-1030

Lee, Y. K. and Choi, C. S.: Driving force for $\gamma \rightarrow \varepsilon$ martensitic transformation and stacking fault energy of γ in Fe-Mn binary system. *Metallurgical Materials Transactions A*. Vol. 31 (2000) pp. 355-360

Lee, S. J. and Lee, Y. K.: Effect of austenite grain size on martensitic transformation of a low alloy steel. *Materials Science forum*, Vol. 475 (2005) pp. 3169-3172

Lenkkeri, J. T. and Levoska, J.: Effects of magnetic and structural changes on elastic moduli of iron-manganese alloys. *Philosophical Magazine. A*, Vol. 48 (1983) pp. 749-758

LePera, F. S.: Improved etching technique for the determination of percent martensite in high-strength dual-phase steels. *Metallography*, Vol. 12 (1979) pp. 263-268

Leslie, W. C. and Miller, R. L.: The stabilization of austenite by closely spaced boundaries. *ASM Transactions Quarterly*, Vol. 57 (1964) pp. 972-979

Li, J. and Wayman, C. M.: Shape memory effect and related phenomena in a microalloyed Fe-Mn-Si alloy. *Materials Characterization*, Vol. 32 (1994) pp. 215-227

Li, H., Dunne, D. and Kennon, N.: Factors influencing shape memory effect and phase transformation behavior of Fe-Mn-Si based shape memory alloys. *Materials Science and Engineering A*, Vol. 273-275 (1999) pp. 517-523

Li, C. L., Cheng, D. J. and Jin, J. H.: Influence of deformation temperature on shape memory effect Fe-Mn-Si-Ni-Cr alloy. *Materials Science and Engineering A*, Vol. 325 (2002) pp. 375-379

Liu, T., Zhao, Z. T. and Ma, R. Z.: On the $\gamma \rightarrow \varepsilon$ transformation below the Néel temperature in Fe-Mn-Si alloys. *Phase Transitions*. Vol. 69 (1999) pp. 425-428

Mackenzie, J. K and Bowles, J. S.: The crystallography of martensite transformations II. *Acta Metallurgica*, Vol. 2 (1954) pp. 138-147

Magee, C. L.: The nucleation of martensite, in 'Phase transformations', (1970) pp. 115-156

Maji, B. C. and Krishnan, M.: The effect of microstructure on the shape recovery of a Fe-Mn-Si-Cr-Ni stainless steel shape memory alloy. *Scripta Materialia*, Vol. 48 (2003) pp. 71-77

Maki, T., Shimooka, S. and Tamura, I.: The MS temperature and morphology of martensite in Fe-31% Ni-0.23% C alloy. *Metallurgical Transactions*, Vol. 2 (1971) pp. 2944-2945

Matsuzaki, A. and Bhadeshia, H. K. D. H.: Effect of austenite grain size and bainite morphology on the overall transformation kinetics of the bainite reaction in steels. *Materials Science and Technology*, Vol. 15 (1995) pp. 518-521

McMurtie, D. G. and Magee, C. L.: The average volume of martensite plates during transformation. *Metallurgical Transactions*, Vol. 1 (1970) pp. 3185-3191

Moore, D. J., Rouns, T. N. and Rundman, K. B.: Structure and mechanical properties of austempered ductile irons. *AFS Transactions*, Vol. 93 (1985) 705-718

Mujahid, S. and Bhadeshia, H. K. D. H.: The partitioning of carbon from supersaturated ferrite plates. *Acta Metallurgica et Materialia*, Vol. 40 (1992) pp. 389-396

Mujahid, S. A. and Bhadeshia H. K. D. H.: Coupled diffusional/displacive transformations: addition of substitutional alloying elements. *Journal of Physics D: Applied Physics*, Vol. 34 (2001) pp. 2573-2580

Nehrenberg, A. E., *Transactions of AIME*, Vol. 167 (1945) pp. 494-501

Nishiyama, Z.: X-ray investigation of the mechanism of the transformation from face centered cubic lattice to body centered cubic. Science Reports of the Research Institutes Tohoku University Series A-Physics Chemistry and Metallurgy. Vol. 23 (1934) pp. 637-664

Nishiyama, Z.: Martensitic Transformation. Academic Press, New York (1978) pp. 115-123

Okumura, T. and Sourmail, T.: MAP_STEEL_MTTTDATA, http://www.msm.cam.ac.uk/map/steel/programs/mtttdata.html

Olson, G. B. and Cohen, M.: A general mechanism of martensitic nucleation, part I-III. *Metallurgical Transactions A*, Vol. 7 (1976) pp. 1897-1923

Olson, G. B., Tsuzaki, K. and Cohen, M.: Statistical aspects of martensitic nucleation. *Materials Research Society Symposia Proceedings*, Vol. 57 (1987) pp. 129-148

Olson, G. B., Bhadeshia, H. K. D. H. and Cohen, M.: Coupled diffusion/displacive transformations. *Acta Metallurgica*, Vol. 37 (1989) pp. 381-390

Olson, G. B., Bhadeshia, H. K. D. H. and Cohen, M.: Coupled diffusion/displacive transformations. Part II. Solute trapping. *Metallurgical Transactions A*, Vol. 21A (1990) pp. 805-509

Olson, G. B.: New directions in martensite theory. *Materials Science and Engineering A*, 273-275 (1999) pp. 11-20

Otsuka, H., Yamada, H., Maruyma, T., Tanahashi, H., Matsuda, S. and Murakami, M.: Effects of alloying additions on Fe-Mn-Si shape memory alloys. *ISIJ International*, Vol. 30 (1990) pp. 674-679

Palumbo: Thermodynamics of martensitic transformation in the framework of the CALPHAD approach. *CALPHAD*, Vol. 32 (2008) 693-708

Payson, P. and Savage, C. H.: Martensite reactions in alloy steels. *Transactions of ASM*, Vol. 33 (1944) pp. 261-281

Peet, M., Babu, S. S., Miller, M. K. and Bhadeshia, H. K. D. H.: Three-dimensional atom probe analysis of carbon distribution in low-temperature bainite, *Scripta Materialia*, Vol. 50 (2004) pp. 1277-1281

Pereloma, E. V., Timokhina, I. B., Miller, M. K. and Hodgson, P. D.: Three-dimensional atom probe analysis of solute distribution in thermomechanically processed TRIP steels, *Acta Materialia*, Vol. 55 (2007) pp. 2587-2598

Porter, D. A., Easterling, K. E. and Sherif, M. Y.: Phase transformations in metals and alloys 3rd edition. (2008) CRC Press

Rao, B. V. N. and Rashid, M. S.: Direct observations of deformation-induced retained austenite transformation in a vanadlum-containing dual-phase steel. *Metallography*, Vol. 16 (1983) pp. 19-37

Rong, L. J., Ping, D. H., Li, Y. Y. and Shi, C. X.: Improvement of shape memory effect in Fe-Mn-Si alloy by Cr and Ni addition. *Scripta Materialia*, Vol. 32 (1995) pp. 1905-1909

Sade, M, Halter K. and Hornbogen, E.: Transformation behavior and one-way shape memory effect in Fe-Mn-Si shape memory alloys. J*ournal of Materials Science Letters* Vol. 9 (1990) pp. 112-115

Sandvik, B. J. P.: The bainite reaction in Fe-Si-C alloys, the primary stage, *Metallurgical Transactions* 13A (1982) pp. 777-787

Sato, A., Shishiman, E. , Yamaji, Y. and Mori, T.: Orientation and composition dependencies of shape memory effect in Fe-Mn-Si alloys. *Acta Metallurgica*, Vol. 32 (1984) pp. 539-547

Sherif, M. Y.: Characterisation and development of nanostructured, ultrahigh strength, and ductile bainitic steels, Ph. D. thesis, Cambridge University (2006)

Shimizu, K. and Nishiyama, Z.: Electron microscopic studies of martensitic transformations in iron alloys and steels. *Metallurgical Transactions*, Vol. 3 (1972) pp. 1055-1068

Singh, S. B. and Bhadeshia, H.K.D.H.: Estimation of bainite plate-thickness in low-alloy steels, *Materials Science and Engineering A,* Vol. 245 (1998) pp. 72–79

Sourmail, T. and Garcia-Mateo, C.: A model for predicting the M_S temperatures of steels. *Computational Materials Science*, Vol. 34 (2005a) pp. 213-218

Sourmail, T. and Garcia-Mateo, C.: Critical assessment of models for predicting the M_S temperature of steels. *Computational Materials Science*, Vol. 34 (2005b) pp. 323-334

Speer, J., Matlock D. K., De Cooman, B. C. and Schroth, J. G.: Carbon partitioning into austenite after martensite transformation. *Acta Materialia*, Vol. 51 (2003) pp. 2611-2622

Steven, W. and Haynes, A. G.: The temperature of formation of martensite and bainite in low-alloy steel. *Journal of Iron and Steel Research International*, Vol. 183 (1956) pp.349-359

Swallow, E. And Bhadeshia, H. K. D. H.: High resolution observations of displacements caused by bainitic transformation. *Materials Science and Technology*, Vol. 12 (1996) pp.121-125

Takahashi, M. and Bhadeshia, H. K. D. H.: A model for the transition from upper to lower bainite*, Materials Science and Technology*, Vol. 6 (1990) pp.592-603.

Takaki, S., Furuya, T. and Tokunaga, Y.: Effect of Si and Al additions on the low temperature toughness and fracture mode of Fe-27Mn alloys. *ISIJ International,* Vol. 30 (1990) pp. 632-638

Takaki, S., Nakatsu, H. and Tokunaga, T.: Effect of austenite grain size on martensitic transformation in Fe-15mass%Mn alloy. *Materials Transactions JIM*, Vol. 34 (1993) pp. 489-495

Tomita, Y.: Effect of microstructure on plane-strain fracture toughness of AISI 4340 steel. *Metallurgical Transactions A*, Vol. 19A (1988) pp. 2513-2521

Tomota, Y., Strum, M. and Morris, J. W. Jr.: Microstructural dependence of Fe-high Mn tensile behavior. *Metallurgical Transactions A,* Vol. 17 (1986) pp. 537-547

Tomota, Y., Nakagawara, W., Tsuzaki, K. and Maki, T.: Reversion of stress-induced ε martensite and two-way shape memory in Fe-24Mn and Fe-24Mn-6Si alloys. *Scripta Materialia*, Vol. 26 (1992) pp. 1571-1574

Tomota, Y. and Yamaguchi, K.: Influence of Alfa martensite on shape memory in Fe-Mn-based alloys. *Journal de Physique Colloque*, Vol. 5 (1995) C8 pp. 421-426

Tomota, Y., Morioka, Y. and Nakagawara, W.: Epsilon martensite to austenite reversion and related phenomena in Fe-24Mn and Fe-24Mn-6Si alloys. *Acta Materialia* Vol. 46 (1998) pp. 1419-1426

Tomota, Y. and Maki, T.: Reversibility in martensitic transformation and shape memory in high Mn ferrous alloys. *Materilas Science Forum*, Vol. 327-328 (2000) pp. 191-198

Troiano, A. R. and McGuire, F. T.: A study of the iron-rich iron-manganese alloys. *Transactions of the ASM*, Vol. 31 (1943) pp. 340-364

Tsuzaki, K., Fukasaku, S., Tomota, Y. and Maki, T.: Effect of prior deformation of austenite on the $\gamma \rightarrow \varepsilon$ martensitic transformation in Fe-Mn alloys. *Materials Transactions JIM*, Vol. 32 (1991) pp. 222-228

Umebayashi, H. and Ishikawa, Y.: Antiferromagnetism of γ Fe-Mn alloys. *Journal of the Physical Society of Japan*, Vol. 21 (1966) pp. 1281-1294

Umemoto, M. and Owen, W. S.: Effects of austenitizing temperature and austenite grain size on the formation of athermal martensite in an iron-nickel and an iron-nickel-carbon alloy. *Metallurgical and Materials Transactions B*, Vol. 5 (1975) pp. 2041-2046

Wang, J., van der Wolk, P. J. And van der Zwaag, S.: Determination of martensite start temperature in engineering steels part I. Empirical relations describing the effect of steel chemistry. *Materials Transactions JIM*, Vol. 41 (2000) pp. 761-768

Wang, Z. and Zhu, J.: Cavitation erosion of Fe-Mn-Si-Cr shape memory alloys. *Wear*, Vol. 256 (2004) pp. 66-72

Wassermann, G.: Einfluβ der α-γ-umwandlung eines irreversiblen Nickelstahls auf krystallorierung und zugfestigkeit. *Archiv für das Eisenhűttenwesen*, Vol. 6 (1933) pp. 347-351

Wechsler, M. S., Lieberman, D. S. and Read, T. A.: On the theory of the formation of martensite. *Transactions AIME* (1953) pp. 1503-1515

Wen, Y., Li, N. and Tu, M.: Effect of quenching temperature on recovery stress of Fe-18Mn-5Si-8Cr-4Ni alloy. *Scripta Materialia*, Vol. 44 (2001) pp. 1113-1116

Wen, Y. H., Yan, M. and Li, N.: Effects of carbon addition and aging on the shape memory effect of Fe-Mn-Si-Cr-Ni alloys. *Scripta Materialia*, Vol. 50 (2004) pp. 441-444

Wen, Y. H., Xie, W. L., Li, N. and Li, D.: Remarkable difference between effects of carbon contents on recovery strain and recovery stress. *Materials Science and Engineering A*, Vol. 457 (2007) pp. 334-337

Wu, X., Hsu, T. Y.: Effect of the Neel temperature, T_N, on martensitic transformation in Fe-Mn-Si-based memory alloys. *Materials Characterization*, Vol. 45 (2000) pp. 137-142

Yamaguchi, K., Morioka, Y. and Tomota, Y.: Anisotropy in the shape memory effect in thermomechanically treated Fe-Mn-Si alloys. *Scripta Materialia*, Vol. 35 (1996) pp. 1147-1152

Yang, J. H., Chen, H. and Wayman, C. M.: Development of Fe-Based Shape Memory alloys associated with face-centered cubic-Hexagonal close-packed martensitic transformations: Part I. Shape memory behavior. *Metallurgical Transactions A*, Vol. 23 (1992) pp. 1431-1437

Yang, H.-S. and Bhadeshia, H. K. D. H.: Uncertainties in dilatometric determination of martensite start temperature. *Materials Science and Technology*, Vol. 23 (2007) pp. 556-560

Yang, H.-S.: Low-carbon, low-temperature bainite. Master thesis, Pohang University of Science and Technology, South Korea (2008)

Yang, H.-S. and Bhadeshia, H. K. D. H.: Designing low carbon, low temperature bainite. *Materials Science and Technology*, Vol. 24 (2008) pp. 335-342

Yang, H.-S. and Bhadeshia, H. D. D. H.: Austenite grain size and the martensite-start temperature. *Scripta Materialia*, Vol. 60 (2009) pp. 493-495

Yang, H.-S., Jang, J. H., Bhadeshia, H. K. D. H. and Suh, D. W.: Critical assessment: martensite-start temperature for the $\gamma \rightarrow \epsilon$ transformation, submitted (2011)

Yang, C. H., Lin, H. C. and Lin, K. M.: Improvement of shape memory effect in Fe-Mn-Si alloy by slight tantalum addition. *Materials Science and Engineering A*, Vol. 518 (2009) pp. 193-143

Zhang, Y. S., Lu, X., Tian, X. and Qin, Z.: Compositional dependence of the Néel transition, structural stability, magnetic properties and electrical resistivity in Fe-Mn-Al-Cr-Si alloys. *Materials Science and Engineering A*, Vol. 334 (2002) pp. 19-27

Zhang, M. R. and Gu, H. C.: Microstructure and properties of carbide free bainite railway wheels produced by programmed quenching. *Materials Science and Technology*, Vol. 23 (2007) pp. 970-974

Zhou, W., Jiang, B., Qi, X. and Hsu, T. Y.: The influence of rare earth element on shape memory effect in Fe-Mn-Si alloys. *Scripta Materialia*, Vol. 39 (1998) pp. 1483-1487

Acknowledgements

I am extremely grateful to my supervisor, Professor H. K. D. H. Bhadeshia, for his constant guidance, support, great friendship and for his unique and charming way of teaching the simplicity and beauty of science. I am also thankful to Professor Dong-Woo Suh, my co-advisor, for advise, guidance and support. And thanks to Professor In Gee Kim and Professor Rongshan Qin for their advise and friendship.

I acknowledge POSCO for their strong financial support to me and establishment of GIFT. I am also thankful to Dr Kyoo-Young Lee for the preparing test alloys. I thank members in Sheet Products and Process Research Group for discussions.

I also would like to thank Professor Hae-Geon Lee for introducing GIFT and kind encouragement when I joined GIFT. I would like to express my sincere thanks to all the people in the GIFT, especially those members in Computational Metallurgy Laboratory (CML), for all their help and for all the happiness we shared. The life with CML members was quite pleasant and enjoyable.

I thank all my friends for their encouragement and friendship. Every GIFT friend, class mate during undergraduate course and other every friend is precious for me.

Finally, I would like to take this opportunity to express my gratitude to my family members for their love, unfailing encouragement and support.

CURRICULUM VITAE

Name: Yang, Hong-Seok (양 홍 석)
E-mail: puremind@potsech.ac.kr; puremind@posco.co.kr
Date of birth: 11th August, 1980
Place of birth: Jeju, South Korea

Education

Ph. D. 2011, POSTECH (Pohang, Korea), Graduate Institute of Ferrous Technology, Computational Metallurgy Group.

M. S. 2008, POSTECH (Pohang, Korea), Graduate Institute of Ferrous Technology, Computational Metallurgy Group.

B. S. 2006 POSTECH (Pohang, Korea), Department of Chemical Engineering.

Publications

Hong-Seok Yang and H. K. D. H. Bhadeshia: Uncertainties in dilatometric determination of martensite start temperature. *Materials Science and Technology,* Vol.23 (2007) pp. 556-560

Hong-Seok Yang and H. K. D. H. Bhadeshia: Designing of low-carbon, low-temperature bainite. *Materials Science and Technology,* Vol. 24 (2008) pp. 335-342

Yang, H.-S., Park, J. H. and Bhadeshia, H. K. D. H.: Possibility of low-carbon, low-temperature bainite. Proceedings of the International Conference on Martensitic Transformations, ICOMAT-08 (2008) pp. 695-702

Hong-Seok Yang and H. D. D. H. Bhadeshia: Austenite grain size and the martensite-start temperature. *Scripta Materialia*, Vol. 60 (2009) pp. 493-495

Hong-Seok Yang, Jae-Hoon Jang, H. K. D. H. Bhadeshia and Dong-Woo Suh: Critical assessment: martensite-start temperature for the $\gamma \rightarrow \epsilon$ transformation, will be published (2011)